

1

²A SEARCH FOR LONG-LIVED, CHARGED, SUPERSYMMETRIC PARTICLES
³USING IONIZATION WITH THE ATLAS DETECTOR

4

BRADLEY AXEN

5

September 2016 – Version 0.41

6



⁸ Bradley Axen: *A Search for Long-Lived, Charged, Supersymmetric Particles using*
⁹ *Ionization with the ATLAS Detector*, Subtitle, © September 2016

10

Usually a quotation.

11

Dedicated to.

₁₂ ABSTRACT

₁₃ How to write a good abstract:

₁₄ <https://plg.uwaterloo.ca/~migod/research/beck00PSLA.html>

₁₅ PUBLICATIONS

₁₆ Some ideas and figures have appeared previously in the following publications:

₁₇

₁₈ Put your publications from the thesis here. The packages `multibib` or `bibtopic`
₁₉ etc. can be used to handle multiple different bibliographies in your document.

²¹ ACKNOWLEDGEMENTS

²² Put your acknowledgements here.

²³

²⁴ And potentially a second round.

²⁵

26 CONTENTS

27	I	INTRODUCTION	1
28	1	INTRODUCTION	3
29	II	THEORETICAL CONTEXT	5
30	2	STANDARD MODEL	7
31	2.1	Particles	7
32	2.2	Interactions	8
33	2.3	Limitations	8
34	3	SUPERSYMMETRY	9
35	3.1	Motivation	9
36	3.2	Structure	9
37	3.3	Phenomenology	9
38	4	LONG-LIVED PARTICLES	11
39	4.1	Mechanisms	11
40	4.1.1	Examples in Supersymmetry	11
41	4.2	Phenomenology	11
42	4.2.1	Disimilarities to Prompt Decays	11
43	4.2.2	Characteristic Signatures	11
44	III	EXPERIMENTAL STRUCTURE AND RECONSTRUCTION	13
45	5	THE LARGE HADRON COLLIDER	15
46	5.1	Injection Chain	16
47	5.2	Design	17
48	5.2.1	Layout	17
49	5.2.2	Magnets	18
50	5.2.3	RF Cavities	19
51	5.2.4	Beam	21
52	5.3	Luminosity Parameters	21
53	5.4	Delivered Luminosity	23
54	6	THE ATLAS DETECTOR	25
55	6.1	Coordinate System	25
56	6.2	Magnetic Field	25
57	6.3	Inner Detector	26
58	6.3.1	Pixel Detector	30
59	6.3.2	Semiconductor Tracker	30
60	6.3.3	Transition Radiation Tracker	30
61	6.4	Calorimetry	30
62	6.4.1	Electromagnetic Calorimeters	30
63	6.4.2	Hadronic Calorimeters	30
64	6.4.3	Forward Calorimeters	30
65	6.5	Muon Spectrometer	30

66	6.6	Trigger	32
67	6.6.1	Trigger Scheme	32
68	6.6.2	Missing Transverse Energy Triggers	32
69	7	EVENT RECONSTRUCTION	33
70	7.1	Tracks and Vertices	33
71	7.1.1	Track Reconstruction	33
72	7.1.2	Vertex Reconstruction	33
73	7.2	Jets	33
74	7.2.1	Topological Clustering	33
75	7.2.2	Jet Energy Scale	33
76	7.2.3	Jet Energy Scale Uncertainties	33
77	7.2.4	Jet Energy Resolution	33
78	7.3	Electrons	33
79	7.3.1	Electron Identification	33
80	7.4	Muons	33
81	7.4.1	Muon Identification	33
82	7.5	Missing Transverse Energy	33
83	IV	CALORIMETER RESPONSE	35
84	8	RESPONSE MEASUREMENT WITH SINGLE HADRONS	37
85	8.1	Dataset and Simulation	38
86	8.1.1	Data Samples	38
87	8.1.2	Simulated Samples	38
88	8.1.3	Event Selection	38
89	8.2	Inclusive Hadron Response	39
90	8.2.1	E/p Distribution	39
91	8.2.2	Zero Fraction	40
92	8.2.3	Neutral Background Subtraction	41
93	8.2.4	Corrected Response	43
94	8.2.5	Additional Studies	45
95	8.3	Identified Particle Response	48
96	8.3.1	Decay Reconstruction	48
97	8.3.2	Identified Response	49
98	8.3.3	Additional Species in Simulation	51
99	8.4	Summary	52
100	9	JET ENERGY RESPONSE AND UNCERTAINTY	55
101	9.1	Motivation	55
102	9.2	Uncertainty Estimate	55
103	9.3	Summary	58
104	V	SEARCH FOR LONG-LIVED PARTICLES	61
105	10	LONG-LIVED PARTICLES IN ATLAS	63
106	10.1	Event Topology	63
107	10.1.1	Detector Interactions	64
108	10.1.2	Lifetime Dependence	65
109	10.2	Simulation	68

110	11	EVENT SELECTION	71
111	11.1	Trigger	72
112	11.2	Kinematics and Isolation	73
113	11.3	Particle Species Rejection	77
114	11.4	Ionization	80
115	11.4.1	Mass Estimation	81
116	11.5	Efficiency	82
117	12	BACKGROUND ESTIMATION	85
118	12.1	Background Sources	85
119	12.2	Prediction Method	86
120	12.3	Validation	87
121	12.3.1	Closure in Simulation	87
122	12.3.2	Validation Region in Data	88
123	13	SYSTEMATIC UNCERTAINTIES AND RESULTS	91
124	13.1	Systematic Uncertainties	91
125	13.1.1	Background Estimate	91
126	13.1.2	Signal Yield	92
127	13.2	Final Yields	98
128	13.3	Cross Sectional Limits	99
129	13.4	Mass Limits	101
130	13.5	Context for Long-Lived Searches	103
131	VI	CONCLUSIONS	107
132	14	SUMMARY AND OUTLOOK	109
133	14.1	Summary	109
134	14.2	Outlook	109
135	VII	APPENDIX	111
136	A	INELASTIC CROSS SECTION	113
137	B	EXPANDED R-HADRON YIELDS AND LIMITS	115
138	BIBLIOGRAPHY		121

¹³⁹ LIST OF FIGURES

¹⁴⁰ Figure 1	The particle content of the Standard Model (SM).	8
¹⁴¹ Figure 2	The four collision points and corresponding experiments of the Large Hadron Collider (LHC). The image includes the location of the nearby city of Geneva as well as the border of France and Switzerland.	16
¹⁴²		
¹⁴³		
¹⁴⁴		
¹⁴⁵ Figure 3	The cumulative luminosity over time delivered to the A Toroidal LHC ApparatuS (ATLAS) experiment from high energy proton-proton collisions since 2011. The energies of the collisions are listed for each of the data-taking periods.	17
¹⁴⁶		
¹⁴⁷		
¹⁴⁸		
¹⁴⁹		
¹⁵⁰ Figure 4	The accelerator complex that builds up to the full design energies at the LHC . The protons are passed in order to Linac 2, the PSB , the PS , the SPS and then the LHC	18
¹⁵¹		
¹⁵²		
¹⁵³		
¹⁵⁴ Figure 5	A schematic of the layout of the LHC , not to scale. The arched and straight sections are illustrated at the bottom of the schematic, and all four crossing sites are indicated with their respective experiments.	19
¹⁵⁵		
¹⁵⁶		
¹⁵⁷		
¹⁵⁸ Figure 6	A cross section of the the cryodipole magnets which bend the flight path of protons around the circumference of the LHC . The diagram includes both the superconducting coils which produce the magnetic field and the structural elements which keep the magnets precisely aligned.	20
¹⁵⁹		
¹⁶⁰		
¹⁶¹		
¹⁶²		
¹⁶³		
¹⁶⁴ Figure 7	The arrangement of four radiofrequency (RF) cavities within a cryomodule.	20
¹⁶⁵		
¹⁶⁶ Figure 8	The cumulative luminosity versus time delivered to ATLAS (green), recorded by ATLAS (yellow), and certified to be good quality data (blue) during stable beams for pp collisions at 13 TeV in 2015.	23
¹⁶⁷		
¹⁶⁸		
¹⁶⁹		
¹⁷⁰ Figure 9	The luminosity-weighted distribution of the mean number of interactions per crossing for the 2015 pp collision data at 13 TeV.	24
¹⁷¹		
¹⁷²		
¹⁷³ Figure 10	· · · · ·	25
¹⁷⁴ Figure 11	· · · · ·	25
¹⁷⁵ Figure 12	· · · · ·	26
¹⁷⁶ Figure 13	· · · · ·	26
¹⁷⁷ Figure 14	· · · · ·	27
¹⁷⁸ Figure 15	· · · · ·	27
¹⁷⁹ Figure 16	· · · · ·	27
¹⁸⁰ Figure 17	· · · · ·	28

181	Figure 18	28
182	Figure 19	28
183	Figure 20	29
184	Figure 21	29
185	Figure 22	30
186	Figure 23	30
187	Figure 24	31
188	Figure 25	31
189	Figure 26	32
190	Figure 27	
191		An illustration (a) of the E/p variable used throughout this paper. The red energy deposits come from the charged particle targeted for measurement, while the blue energy deposits are from nearby neutral particles and must be subtracted. The same diagram (b) for the neutral-background selection, described in Section 8.2.3.
192		40
193		
194		
195		
196	Figure 28	40
197		The E/p distribution and ratio of simulation to data for isolated tracks with (a) $ \eta < 0.6$ and $1.2 < p/\text{GeV} < 1.8$ and (b) $ \eta < 0.6$ and $2.2 < p/\text{GeV} < 2.8$.
198		40
199	Figure 29	
200		
201		
202		
203	Figure 30	42
204		$\langle E/p \rangle_{\text{BG}}$ as a function of the track momentum for tracks with (a) $ \eta < 0.6$, (b) $0.6 < \eta < 1.1$, and as a function of the track pseudorapidity for tracks with (c) $1.2 < p/\text{GeV} < 1.8$, (d) $1.8 < p/\text{GeV} < 2.2$.
205		43
206		
207	Figure 31	44
208		$\langle E/p \rangle_{\text{COR}}$ as a function of track momentum, for tracks with (a) $ \eta < 0.6$, (b) $0.6 < \eta < 1.1$, (c) $1.8 < \eta < 1.9$, and (d) $1.9 < \eta < 2.3$.
209		
210	Figure 32	45
211		$\langle E/p \rangle_{\text{COR}}$ calculated using LCW-calibrated topological clusters as a function of track momentum for tracks with (a) zero or more associated topological clusters or (b) one or more associated topological clusters.
212		45
213		
214	Figure 33	46
215		Comparison of the $\langle E/p \rangle_{\text{COR}}$ for tracks with (a) less than and (b) greater than 20 hits in the TRT.
216	Figure 34	46
217		Comparison of the $\langle E/p \rangle_{\text{COR}}$ for (a) positive and (b) negative tracks as a function of track momentum for tracks with $ \eta < 0.6$.
218		46
219	Figure 35	47
220		Comparison of the E/p distributions for (a) positive and (b) negative tracks with $0.8 < p/\text{GeV} < 1.2$ and $ \eta < 0.6$, in simulation with the FTFP_BERT and QGSP_BERT physics lists.
221		47
222		
223	Figure 36	
224		Comparison of the response of the hadronic calorimeter as a function of track momentum (a) at the EM-scale and (b) after the LCW calibration.
225		47

226	Figure 37	Comparison of the response of the EM calorimeter as a function of track momentum (a) at the EM-scale and (b) with the LCW calibration.	48
227			
228			
229	Figure 38	The reconstructed mass peaks of (a) K_S^0 , (b) Λ , and (c) $\bar{\Lambda}$ candidates.	49
230			
231	Figure 39	The E/p distribution for isolated (a) π^+ , (b) π^- , (c) proton, and (d) anti-proton tracks.	50
232			
233	Figure 40	The fraction of tracks with $E \leq 0$ for identified (a) π^+ and π^- , and (b) proton and anti-proton tracks	50
234			
235	Figure 41	The difference in $\langle E/p \rangle$ between (a) π^+ and π^- (b) p and π^+ , and (c) \bar{p} and π^-	51
236			
237	Figure 42	$\langle E/p \rangle_{\text{COR}}$ as a function of track momentum for (a) π^+ tracks and (b) π^- tracks.	52
238			
239	Figure 43	The ratio of the calorimeter response to single particles of various species to the calorimeter response to π^+ with the physics list FTFP_BERT.	52
240			
241			
242	Figure 44	The spectra of true particles inside anti- k_t , $R = 0.4$ jets with (a) $90 < p_T/\text{GeV} < 100$, (b) $400 < p_T/\text{GeV} < 500$, and (c) $1800 < p_T/\text{GeV} < 2300$	56
243			
244			
245	Figure 45	The jet energy scale (<a>JES) uncertainty contributions, as well as the total <a>JES uncertainty, as a function of jet p_T for (a) $ \eta < 0.6$ and (b) $0.6 < \eta < 1.1$	58
246			
247			
248	Figure 46	The <a>JES correlations as a function of jet p_T and $ \eta $ for jets in the central region of the detector.	59
249			
250	Figure 47	A schematic diagram of an R-Hadron event with a lifetime around 0.01 ns. The diagram includes one charged R-Hadron (solid blue), one neutral R-Hadron (dashed blue), Lightest Supersymmetric Particles (<a>LSPs) (dashed green) and charged hadrons (solid orange). The pixel detector, calorimeters, and muon system are illustrated but not to scale.	65
251			
252			
253			
254			
255			
256			
257	Figure 48	A schematic diagram of an R-Hadron event with a lifetime around 4 ns. The diagram includes one charged R-Hadron (solid blue), one neutral R-Hadron (dashed blue), <a>LSPs (dashed green) and a charged hadron (solid orange). The pixel detector, calorimeters, and muon system are illustrated but not to scale.	66
258			
259			
260			
261			
262			
263	Figure 49	A schematic diagram of an R-Hadron event with a lifetime around 5 ns. The diagram includes one charged R-Hadron (solid blue), one neutral R-Hadron (dashed blue), <a>LSPs (dashed green) and charged hadrons (solid orange). The pixel detector, calorimeters, and muon system are illustrated but not to scale.	67
264			
265			
266			
267			
268			

269	Figure 50	A schematic diagram of an R-Hadron event with a life-time around 20 ns. The diagram includes one charged R-Hadron (solid blue), one neutral R-Hadron (dashed blue), LSPs (dashed green) and charged hadrons (solid orange). The pixel detector, calorimeters, and muon system are illustrated but not to scale.	67
270			
271			
272			
273			
274			
275	Figure 51	A schematic diagram of an R-Hadron event with a life-time around 20 ns. The diagram includes one charged R-Hadron (solid blue) and one neutral R-Hadron (dashed blue). The pixel detector, calorimeters, and muon system are illustrated but not to scale.	68
276			
277			
278			
279			
280	Figure 52	The distribution of (a) E_T^{miss} and (b) Calorimeter E_T^{miss} for simulated signal events before the trigger requirement.	72
281			
282			
283	Figure 53	The distribution of E_T^{miss} for data and simulated signal events, after the trigger requirement.	74
284			
285	Figure 54	The trigger efficiency for the HLT_xe70 trigger requirement as a function of (a) E_T^{miss} and (b) Calorimeter E_T^{miss} for simulated signal events.	75
286			
287			
288	Figure 55	The dependence of dE/dx on N_{split} in data after basic track hit requirements have been applied.	76
289			
290	Figure 56	The distribution of dE/dx with various selections applied in data and simulated signal events.	76
291			
292	Figure 57	The distribution of track momentum for data and simulated signal events, after previous selection requirements have been applied.	77
293			
294			
295	Figure 58	The distribution of M_T for data and simulated signal events, after previous selection requirements have been applied.	78
296			
297			
298	Figure 59	The distribution of summed tracked momentum within a cone of $\Delta R < 0.25$ around the candidate track for data and simulated signal events, after previous selection requirements have been applied.	79
299			
300			
301			
302	Figure 60	The normalized, two-dimensional distribution of E/p and f_{EM} for simulated (a) $Z \rightarrow ee$, (b) $Z \rightarrow \tau\tau$, (c) 1200 GeV Stable R-Hadron events, and (d) 1200 GeV, 10 ns R-Hadron events.	80
303			
304			
305			
306	Figure 61	Two-dimensional distribution of dE/dx versus charge signed momentum (qp) for minimum-bias tracks. The fitted distributions of the most probable values for pions, kaons and protons are superimposed.	81
307			
308			
309			
310	Figure 62	The distribution of mass estimated using dE/dx for simulated stable R-Hadrons with masses between 1000 and 1600 GeV.	82
311			
312			

313	Figure 63	The acceptance \times efficiency as a function of R-Hadron (a) mass and (b) lifetime. (a) shows all of the combinations of mass and lifetime considered in this search, and (b) highlights the lifetime dependence for 1000 GeV and 1600 GeV R-Hadrons.	84
314			
315			
316			
317			
318	Figure 64	The distribution of (a) dE/dx and (b) momentum for tracks in data and simulated signal after requiring the event level selection and the track selection on p_T , hits, and N_{split} . Each sub-figure shows the normalized distributions for tracks classified as hadrons, electrons, and muons in data and R-Hadrons in the simulated signal.	86
319			
320			
321			
322			
323			
324			
325	Figure 65	The distribution of $M_{dE/dx}$ (a) before and (b) after the ionization requirement for tracks in simulated W boson decays and for the randomly generated background estimate.	88
326			
327			
328			
329	Figure 66	The distribution of $M_{dE/dx}$ (a) before and (b) after the ionization requirement for tracks in the validation region and for the randomly generated background estimate.	89
330			
331			
332			
333	Figure 67	The trigger efficiency for the HLT_xe70 trigger requirement as a function of Calorimeter E_T^{miss} for simulated data events with a W boson selection. Simulated signal events and simulated W boson events are also included.	94
334			
335			
336			
337			
338	Figure 68	The efficiency of the muon veto for R -hadrons of two different masses, as a function of $\frac{1}{\beta}$ for simulated R-Hadron tracks.	96
339			
340			
341	Figure 69	The average reconstructed MDT β distribution for $Z \rightarrow \mu\mu$ events in which one of the muons is reconstructed as a slow muon, for both data and simulation. A gaussian fit is superimposed.	97
342			
343			
344			
345	Figure 70	The observed mass distribution of events in data and the generated background distribution in (a) the stable and (b) the metastable signal region. A few example simulated signal distributions are superimposed.	98
346			
347			
348			
349	Figure 71	The observed and expected cross section limits as a function of mass for the stable simulated signal. The predicted cross section values for the corresponding signals are included.	101
350			
351			
352			
353	Figure 72	The observed and expected cross section limits as a function of mass for each generated lifetime. The predicted cross section values for the corresponding signals are included.	102
354			
355			
356			

- 357 **Figure 73** The excluded range of masses as a function of gluino
358 lifetime. The expected lower limit (LL), with its exper-
359 imental $\pm 1\sigma$ band, is given with respect to the nominal
360 theoretical cross-section. The observed 95% LL ob-
361 tained at $\sqrt{s} = 8$ TeV [61] is also shown for comparison.¹⁰⁴
362 **Figure 74** The constraints on the gluino mass as a function of
363 lifetime for a split-supersymmetry model with the gluino
364 R-Hadrons decaying into a gluon or light quarks and
365 a neutralino with mass of 100 GeV. The solid lines in-
366 dicate the observed limits, while the dashed lines in-
367 dicate the expected limits. The area below the curves
368 is excluded. The dots represent results for which the
369 particle is assumed to be prompt or stable.¹⁰⁵

370 LIST OF TABLES

371	Table 1	The design parameters of the LHC beam that determines the energy of collisions and the luminosity, for both the injection of protons and at the nominal circulation.	22
372			
373			
374			
375	Table 2	The dominant sources of corrections and systematic uncertainties in the JES estimation technique, including typical values for the correcting shift (Δ) and the associated uncertainty (σ).	57
376			
377			
378			
379	Table 3	The expected number of events at each level of the selection for metastable 1600 GeV, 10 ns R-Hadrons, along with the number of events observed in data, for 3.2 fb^{-1} . The simulated yields are shown with statistical uncertainties only. The total efficiency \times acceptance is also shown for the signal.	83
380			
381			
382			
383			
384			
385	Table 4	A summary of the sources of systematic uncertainty for the data-driven background in the signal region. If the uncertainty depends on the mass, the maximum values are reported.	91
386			
387			
388			
389	Table 5	A summary of the sources of systematic uncertainty for the simulated signal yield. The uncertainty depends on the mass and lifetime, and the maximum negative and positive values are reported in the table.	93
390			
391			
392			
393	Table 6	Example of the contributing systematic variations to the total systematic for the E_T^{miss} Scale, as measured in a 1200 GeV, Stable R-Hadron signal sample.	95
394			
395			
396	Table 7	The estimated number of background events and the number of observed events in data for the specified selection regions prior to the requirement on mass. The background estimates show statistical and systematic uncertainties.	98
397			
398			
399			
400			
401	Table 8	The left and right extremum of the mass window for each generated mass point with a 10 ns lifetime.	99
402			
403	Table 9	The left and right extremum of the mass window used for each generated stable mass point.	99
404			
405	Table 10	The expected number of signal events, the expected number of background events, and the observed number of events in data with their respective statistical errors within the respective mass window for each generated stable mass point	100
406			
407			
408			
409			

410	Table 11	The expected number of signal events, the expected number of background events, and the observed number of events in data with their respective statistical errors within the respective mass window for each generated mass point with a lifetime of 10 ns.	100
411			
412			
413			
414			
415	Table 12	The observed and expected 95% CL lower limit on mass for gluino R-Hadrons for each considered lifetime.	103
416			
417	Table 13	The left and right extremum of the mass window for each generated mass point with a 50 ns lifetime.	115
418			
419	Table 14	The left and right extremum of the mass window for each generated mass point with a 30 ns lifetime.	115
420			
421	Table 15	The left and right extremum of the mass window for each generated mass point with a 10 ns lifetime.	116
422			
423	Table 16	The left and right extremum of the mass window used for each generated mass point with a lifetime of 3 ns.	116
424			
425	Table 17	The left and right extremum of the mass window used for each mass point with a lifetime of 1 ns.	116
426			
427	Table 18	The left and right extremum of the mass window for each generated mass point with a lifetime of 0.4 ns.	117
428			
429	Table 19	The left and right extremum of the mass window used for each generated stable mass point.	117
430			
431	Table 20	The expected number of signal events, the expected number of background events, and the observed number of events in data with their respective statistical errors within the respective mass window for each generated mass point with a lifetime of 50 ns.	117
432			
433			
434			
435			
436	Table 21	The expected number of signal events, the expected number of background events, and the observed number of events in data with their respective statistical errors within the respective mass window for each generated mass point with a lifetime of 30 ns.	118
437			
438			
439			
440			
441	Table 22	The expected number of signal events, the expected number of background events, and the observed number of events in data with their respective statistical errors within the respective mass window for each generated mass point with a lifetime of 10 ns.	118
442			
443			
444			
445			
446	Table 23	The expected number of signal events, the expected number of background events, and the observed number of events in data with their respective statistical errors within the respective mass window for each generated mass point with a lifetime of 3 ns.	119
447			
448			
449			
450			
451	Table 24	The expected number of signal events, the expected number of background events, and the observed number of events in data with their respective statistical errors within the respective mass window for each generated mass point with a lifetime of 1 ns.	119
452			
453			
454			
455			

456	Table 25	The expected number of signal events, the expected number of background events, and the observed number of events in data with their respective statistical errors within the respective mass window for each generated mass point with a lifetime of p4 ns.	120
457			
458			
459			
460			
461	Table 26	The expected number of signal events, the expected number of background events, and the observed number of events in data with their respective statistical errors within the respective mass window for each generated stable mass point	120
462			
463			
464			
465			

467 ACRONYMS

- 468 SM Standard Model
469 CERN European Organization for Nuclear Research
470 SUSY Supersymmetry
471 LSP Lightest Supersymmetric Particle
472 LHC Large Hadron Collider
473 ATLAS A Toroidal LHC ApparatuS
474 CMS Compact Muon Solenoid
475 ALICE A Large Ion Collider Experiment
476 LHCb Large Hadron Collider beauty experiment
477 LEP the Large Electron Positron collider
478 PS Proton Synchrotron
479 PSB Proton Synchrotron Booster
480 SPS Super Proton Synchrotron
481 ToT time over threshold
482 LCW local cluster weighted
483 MIP minimally ionizing particle
484 EPJC European Physical Journal C
485 JES jet energy scale
486 LLP Long-Lived Particle
487 CR Control Region
488 NLO next-to-leading order
489 NLL next-to-leading logarithmic
490 PDF parton distribution function
491 ISR initial state radiation
492 RMS root mean square
493 IBL Insertible B-Layer

⁴⁹⁴ CP Combined Performance

⁴⁹⁵ MDT Monitored Drift Tube

⁴⁹⁶ RF radiofrequency

497

PART I

498

INTRODUCTION

499

You can put some informational part preamble text here.

1

500

501 INTRODUCTION

502

PART II

503

THEORETICAL CONTEXT

504

You can put some informational part preamble text here.

2

505

506 STANDARD MODEL

507 The SM of particle physics seeks to explain the symmetries and interactions of
508 all currently discovered fundamental particles. It has been tested by several genera-
509 tions of experiments and has been remarkably successful, no significant de-
510 viations have been found. The SM provides predictions in particle physics for
511 interactions up to the Planck scale (10^{15} - 10^{19} GeV).

512 The theory itself is a quantum field theory grown from an underlying $SU(3) \times$
513 $SU(2) \times U(1)$ that requires the particle content and quantum numbers consist-
514 ent with experimental observations (see Section 2.1). Each postulated symme-
515 try is accompanied by an interaction between particles through gauge invari-
516 ance. These interactions are referred to as the Strong, Weak, and Electromag-
517 netic forces, which are discussed in Section 2.2.

518 Although this model has been very predictive, the theory is incomplete; for
519 example, it is not able to describe gravity or astronomically observed dark matter.
520 These limitations are discussed in more detail in Section 2.3.

521 21 PARTICLES

522 The most familiar matter in the universe is made up of protons, neutrons, and
523 electrons. Protons and neutrons are composite particles, however, and are made
524 up in turn by particles called quarks. Quarks carry both electric charge and color
525 charge, and are bound in color-neutral combinations called baryons. The elec-
526 tron is an example of a lepton, and carries only electric charge. Another type
527 of particle, the neutrino, does not form atomic structures in the same way that
528 quarks and leptons do because it carries no color or electric charge. Collectively,
529 these types of particles are known as fermions, the group of particles with half-
530 integer spin.

531 There are three generations of fermions, although familiar matter is formed
532 predominantly by the first generation. The generations are identical except for
533 their masses, which increase in each generation by convention. In addition, each
534 of these particles is accompanied by an antiparticle, with opposite-sign quantum
535 numbers but the same mass.

536 The fermions comprise what is typically considered matter, but there are
537 additional particles that are mediators of interactions between those fermions.
538 These mediators are known as the gauge bosons, gauge in that their existence
539 is required by gauge invariance (discussed further in Section 2.2) and bosons in
540 that they have integer spin. The boson which mediates the electromagnetic force
541 is the photon, the first boson to be discovered; it has no electric charge, no mass,
542 and a spin of 1. There are three spin-1 mediators of the weak force, the two
543 W bosons and the Z boson. The W bosons have electric charge of ± 1 and a
544 mass of 80.385 ± 0.015 GeV, while the Z boson is neutral and has a mass of

545 91.1876 \pm 0.0021 GeV. The strong force is mediated by eight particles called
 546 gluons, which are massless and electrically neutral but do carry color charge.

547 The final particle present in the SM is the Higgs boson, which was recently
 548 observed for the first time by experiments at CERN in 2012. It is electrically
 549 neutral, has a mass of 125.7 \pm 0.4 GeV, and is the only spin-0 particle yet to be
 550 observed. The Higgs boson is the gauge boson associated with the mechanism
 551 that gives a mass to the W and Z bosons.

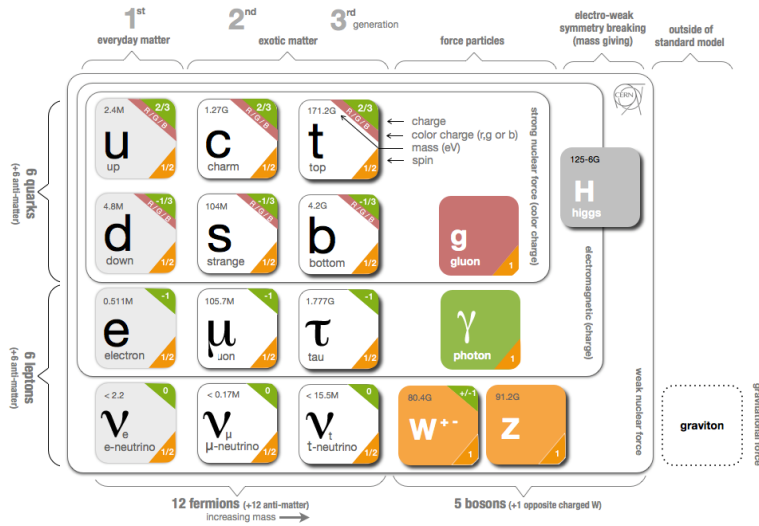


Figure 1: The particle content of the SM.

552 Together these particles form the entire content of the SM, and are summa-
 553 rized in Figure 1. These are the particles that constitute the observable universe
 554 and all the so-far-observed interactions within it.

555 2.2 INTERACTIONS

556 The interactions predicted and described by the SM are fundamentally tied to the
 557 particles within it, both in that they describe the way those particles can influence
 558 each other and also in that the existence of the interactions requires the existence
 559 of some particles (the gauge bosons).

560 2.3 LIMITATIONS

3

561

562 SUPERSYMMETRY

563 3.1 MOTIVATION

564 3.2 STRUCTURE

565 3.3 PHENOMENOLOGY

4

566

567 LONG-LIVED PARTICLES

568 4.1 MECHANISMS

569 4.1.1 EXAMPLES IN SUPERSYMMETRY

570 4.2 PHENOMENOLOGY

571 4.2.1 DISIMILARITIES TO PROMPT DECAYS

572 4.2.2 CHARACTERISTIC SIGNATURES

573

PART III

574

EXPERIMENTAL STRUCTURE AND RECONSTRUCTION

575

You can put some informational part preamble text here.

577 THE LARGE HADRON COLLIDER

578 The LHC, a two-ring superconducting hadron accelerator, provides high energy
579 proton-proton collisions for several large experiments at European Organization
580 for Nuclear Research (CERN) in Geneva, Switzerland [1, 2]. It is the largest,
581 highest-luminosity, and highest-energy proton collider ever built, and was con-
582 structed by a collaboration of more than 10,000 scientists from the more than
583 100 countries that contribute to CERN. The original design of the LHC focused on
584 providing collision energies of up to 14 TeV and generating enough collisions to
585 reveal physics beyond the SM which is predicted to exist at higher energy scales.

586 The LHC was installed in an existing 27 km tunnel at CERN which was origi-
587 nally designed to house the Large Electron Positron collider (LEP). This allows
588 the collider to use existing accelerators at the same complex to provide the initial
589 acceleration of protons up to 450 GeV before injecting into LHC. The injected
590 hadrons are accelerated up to as much as 14 TeV while being focused into two
591 beams traveling in opposite directions. During this process the protons circulate
592 around the tunnel millions of times, while the beams are intermittently crossed
593 at the four locations of the experiments to provide collisions. These collision
594 points correspond to the four major LHC experiments: ATLAS, Compact Muon
595 Solenoid (CMS), Large Hadron Collider beauty experiment (LHCb), and A Large
596 Ion Collider Experiment (ALICE), and Figure 2 shows the layout of the exper-
597 iments both on the surface and below. ATLAS and CMS are both general pur-
598 pose, high-luminosity detectors which search for a wide range of new types of
599 physics [3, 4]. LHCb studies the interactions of b-hadrons to explore the asymme-
600 try between matter and antimatter [5]. ALICE focuses on the collisions of lead
601 ions, which the LHC also provides, in order to study the properties of quark-
602 gluon plasma [6].

603 During the first five years of operation, after the LHC turned on in 2010, the
604 LHC has provided four major data collecting periods. In 2010 the LHC generated
605 collisions at several energies, starting at 900 GeV. It increased the energy from
606 900 GeV to 2.76 TeV and then subsequently to 7 TeV, with a peak luminos-
607 ity of $2 \times 10^{32} \text{ cm}^{-2}\text{s}^{-1}$, and a total delivered luminosity of 50 pb^{-1} . The next
608 run, during 2011, continued the operation at 7 TeV and provided an additional 5 fb^{-1}
609 with a peak luminosity of $4 \times 10^{33} \text{ cm}^{-2}\text{s}^{-1}$. The energy was then increased
610 to 8 TeV for the data collection during 2012, which provided 23 fb^{-1} with a peak
611 luminosity of $7.7 \times 10^{33} \text{ cm}^{-2}\text{s}^{-1}$. After the first long shutdown for 2013 and
612 2014, the LHC resumed operation and increased the energy to 13 TeV in 2015,
613 where it delivered 4.2 fb^{-1} with a peak luminosity of $5.5 \times 10^{33} \text{ cm}^{-2}\text{s}^{-1}$. The
614 LHC is currently providing additional 13 TeV collisions in 2016 with higher lu-
615 minosities than during any previous data collection periods. These running peri-
616 ods are summarized in Figure 3, which shows the total delivered luminosity over

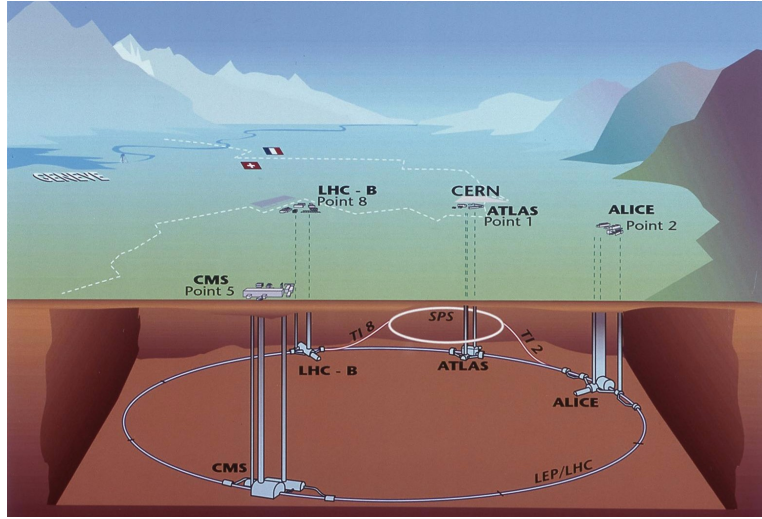


Figure 2: The four collision points and corresponding experiments of the [LHC](#). The image includes the location of the nearby city of Geneva as well as the border of France and Switzerland.

time for the [ATLAS](#) experiment during each of the four years of data collection since 2011.

5.1 INJECTION CHAIN

The [LHC](#) takes advantage of the presence of previously built accelerators at [CERN](#) to work up to the target energy in consecutive stages. The series of accelerators that feed into the [LHC](#) are known collectively as the injection chain, and together with the [LHC](#) form the accelerator complex. The full complex is illustrated in Figure 4, which details the complex series required to reach collisions of 13 or 14 TeV.

Protons at the [LHC](#) begin as hydrogen atoms in the Linac 2, a linear accelerator which replaced Linac 1 as the primary proton accelerator at [CERN](#) in 1978. In Linac 2, the hydrogen atoms are stripped of their electrons by a strong magnetic field, and the resulting protons are accelerated up to 50 MeV by cylindrical conductors charged by radio frequency cavities. The protons are then transferred to the Proton Synchrotron Booster ([PSB](#)), which uses a stack of four synchrotron rings to accelerate the protons up to 1.4 GeV. Then the protons are injected into the Proton Synchrotron ([PS](#)) which again uses synchrotron rings to bring the energy up to 25 GeV. The intermediate step between Linac 2 and the [PS](#) is not directly necessary, as the [PS](#) can accelerate protons starting from as low as 50 MeV. The inclusion of the [PSB](#) allows the [PS](#) to accept a higher intensity of injection and so increases the deliverable luminosity in the [LHC](#). The penultimate stage of acceleration is provided by the Super Proton Synchrotron ([SPS](#)), a large synchrotron with a 7 km circumference that was commissioned at [CERN](#) in 1976. During this step the protons increase in energy to 450 GeV, after which they can be directly injected into the [LHC](#).

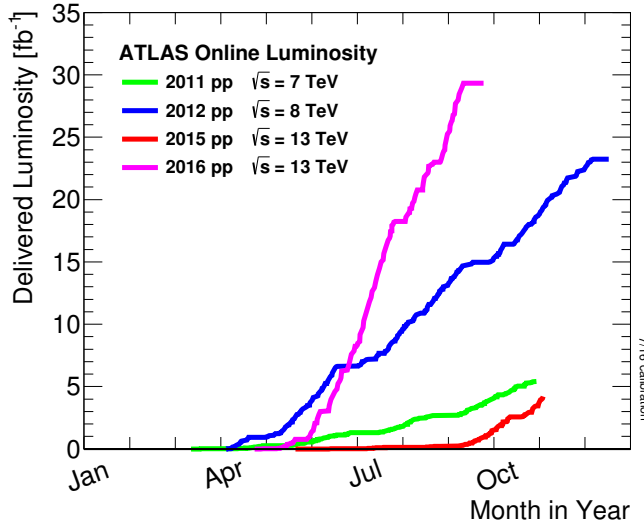


Figure 3: The cumulative luminosity over time delivered to the [ATLAS](#) experiment from high energy proton-proton collisions since 2011. The energies of the collisions are listed for each of the data-taking periods.

642 The final step is the [LHC](#) itself, which receives protons from the [SPS](#) into two
 643 separate beam pipes which circulate in opposite directions. The filling process
 644 at this steps takes approximately 4 minutes, and the subsequent acceleration to
 645 the final energy (6.5 TeV during 2015 and up to 7 TeV by design) takes approxi-
 646 mately half an hour. At this point the protons circulate around the circumference
 647 tens of thousands of times a second and continue for up to two hours.

648 5.2 DESIGN

649 5.2.1 LAYOUT

650 Many of the aspects of the [LHC](#) design are driven by the use of the existing [LEP](#)
 651 tunnel. This tunnel slopes gradually, with a 1.4% decline, with 90% of its length
 652 built into molasse rock which is particularly well suited to the application. The
 653 circumference is composed of eight 2987 meter arcs and eight 528 meter straight
 654 sections which connect them; this configuration is illustrated in Figure 5. The
 655 tunnel diameter is 3.7 m throughout its length.

656 The design energy is directly limited by the size of this tunnel, with its radius
 657 of curvature of 2804 m. A significant magnetic field is required to curve the
 658 protons around that radius of curvature; the relationship is given by

$$p \simeq 0.3BR \quad (1)$$

659 where p is the momentum of the particle in GeV, B is the magnetic field in Tesla,
 660 and R is the radius of curvature in meters. From the target design energy of
 661 14 TeV, or 7 TeV of momentum for protons in each beam, the required mag-
 662 netic field is 8.33 Tesla. This is too large a field strength to be practical with

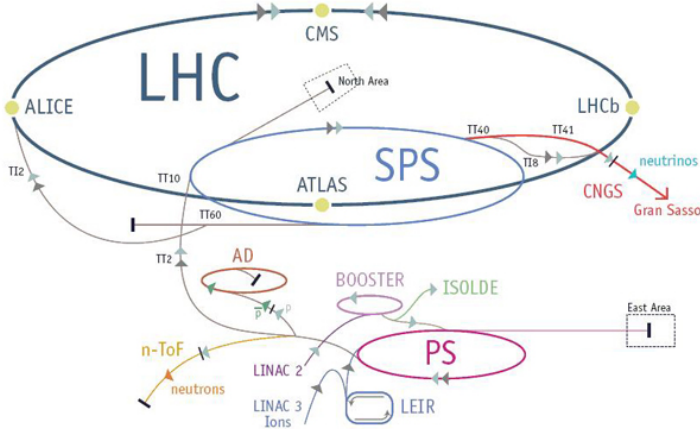


Figure 4: The accelerator complex that builds up to the full design energies at the [LHC](#). The protons are passed in order to Linac 2, the [PSB](#), the [PS](#), the [SPS](#) and then the [LHC](#).

663 iron electromagnets, because of the enormous power required and the resulting
 664 requirements for cooling. Because of these constraints, the [LHC](#) uses supercon-
 665 ducting magnets which can maintain that field strength with significantly less
 666 power consumption.

667 5.2.2 MAGNETS

668 Specifically the magnets chosen were Niobium and Titanium (NbTi) which al-
 669 low for field strengths as high as 10 Tesla when cooled down to 1.9 K. Reaching
 670 the target temperature of 1.9 K for all of the magnets requires superfluid helium
 671 and a large cryogenic system along the entire length of the tunnel. During nor-
 672 mal operation, the [LHC](#) uses 120 tonnes of helium within the magnets, and the
 673 entire system is cooled by eight cryogenic helium refrigerators. The tempera-
 674 ture increase that occurs during transit from the refrigerator along the beam
 675 necessitates that the refrigerators cool the helium down to 1.8 K. Any significant
 676 increase above this temperature range can remove the superconductive proper-
 677 ties of the magnets, which in turn generates drastically larger heat losses from
 678 the current within the magnets and causes a rapid rise in temperature called a
 679 quench.

680 In all there are approximately 8000 superconducting magnets distributed around
 681 the [LHC](#). The 1232 bending magnets, which keep the protons curving along the
 682 length of the beam, are twin bore cryodipoles, which allow both proton beams
 683 to be accommodated by one magnet and all of the associated cooling structure.
 684 Figure 6 shows the cross section of the design for these dipoles. The magnets are
 685 very large, 16.5 m long with a diameter of 0.57 meters and a total weight of 28
 686 tonnes. They are slightly curved, with an angle of 5.1 mrad, in order to carefully
 687 match the beam path. The twin bore accommodates both magnets inside the
 688 two 5 cm diameter holes which are surrounded by the superconducting coils.
 689 The coils require 12 kA of current in order to produce the required magnetic

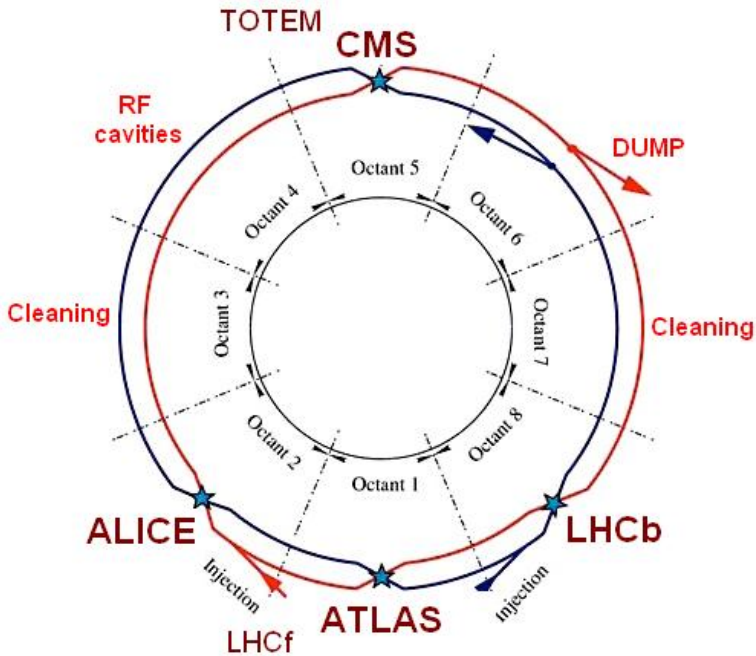


Figure 5: A schematic of the layout of the LHC, not to scale. The arched and straight sections are illustrated at the bottom of the schematic, and all four crossing sites are indicated with their respective experiments.

field. These coils are comprised of NbTi cable wound in two layers; the wire in the inner layer has a diameter of 1.065 mm while the wire in the outer layer has a diameter of 0.825 mm.

The large currents in the wires, along with the magnetic field produced, result in forces on the magnets which would tend to push them apart with over 10,000 Newtons per meter. Constraining the magnets requires a significant amount of structure including non-magnetic stainless steel collars. Both the presence of these electromagnetic forces and the varying thermal contraction coefficient of the pieces of the magnet produce significant forces on the cold mass structure. The cold mass is carefully engineered to so that these stresses do not significantly alter the magnetic field shape, which must be maintained between magnets to a precision of approximately 10^{-4} for successful operation.

The remaining 6800 magnets are a variety of quadrupole, sextapole, octopole, and single bore dipole magnets. These are used to damp oscillations, correct beam trajectories, focus the beams during circulation, and to squeeze the beams before collisions.

5.2.3 RF CAVITIES

Sixteen RF cavities produce the actual acceleration of the proton beam up to the design energy. These RF cavities are tuned to operate at 400 MHz, and are powered by high-powered electron beams modulated at the same frequency, called klystrons. The resonance within the cavity with the oscillating electric field establishes a voltage differential of 2 MV per cavity. The sixteen cavities are

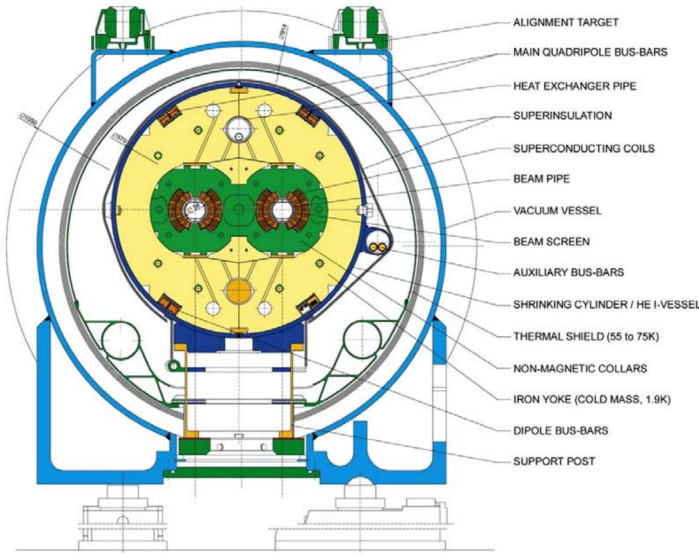


Figure 6: A cross section of the cryodipole magnets which bend the flight path of protons around the circumference of the LHC. The diagram includes both the superconducting coils which produce the magnetic field and the structural elements which keep the magnets precisely aligned.

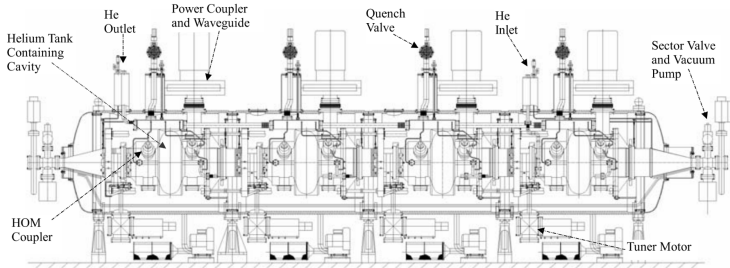


Figure 7: The arrangement of four RF cavities within a cryomodule.

712 split between the two beams, so combined the cavities provide 16 MV per beam,
 713 which accelerate the protons on each consecutive pass through the cavity. This
 714 acceleration is also necessary during circulation even after the target energy has
 715 been reached in order to compensate for losses from synchrotron radiation.

716 The cavities are arranged in cryomodules which contain four cavities, with
 717 two cryomodules per beam; this arrangement is illustrated in Figure 7. These
 718 cryomodules are necessary to maintain the superconducting state of the cavities,
 719 which are also constructed from niobium. The RF cavities use niobium along
 720 with copper to allow for low power losses in the superconductors. The copper
 721 provides a reduced susceptibility to quenching, as it rapidly conducts away heat
 722 generated by imperfections in the niobium, as well as natural shielding from the
 723 earth's magnetic field which can interfere with the RF system.

724 The nature of the radio frequency oscillations tends to group protons together
 725 into buckets. A proton traveling exactly in phase with the RF oscillations will not
 726 be displaced at all during a single circulation, and those slightly ahead or behind

727 of that phase will slightly decelerate or accelerate, respectively. This produces
 728 separate clusters of protons which arrive in phase to the cavities every 2.5 ns,
 729 corresponding to the 400 MHz frequency.

730 5.2.4 BEAM

731 The beams of protons circulate within 54 km of 5 cm diameter beam pipe. This
 732 entire structure is kept under vacuum at 1.9 K to prevent interactions between
 733 the beam pipe and the magnets as well as to prevent any interactions between the
 734 circulating protons and gas in the pipe. The vacuum within the pipe establishes
 735 a pressure as low as 10^{-9} mbar before the protons are introduced.

736 Because of the very high energies of the circulating protons, synchrotron ra-
 737 diation is not negligible in the bending regions. The protons are expected to
 738 radiate 3.9 kW per beam at 14 TeV, with 0.22 W/m, which is enough power to
 739 heat the liquid helium and cause a quench were it absorbed by the magnets. To
 740 prevent this, a copper screen is placed within the vacuum tube that absorb the
 741 emitted photons. This screen is kept between 5 and 20 K by the liquid helium
 742 cooling system.

743 5.3 LUMINOSITY PARAMETERS

744 In addition to the high energy of the collisions, the rate of collisions is extremely
 745 important to enabling the discovery of new physics. Many measurements and
 746 searches require a large number of events in order to be able to make statistically
 747 significant conclusions. The rate of collisions is measured using luminosity, the
 748 number of collisions per unit time and unit cross section for the proton-proton
 749 collisions. From the beam parameters, luminosity is given by

$$\mathcal{L} = \frac{N_b^2 n_b f_{rev} \gamma}{4\pi \epsilon_n \beta^*} F \quad (2)$$

750 where N_b is the number of protons per bunch, n_b is the number of bunches per
 751 beam, f_{rev} is the frequency of revolution, γ is the Lorentz factor for the protons
 752 at the circulating energy, ϵ_n is the emittance, β^* is the amplitude function at the
 753 collision point, and F is a geometric factor that accounts for the crossing angle of
 754 the beams at the collision point. The emittance measures the average spread of
 755 particles in both position and momentum space, while the amplitude function
 756 is a beam parameter which measures how much the beam has been squeezed.
 757 Together ϵ_n and β^* give the size of the beam in the transverse direction, $\sigma = \sqrt{\epsilon \beta^*}$. β
 758 changes over the length of the beam as the accessory magnets shape the
 759 distribution of protons, but only the value at the point of collisions, β^* , affects
 760 the luminosity.

761 The luminosity is maximized to the extent possible by tuning the parameters
 762 in Equation 2. A number of these are constrained by the design decisions. The
 763 revolution frequency is determined entirely by the length of the tunnel, as the

Parameter	Unit	Injection	Nominal
Beam Energy	TeV	0.450	7
Peak Instantaneous Luminosity	$\text{cm}^{-2}\text{s}^{-1}$	-	10^{34}
Bunch Spacing	ns	25	25
Number of Filled Bunches	-	2808	2808
Normalized Transverse Emittance	μm	3.75	3.75
Frequency	MHz	400.789	400.790
RF Voltage/Beam	MV	8	16
Stored Energy	MJ	-	362
Magnetic Field	T	0.54	8.33
Operating Temperature	K	1.9	1.9

Table 1: The design parameters of the [LHC](#) beam that determines the energy of collisions and the luminosity, for both the injection of protons and at the nominal circulation.

764 protons travel at very close to the speed of light. The geometric factor F is de-
 765 termined by the crossing angle of the beams at the collision points, again a com-
 766 ponent of the tunnel design; this angle is already very small at $285 \mu\text{rad}$, which
 767 helps to maximize the geometric factor.

768 The major pieces that can be adjusted are the number of protons per bunch,
 769 N_b , the number of bunches in the beam, n_b , and the amplitude function β . In-
 770 creasing either N_b or n_b increases the amount of energy stored in the beam,
 771 which presents a danger if control of the beam is lost. At design specifications,
 772 the beam stores 362 MJ, which is enough energy to damage the detectors or ac-
 773 celerator if the beam were to wander out of the beam pipe. So, the luminosity
 774 is primarily controlled at the [LHC](#) by adjusting β^* , where lowering β^* increases
 775 the luminosity. β^* is tuned to provide the various values of luminosity used at
 776 the [LHC](#) which can be raised to as much as 10^{34} .

777 The nominal bunch structure consists of 3654 bunches, each holding 10^{11} pro-
 778 tons, which cross a collision point in 25 ns. These are further subdivided into the
 779 buckets mentioned in Section 5.2.3 by the clustering properties of the [RF](#) cavities.
 780 The bunches are further grouped into trains of 72 bunches which are separated
 781 by a gap which would otherwise hold 12 bunches. At nominal operation 2808
 782 of the bunches will actually be filled with protons, while the remainder are left
 783 empty to form an abort gap that can be used in case the beam needs to be dumped.

784 The various beam parameters are summarized in Table 1 for the designed op-
 785 eration. In practice the beam has operated at lower energies and lower luminosi-
 786 ties than the design values, but the [LHC](#) is expected to operate at the full design
 787 values during Run 2.

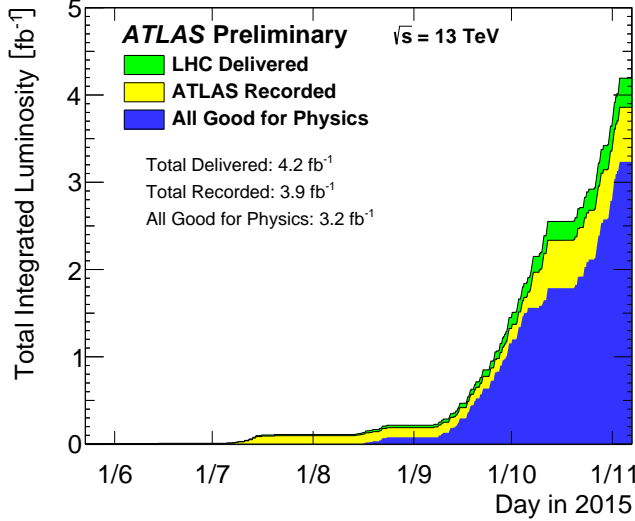


Figure 8: The cumulative luminosity versus time delivered to ATLAS (green), recorded by ATLAS (yellow), and certified to be good quality data (blue) during stable beams for pp collisions at 13 TeV in 2015.

5.4 DELIVERED LUMINOSITY

During the data collection of 2015, the [LHC](#) operated at luminosities as large as 5×10^{33} . It is convenient to refer to the integrated luminosity, the integral of the instantaneous luminosity, which corresponds directly to the number of delivered events for a given process.

$$N = \sigma \times \int \mathcal{L}(t) dt$$

where σ is the cross section for the process of interest. The integrated luminosity over time is shown in Figure 8. This includes the luminosity delivered by the [LHC](#) as well as the luminosity that was recorded by [ATLAS](#). Some of the delivered luminosity is not recorded because [ATLAS](#) is placed in standby until the [LHC](#) reports that the beam conditions are stable, and only then does [ATLAS](#) begin recording. The figure also includes the amount of luminosity marked as good for physics, which includes additional requirements on the operation of the detector during data collection that are necessary for precise measurements.

In addition to the instantaneous luminosity, the beam conditions also influence the number of collisions that occur within a single bunch crossing. The multiple interactions at each crossing are referred to as pileup, often denoted μ , and each of these interactions are present in a single measured event. Figure 9 shows the luminosity-weighted distribution of the mean number of interactions for events collected in 2015. The presence of as many as 20 events in a single collision provides a significant challenge in reconstructing events and isolating the targeted physical processes.

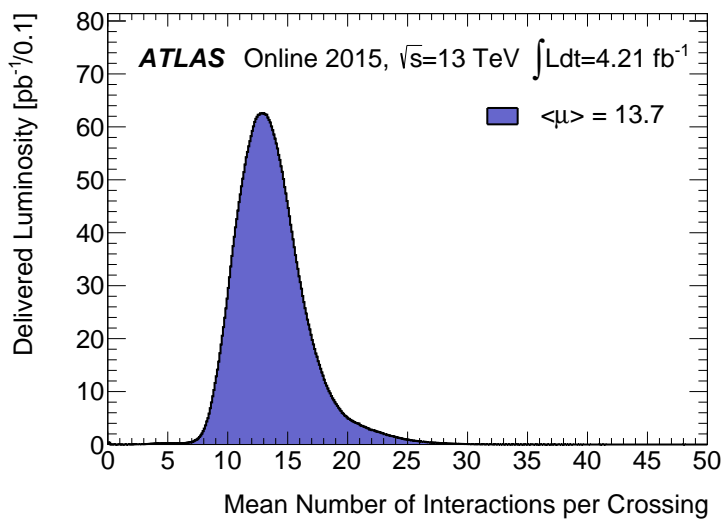


Figure 9: The luminosity-weighted distribution of the mean number of interactions per crossing for the 2015 pp collision data at 13 TeV.

805

806 THE ATLAS DETECTOR

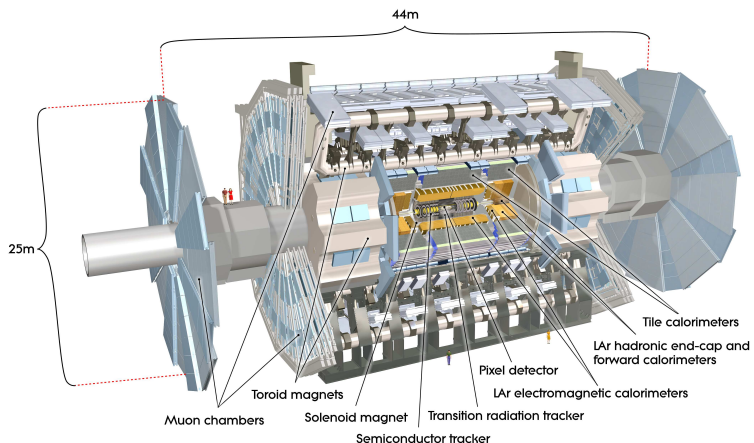


Figure 10

807 6.1 COORDINATE SYSTEM

808 6.2 MAGNETIC FIELD

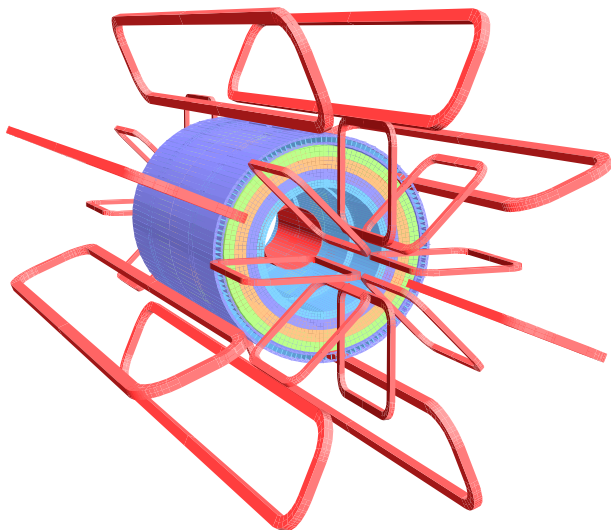


Figure 11

809 6.3 INNER DETECTOR

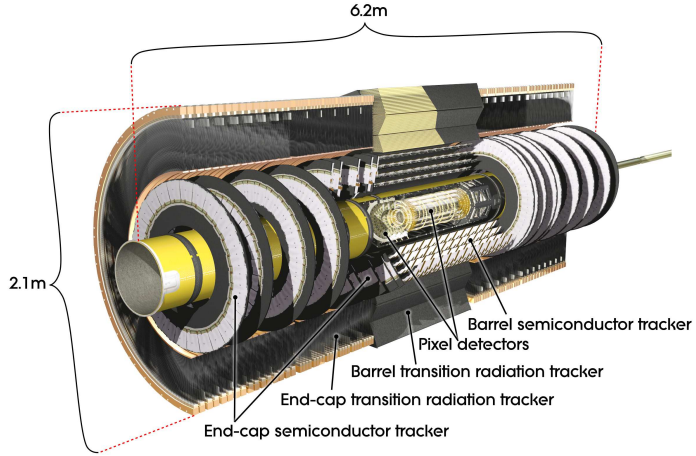


Figure 12

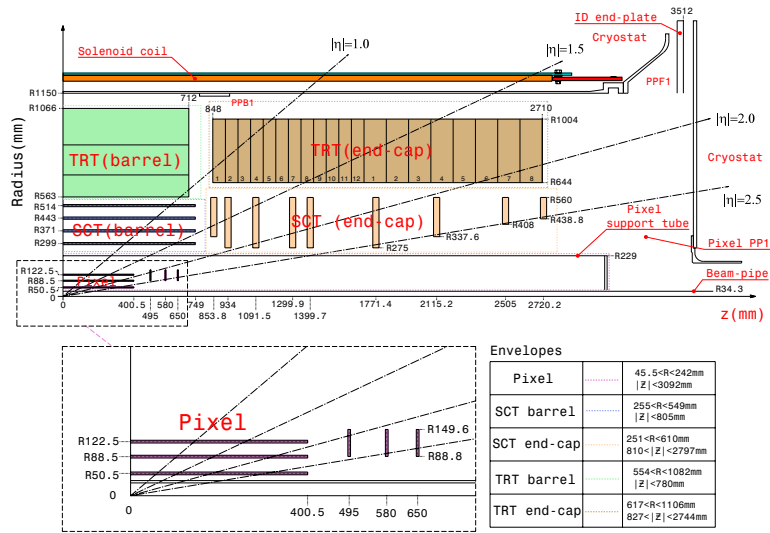


Figure 13

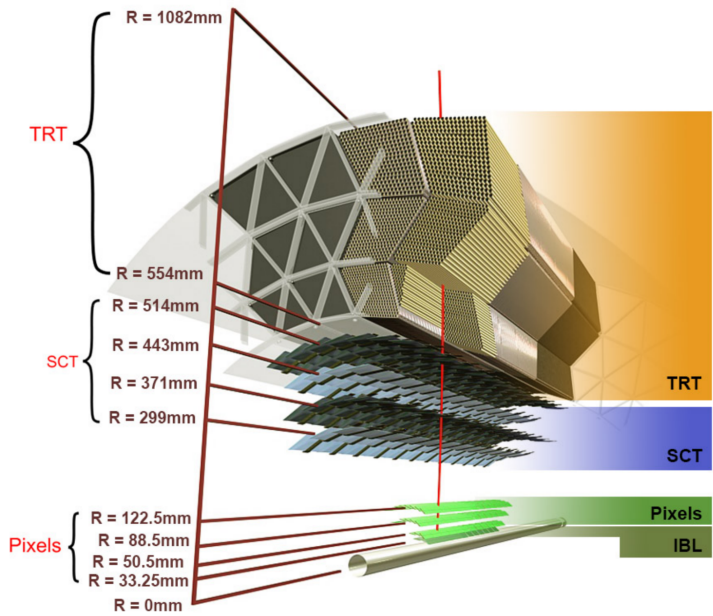


Figure 14

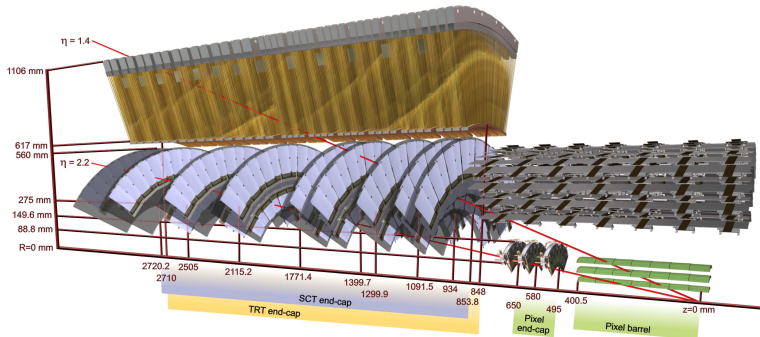


Figure 15

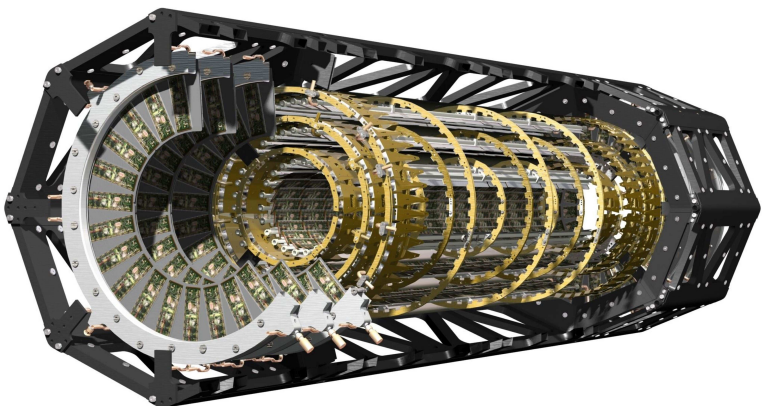


Figure 16

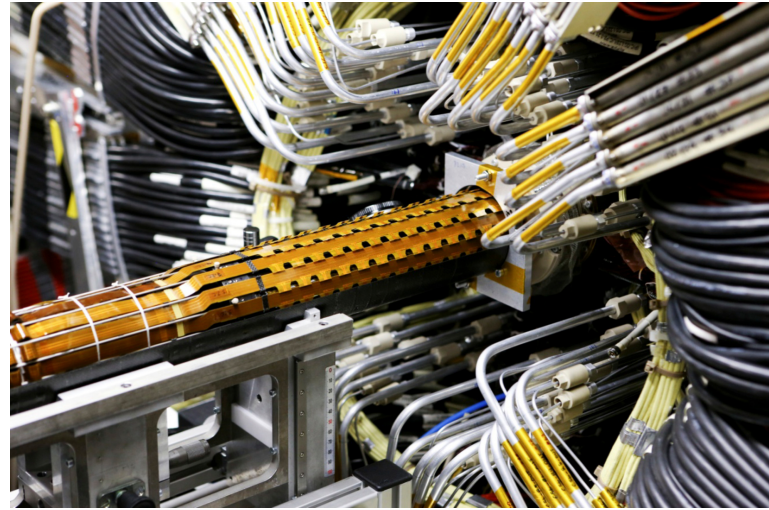


Figure 17

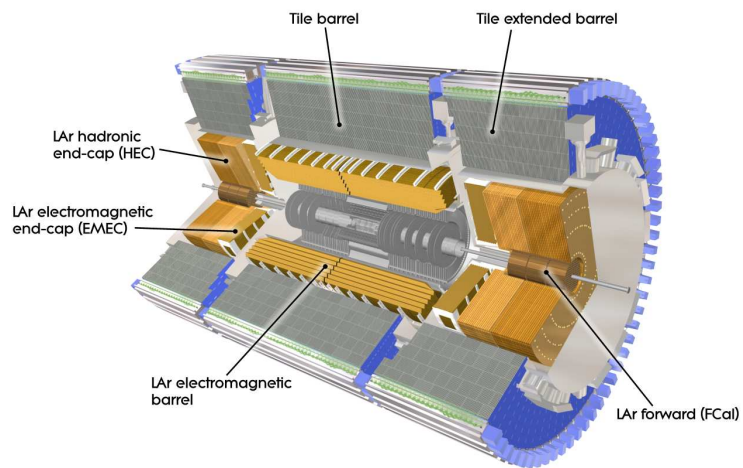


Figure 18

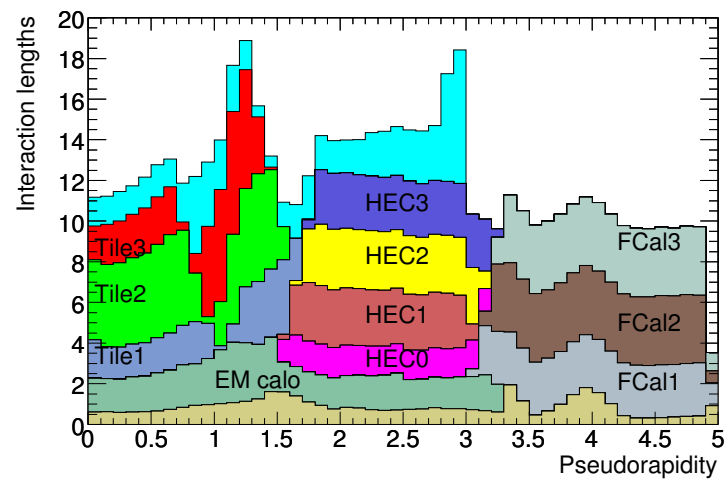


Figure 19

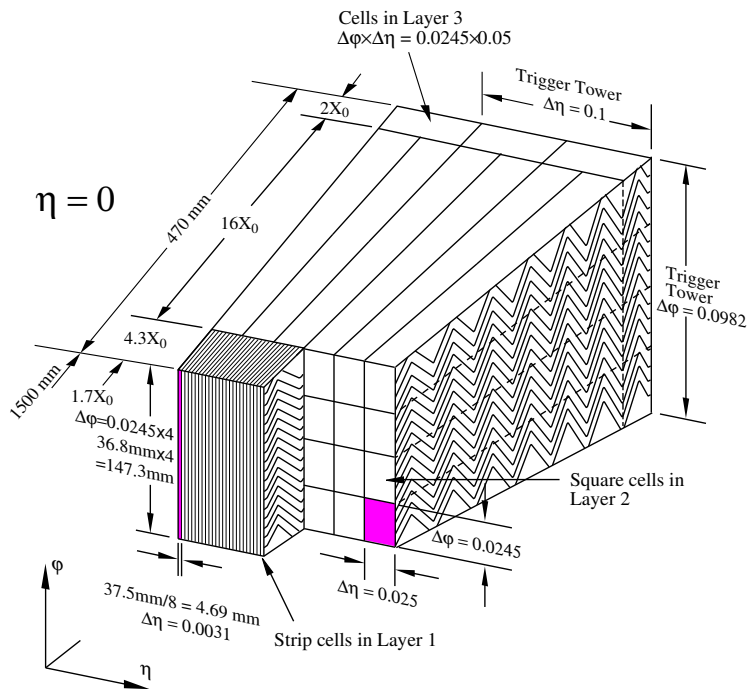


Figure 20

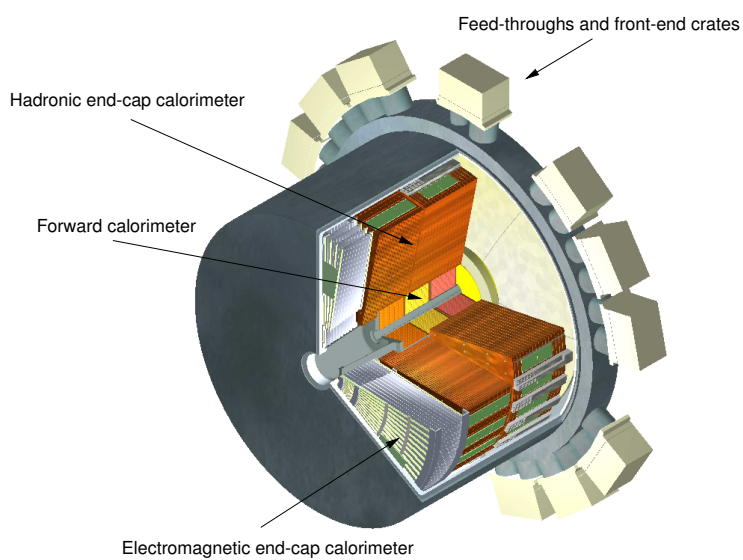


Figure 21

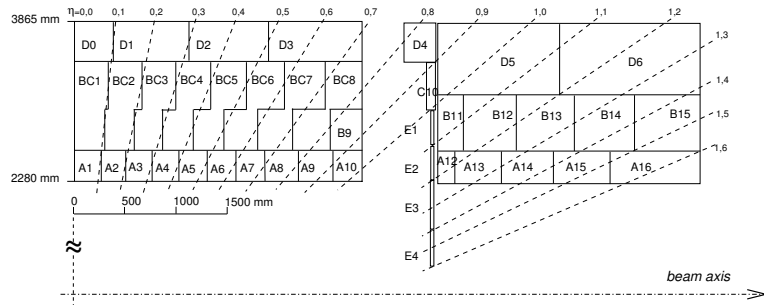


Figure 22

810 6.3.1 PIXEL DETECTOR

811 6.3.2 SEMICONDUCTOR TRACKER

812 6.3.3 TRANSITION RADIATION TRACKER

813 6.4 CALORIMETRY

814 6.4.1 ELECTROMAGNETIC CALORIMETERS

815 6.4.2 HADRONIC CALORIMETERS

816 6.4.3 FORWARD CALORIMETERS

817 6.5 MUON SPECTROMETER

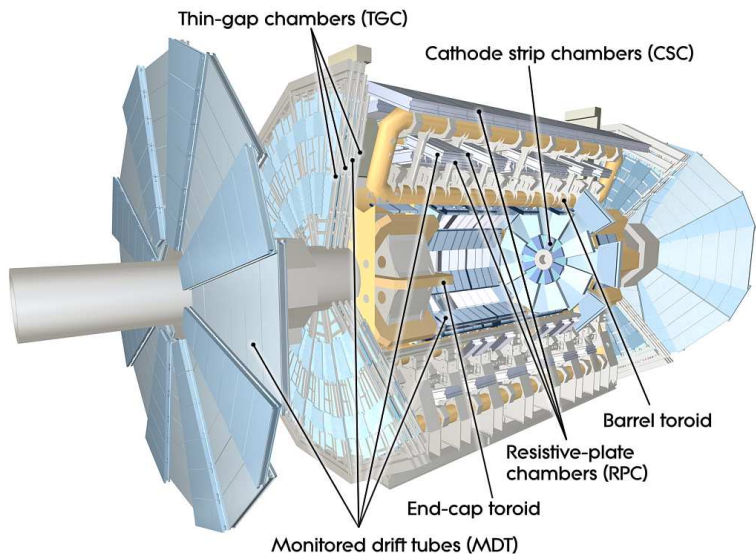


Figure 23

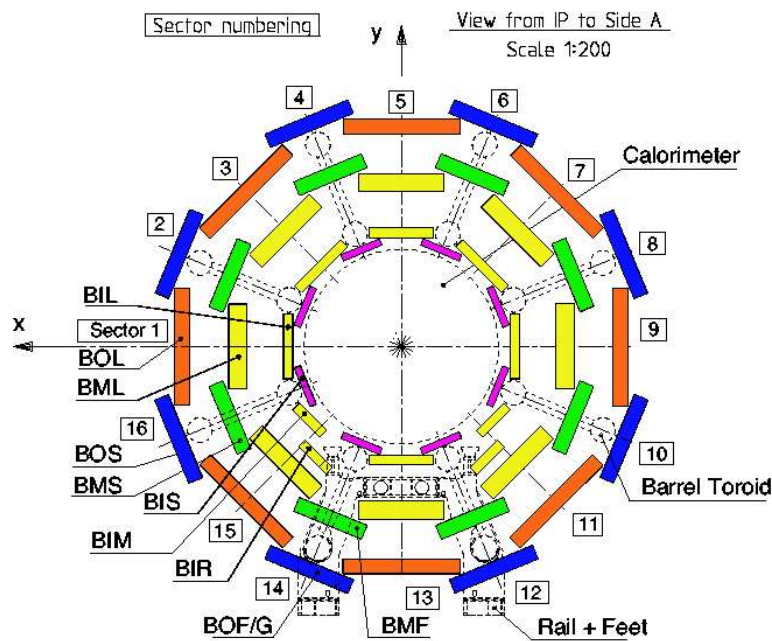


Figure 24

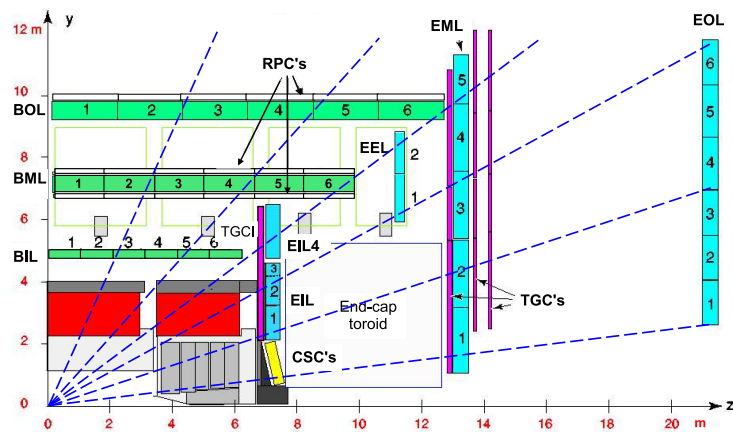


Figure 25

6.6 TRIGGER

6.6.1 TRIGGER SCHEME

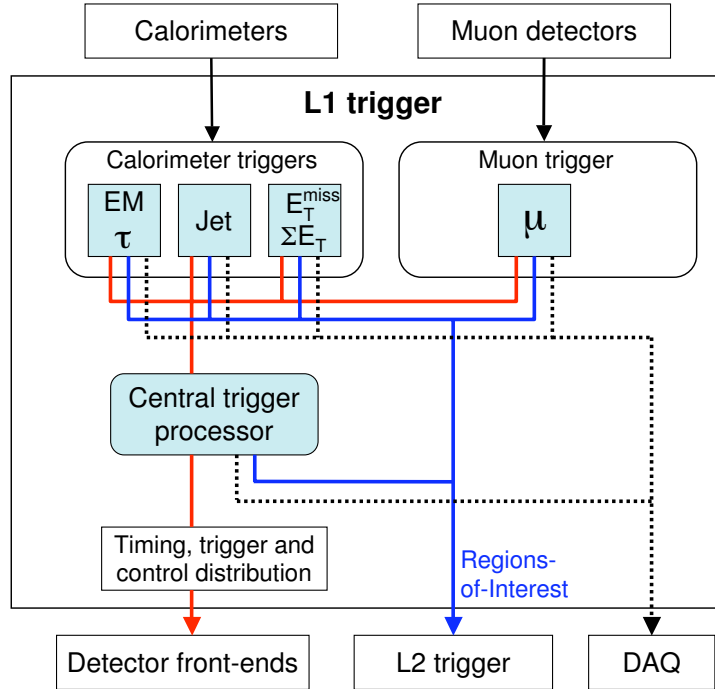


Figure 26

6.6.2 MISSING TRANSVERSE ENERGY TRIGGERS

7

821

822 EVENT RECONSTRUCTION

823 The ATLAS experiment combines measurements in the subdetectors to form a
824 cohesive picture of each physics event.

825 7.1 TRACKS AND VERTICES

826 7.1.1 TRACK RECONSTRUCTION

827 7.1.1.1 NEURAL NETWORK

828 7.1.1.2 PIXEL DE/DX

829 7.1.2 VERTEX RECONSTRUCTION

830 7.2 JETS

831 7.2.1 TOPOLOGICAL CLUSTERING

832 7.2.2 JET ENERGY SCALE

833 7.2.3 JET ENERGY SCALE UNCERTAINTIES

834 7.2.4 JET ENERGY RESOLUTION

835 7.3 ELECTRONS

836 7.3.1 ELECTRON IDENTIFICATION

837 7.4 MUONS

838 7.4.1 MUON IDENTIFICATION

839 7.5 MISSING TRANSVERSE ENERGY

840

PART IV

841

CALORIMETER RESPONSE

842

You can put some informational part preamble text here.

8

843

844 RESPONSE MEASUREMENT WITH SINGLE HADRONS

845 As discussed in Section 7.2, colored particles produced in collisions hadronize
846 into jets of multiple hadrons. One approach to understanding jet energy mea-
847 surements in the ATLAS calorimeters is to evaluate the calorimeter response to
848 those individual hadrons; measurements of individual hadrons can be used to
849 build up an understanding of the jets that they form. The redundancy of the
850 momentum provided by the tracking system and the energy provided by the
851 calorimeter provides an opportunity to study calorimeter response using real
852 collisions, as described further in Section 8.2.

853 Calorimeter response includes a number of physical effects that can be ex-
854 tracted to provide insight into many aspects of jet modeling. First, many charged
855 hadrons interact with the material of the detector prior to reaching the calorime-
856 ters and thus do not deposit any energy. Comparing this effect in data and simu-
857 lation is a powerful tool in validating the interactions of particles with the mate-
858 rial of the detector and the model of the detector geometry in simulation, see Sec-
859 tion 8.2.2. The particles which do reach the calorimeter deposit their energy into
860 several adjacent cells, which are then clustered together. The energy of the clus-
861 ter is then the total energy deposited by that particle. Comparing the response of
862 hadrons in data to that of simulated hadrons provides a direct evaluation of the
863 showering of hadronic particles and the energy deposited by particles in matter
(Section 8.2.4).

864 The above studies all use an inclusive selection of charged particles, which are
865 comprised predominantly of pions, kaons, and (anti)protons. It is also possible to
866 measure the response to various identified particle types separately to evaluate
867 the simulated interactions of each particle, particularly at low energies where
868 differences between species are very relevant. Pions and (anti)protons can be
869 identified through decays of long-lived particles, in particular Λ , $\bar{\Lambda}$, and K_S^0 , and
870 then used to measure response as described above. This is discussed in detail in
871 Section 8.3.

872 The results in this chapter use data collected at 7 and 8 TeV collected in 2010
873 and 2012, respectively. Both are included as the calorimeter was repaired and
874 recalibrated between those two data-taking periods. Both sets of data are com-
875 pared to an updated simulation that includes new physics models provided by
876 Geant4 [7] and improvements in the detector description [8, 9]. The present
877 results are published in European Physical Journal C (EPJC) [10] and can be com-
878 compared to a similar measurement performed in 2009 and 2010 [11], which used
879 the previous version of the simulation framework [12].

881 8.1 DATASET AND SIMULATION

882 8.1.1 DATA SAMPLES

883 The two datasets used in this chapter are taken from dedicated low-pileup runs
 884 where the fraction of events with multiple interactions was negligible. These
 885 datasets are used rather than those containing full-pileup events to facilitate mea-
 886 surement of isolated hadrons. The 2012 dataset at $\sqrt{s} = 8$ TeV contains 8 mil-
 887 lion events and corresponds to an integrated luminosity of 0.1 nb^{-1} . The 2010
 888 dataset at $\sqrt{s} = 7$ TeV contains 3 million events and corresponds to an inte-
 889 grated luminosity of 3.2 nb^{-1} . The latter dataset was also used for the 2010 re-
 890 sults [11], but it has since been reanalyzed with an updated reconstruction in-
 891 cluding the final, best understanding of the detector description for the material
 892 and alignment from Run 1.

893 8.1.2 SIMULATED SAMPLES

894 The two datasets above are compared to simulated single-, double-, and non-
 895 diffractive events generated with Pythia8 [13] using the A2 configuration of
 896 hadronization [14] and the MSTW 2008 parton-distribution function set [15,
 897 16]. The admixture of the single-, double-, and non-diffractive events uses the
 898 default relative contributions from Pythia8. The conditions and energies for
 899 the two simulations are chosen so that they match those of the corresponding
 900 dataset.

901 To evaluate the interaction of hadrons with detector material, the simulation
 902 uses two different collections of hadronic physics models, called physics lists, in
 903 Geant4 9.4 [17]. The first, QGSP_BERT, combines the Bertini intra-nuclear
 904 cascade [18–20] below 9.9 GeV, a parametrized proton inelastic model from 9.5
 905 to 25 GeV [21], and a quark-gluon string model above 12 GeV [22–26]. The
 906 second, FTFP_BERT, combines the Bertini intra-nuclear cascade [18–20] below
 907 5 GeV and the Fritiof model [27–30] above 4 GeV. In either list, Geant4 en-
 908 forces a smooth transition between models where multiple models overlap.

909 8.1.3 EVENT SELECTION

910 The event selection for this study is minimal, as the only requirement is selecting
 911 good-quality events with an isolated track. Such events are triggered by requir-
 912 ing at least two hits in the minimum-bias trigger scintillators. After trigger, each
 913 event is required to have exactly one reconstructed vertex, and that vertex is re-
 914 quired to have four or more associated tracks.

915 The particles which are selected for the response measurements are first iden-
 916 tified as tracks in the inner detector. The tracks are required to have at least 500
 917 MeV of transverse momentum. To ensure a reliable momentum measurement,
 918 these tracks are required to have at least one hit in the pixel detector, six hits in
 919 the SCT, and small longitudinal and transverse impact parameters with respect
 920 to the primary vertex [11]. For the majority of the measurements in this chapter,

the track is additionally required to have 20 hits in the TRT, which significantly reduces the contribution from tracks which undergo nuclear interactions. This requirement and its effect is discussed in more detail in Section 8.2.5. In addition, tracks are rejected if there is any other reconstructed track which extrapolates to the calorimeter within a cone of $\Delta R = \sqrt{(\Delta\phi)^2 + (\Delta\eta)^2} < 0.4$. This requirement guarantees that the contamination of energy from nearby charged particles is negligible [11].

8.2 INCLUSIVE HADRON RESPONSE

The calorimeter response is more precisely defined as the ratio of the measured calorimeter energy to the true energy carried by the particle, although this true energy is unknown. For charged particles, however, the inner detector provides a very precise measurement of momentum (with uncertainty less than 1%) that can be used as a proxy for true energy. The ratio of the energy deposited by the charged particle in the calorimeter, E , to its momentum measured in the inner detector p , forms the calorimeter response measure called E/p . Though the distribution of E/p contains a number of physical features, this study focuses on the trends in two aggregated quantities: $\langle E/p \rangle$, the average of E/p for the selected tracks, and the zero fraction, the fraction of tracks with no associated energy in the calorimeter for those tracks.

The calorimeter energy assigned to a track is defined using clusters. The clusters are formed using a 4–2–0 algorithm [31] that begins with seeds requiring at least 4 times the average calorimeter cell noise. The neighboring cells with at least twice that noise threshold are then added to the cluster, and all bounding cells are then added with no requirement. This algorithm minimizes noise contributions through its seeding process, and including the bounding cells improves the energy resolution [32]. The clusters are associated to a given track if they fall within a cone of $\Delta R = 0.2$ of the extrapolated position of the track, which includes about 90% of the energy on average [11]. This construction is illustrated in Figure 27.

8.2.1 E/P DISTRIBUTION

The E/p distributions measured in both data and simulation are shown in Figure 28 for two example bins of track momentum and for tracks in the central region of the detector. These distributions show several important features of the E/p observable. The large content in the bin at $E = 0$ comes from tracks that have no associated cluster, which occurs due to interactions with detector material prior to reaching the calorimeter or the energy deposit being insufficiently large to generate a seed, and are discussed in Section 8.2.2. The small negative tail also comes from tracks that do not deposit any energy in the calorimeter but are randomly associated to a cluster with an energy below the noise threshold. The long positive tail above 1.0 comes from the contribution of neutral particles. Nearby neutral particles deposit (sometimes large) additional energy in the calorimeter but do not produce tracks in the inner detector, so they cannot be

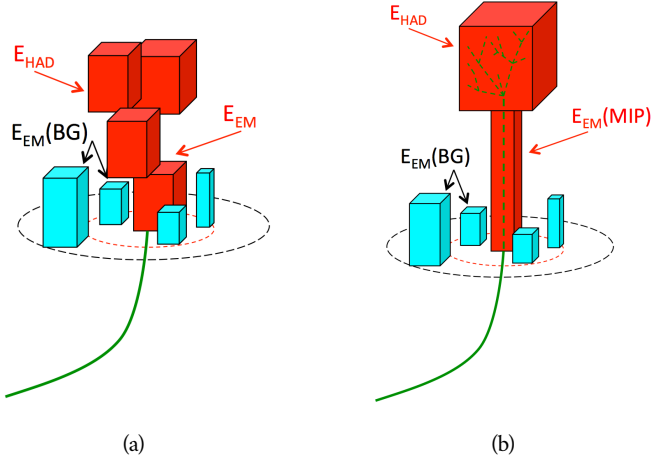


Figure 27: An illustration (a) of the E/p variable used throughout this paper. The red energy deposits come from the charged particle targeted for measurement, while the blue energy deposits are from nearby neutral particles and must be subtracted. The same diagram (b) for the neutral-background selection, described in Section 8.2.3.

963 rejected by the track isolation requirement. Additionally the peak and mean of
964 the distribution falls below 1.0 because of the loss of energy not found within
965 the cone as well as the non-compensation of the calorimeter.

The data and simulation share the same features, but the high and low tails are significantly different. The simulated events tend to overestimate the contribution of neutral particles to the long tail, an effect which can be isolated and removed as discussed in Section 8.2.3. Additionally, the simulated clusters have less noise on average, although this is a small effect on the overall response.

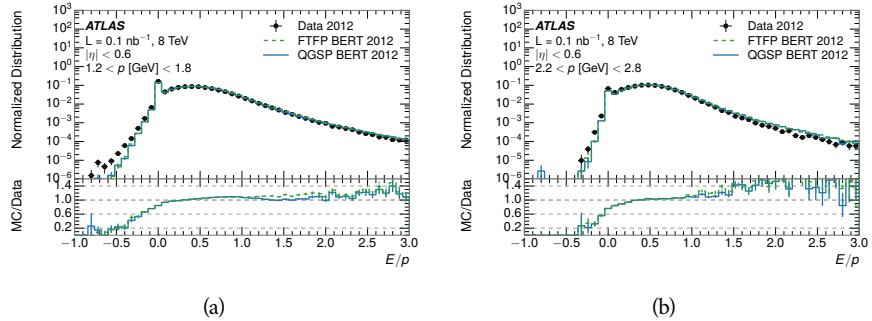


Figure 28: The E/p distribution and ratio of simulation to data for isolated tracks with (a) $|\eta| < 0.6$ and $1.2 < p/\text{GeV} < 1.8$ and (b) $|\eta| < 0.6$ and $2.2 < p/\text{GeV} < 2.8$.

971 8.2.2 ZERO FRACTION

972 The fraction of particles with no associated clusters, or similarly those with $E \leq$
 973 0, reflects the modeling of both the detector geometry and hadronic interactions.

974 The zero fraction is expected to rise as the amount of material a particle traverses
 975 increases, while it is expected to decrease as the particle energy increases. This
 976 dependence can be seen in Figure 29, where the zero fraction in data and simulation
 977 is shown as a function of momentum and the amount of material measured
 978 in interaction lengths. The trends are similar between 2010 and 2012 and for
 979 positively and negatively charged particles. The zero fraction decreases with
 980 energy as expected. The absolute discrepancy in zero fraction decreases with
 981 momentum from 5% to less than 1%, but this becomes more pronounced in the
 982 ratio as the zero fraction shrinks quickly with increasing momentum. There is
 983 a small constant difference between the data and simulation in both interaction
 984 models that becomes more pronounced. The amount of material in the detector
 985 increases with η , which is used to obtain results for interaction lengths ranging
 986 between 0.1 and 0.65 λ . As the data and simulation have significant disagree-
 987 ment in the zero fraction over a number of interaction lengths, the difference
 988 must be primarily from the modeling of hadronic interactions with detector ma-
 989 terial and not just the detector geometry. Although two different hadronic in-
 990 teraction models are shown in the figure, they have very similar discrepancies to
 991 data because both use the same description (the BERT model) at low momentum.

992 8.2.3 NEUTRAL BACKGROUND SUBTRACTION

993 The isolation requirement on hadrons is only effective in removing an energy
 994 contribution from nearby charged particles. Nearby neutral particles, predomi-
 995 nantly photons from π^0 decays, also add their energy to the calorimeter clusters,
 996 but mostly in the electromagnetic calorimeter. It is possible to measure this con-
 997 tribution, on average, using late-showering hadrons that minimally ionize in the
 998 electromagnetic calorimeter. Such particles are selected by requiring that they
 999 deposit less than 1.1 GeV in the EM calorimeter within a cone of $\Delta R < 0.1$
 1000 around the track. To ensure that these particles are well measured, they are addi-
 1001 tionally required to deposit between 40% and 90% of their energy in the hadronic
 1002 calorimeter within the same cone.

1003 These particles provide a clean sample to measure the nearby neutral back-
 1004 ground because they do not deposit energy in the area immediately surrounding
 1005 them in the EM calorimeter, as shown in Figure 27. So, the energy deposits in the
 1006 region $0.1 < \Delta R < 0.2$ can be attributed to neutral particles alone. To estimate
 1007 the contribution to the whole cone considered for the response measurement,
 1008 that energy is scaled by a geometric factor of $4/3$. This quantity, $\langle E/p \rangle_{BG}$, mea-
 1009 sured in aggregate over a number of particles, gives the contribution to $\langle E/p \rangle$
 1010 from neutral particles in the EM calorimeter. Similar techniques were used in
 1011 the individual layers of the hadronic calorimeters to show that the background
 1012 from neutrals is negligible in those layers [11].

1013 The distribution of this background estimate is shown in Figure 30 for data
 1014 and simulation with the two different physics lists. The contribution from neu-
 1015 tral particles falls from 0.1 at low momentum to around 0.03 for particles above
 1016 7 GeV. Although the simulation captures the overall trend, it significantly over-
 1017 estimates the neutral contribution for tracks with momentum between 2 and 8

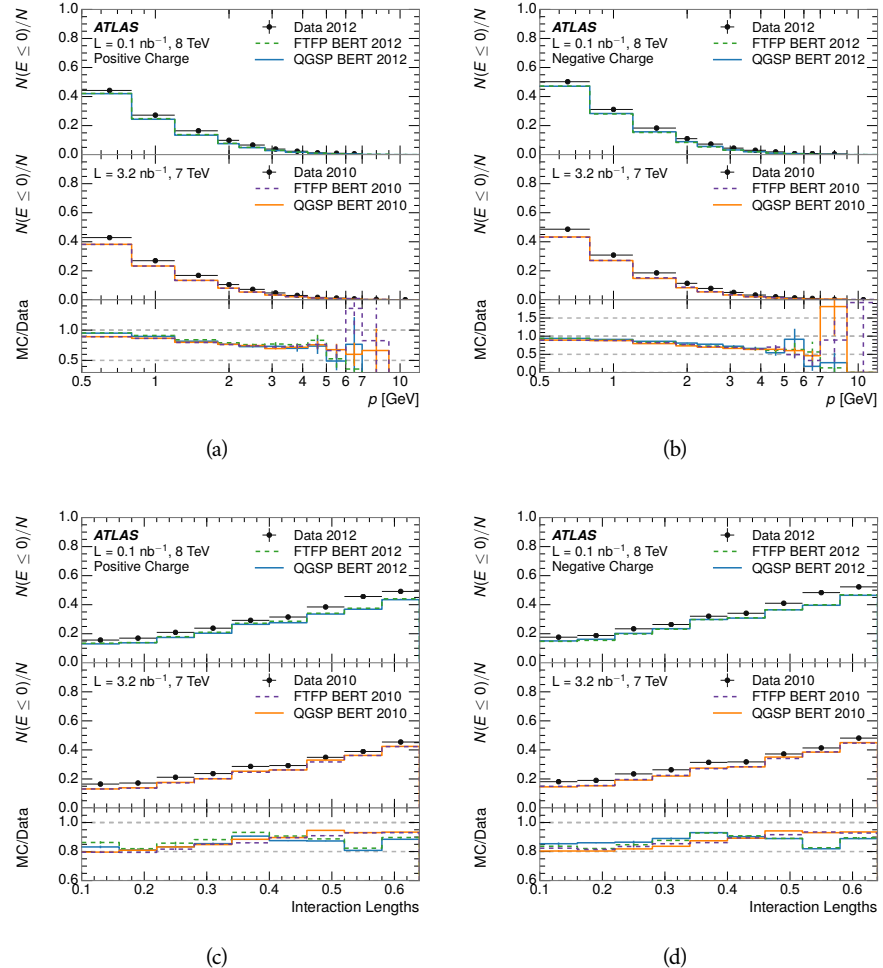


Figure 29: The fraction of tracks as a function (a, b) of momentum, (c, d) of interaction lengths with $E \leq 0$ for tracks with positive (on the left) and negative (on the right) charge.

1018 GeV. This effect was also seen in the tails of the E/p distributions in Figure 28.
 1019 This difference is likely due to modeling of coherent neutral particle radiation
 1020 in **Pythia8** that overestimates the production of π^0 near the production of the
 1021 charged particles. The discrepancy does not depend on η and thus is unlikely to
 1022 be a mismodeling of the detector. This difference can be subtracted to form a
 1023 corrected average E/p , as in Section 8.2.4.

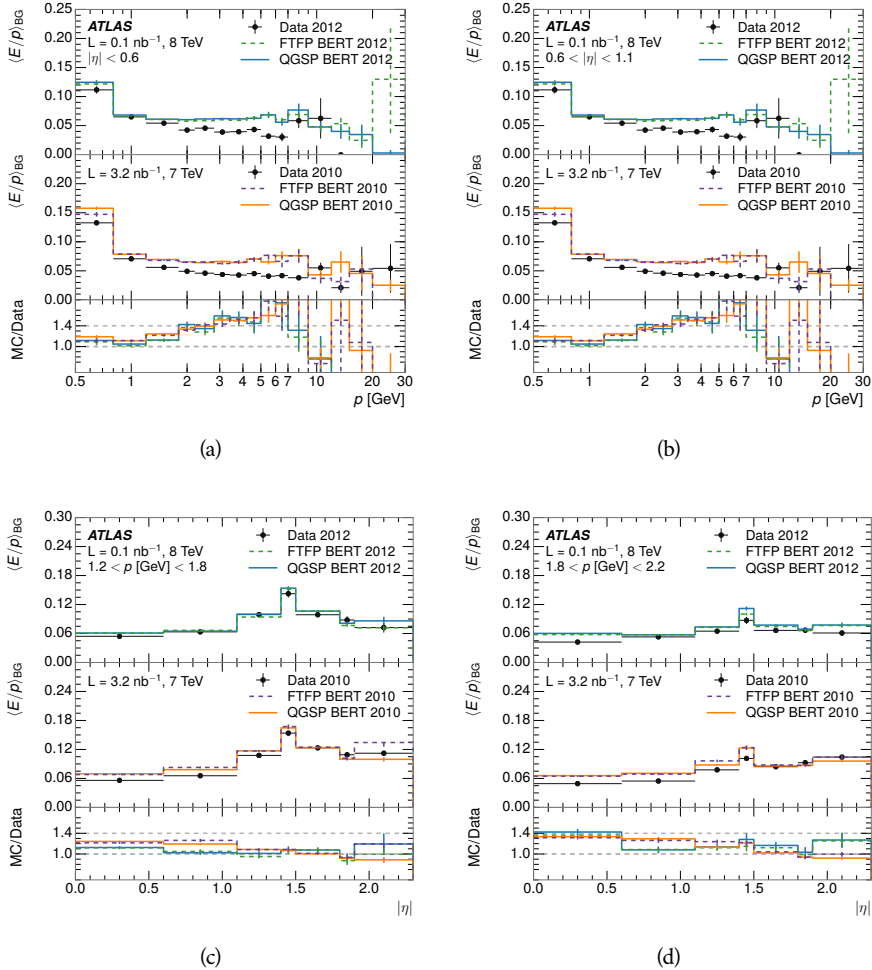


Figure 30: $\langle E/p \rangle_{BG}$ as a function of the track momentum for tracks with (a) $|\eta| < 0.6$,
 (b) $0.6 < |\eta| < 1.1$, and as a function of the track pseudorapidity for tracks
 with (c) $1.2 < p/\text{GeV} < 1.8$, (d) $1.8 < p/\text{GeV} < 2.2$.

1024 8.2.4 CORRECTED RESPONSE

1025 Figure 31 shows $\langle E/p \rangle_{COR}$ as a function of momentum for several bins of pseudo-
 1026 rapidity. This corrected $\langle E/p \rangle_{COR} \equiv \langle E/p \rangle - \langle E/p \rangle_{BG}$ measures the average
 1027 calorimeter response without the contamination of neutral particles. It is the
 1028 most direct measurement of calorimeter response in that it is the energy mea-
 1029 sured for fully isolated hadrons. The correction is performed separately in data
 1030 and simulation, so that the mismodeling of the neutral background in simulation

is removed from the comparison of response. The simulation overestimates the response at low momentum by about 5%, an effect that can be mostly attributed to the underestimation of the zero fraction mentioned previously. For $|\eta| < 0.6$, the data-simulation agreement has a larger discrepancy by about 5% for 2010 than 2012, although this is not reproduced in at higher pseudorapidity.

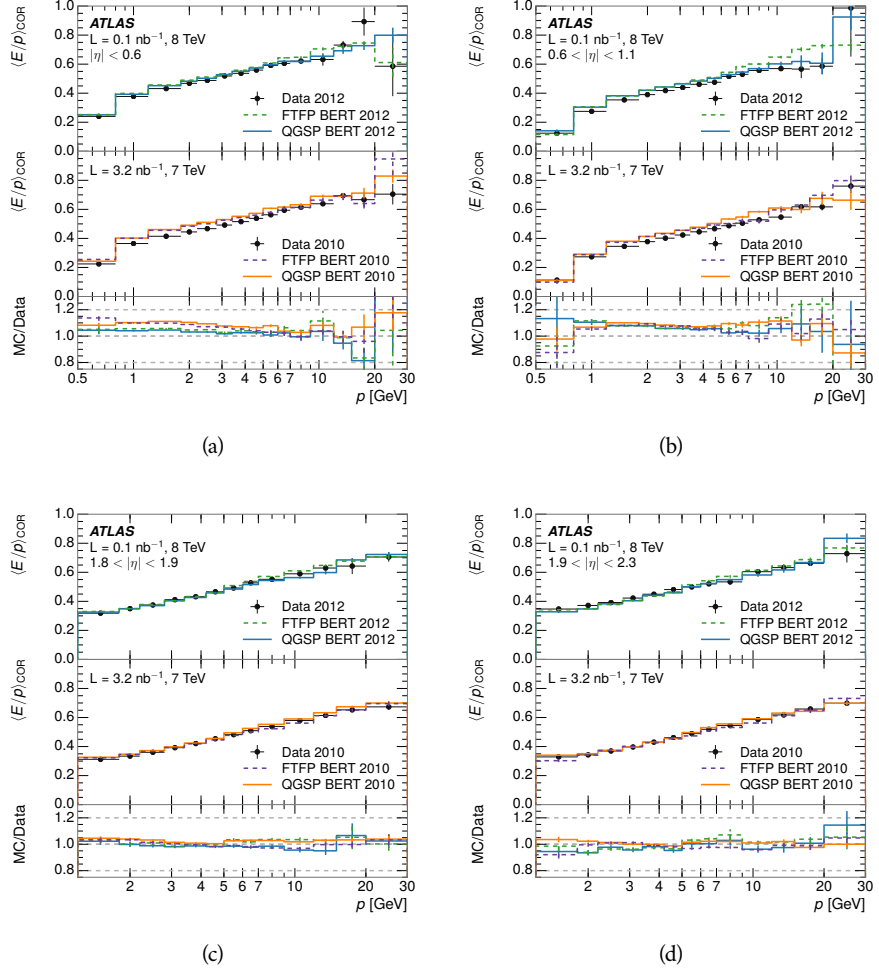


Figure 31: $\langle E/p \rangle_{\text{COR}}$ as a function of track momentum, for tracks with (a) $|\eta| < 0.6$, (b) $0.6 < |\eta| < 1.1$, (c) $1.8 < |\eta| < 1.9$, and (d) $1.9 < |\eta| < 2.3$.

The response measurement above used topological clustering at the EM scale, that is clusters were formed to measure energy but no corrections were applied to correct for expected effects like energy lost outside of the cluster or in uninstrumented material. It is also interesting to measure $\langle E/p \rangle_{\text{COR}}$ using local cluster weighted (**LCW**) energies, which accounts for those effects by calibrating the energy based on the properties of the cluster such as energy density and depth in the calorimeter. Figure 32 shows these distributions for tracks with zero or more clusters and separately for tracks with one or more clusters. The calibration moves the mean value of $\langle E/p \rangle_{\text{COR}}$ significantly closer to 1.0 as desired. The agreement between data and simulation improves noticeably when at least one cluster is required, as this removes the contribution from the mismodeling of

1047 the zero fraction. The good agreement in that case again demonstrates that the
 1048 difference in $\langle E/p \rangle_{\text{COR}}$ between data and simulation is caused predominantly
 1049 by the difference in zero fraction.

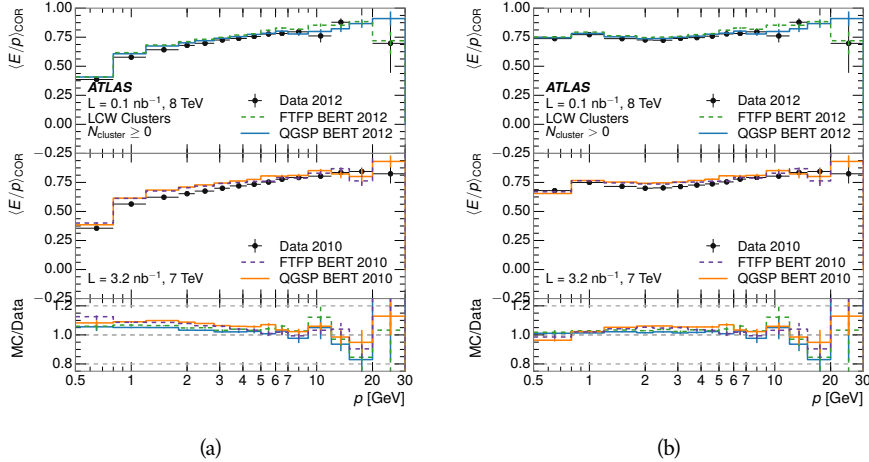


Figure 32: $\langle E/p \rangle_{\text{COR}}$ calculated using LCW-calibrated topological clusters as a function of track momentum for tracks with (a) zero or more associated topological clusters or (b) one or more associated topological clusters.

1050 8.2.5 ADDITIONAL STUDIES

1051 As has been seen in several measurements in previous sections, the simulation
 1052 does not correctly model the chance of a low momentum hadron to reach the
 1053 calorimeter. Because of the consistent discrepancy across pseudorapidity and
 1054 interaction lengths, this can be best explained by incomplete understanding of
 1055 hadronic interactions with the detector [10]. For example, a hadron that scat-
 1056 ters off of a nucleus in the inner detector can be deflected through a significant
 1057 angle and not reach the expected location in the calorimeter. In addition, these
 1058 interactions can produce secondary particles that are difficult to model.

1059 The requirement used throughout the previous sections on the number of
 1060 hits in the TRT reduces these effects by preferentially selecting tracks that do
 1061 not undergo nuclear interactions. It is interesting to check how well the sim-
 1062 ulation models tracks with low numbers of TRT hits, which selects tracks that
 1063 are more likely to have undergone a hadronic interaction. Figure 33 compares
 1064 the distributions with $N_{\text{TRT}} < 20$ to $N_{\text{TRT}} > 20$ for real and simulated particles.
 1065 As expected, the tracks with fewer hits are poorly modeled in the simulation as
 1066 $\langle E/p \rangle_{\text{COR}}$ differs by as much as 25% at low momentum.

1067 Another interesting aspect of the simulation is the description of antiprotons
 1068 at low momentum, where QGSP_BERT and FTFP_BERT have significant differ-
 1069 ences. This can be seen to have an effect in the inclusive response measurement
 1070 when separated into positive and negative charge. The $\langle E/p \rangle_{\text{COR}}$ distributions
 1071 for positive and negative particles are shown in Figure 34, where a small differ-
 1072 ence between QGSP_BERT and FTFP_BERT can be seen in the distribution for

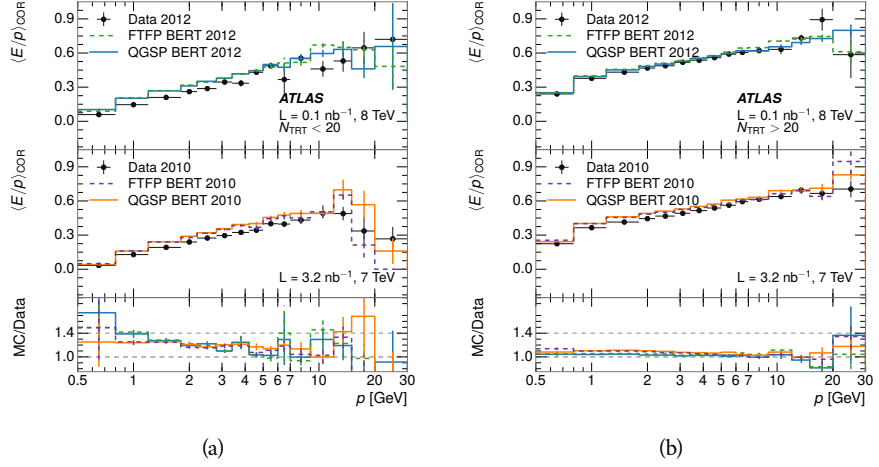


Figure 33: Comparison of the $\langle E/p \rangle_{\text{COR}}$ for tracks with (a) less than and (b) greater than 20 hits in the TRT.

negative tracks. This is demonstrated more clearly in Figure 35, which shows the E/p distribution in the two simulations separated by charge. There is a clear difference around $E/p > 1.0$, which can be explained by the additional energy deposited by the annihilation of the antiproton in the calorimeter that is modeled well only in FTFP_BERT. This is also explored with data using identified antiprotons in Section 8.3.

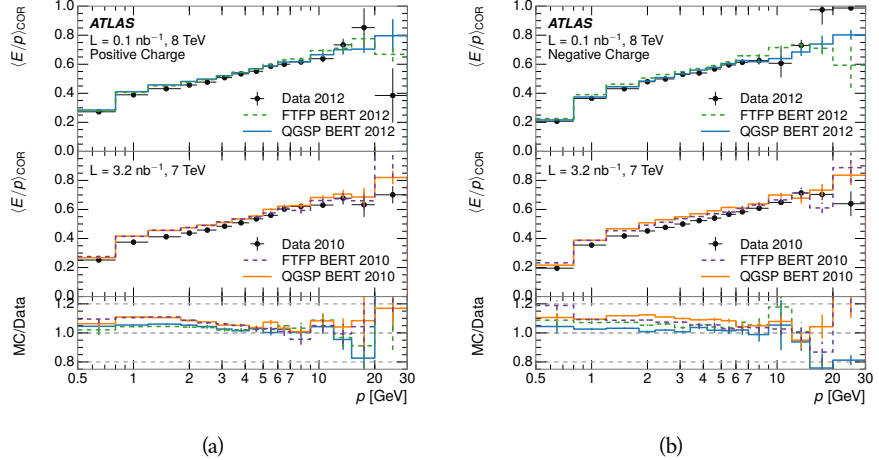


Figure 34: Comparison of the $\langle E/p \rangle_{\text{COR}}$ for (a) positive and (b) negative tracks as a function of track momentum for tracks with $|\eta| < 0.6$.

The $\langle E/p \rangle$ results in previous sections have considered the electromagnetic and hadronic calorimeters together as a single energy measurement, to emphasize the total energy deposited for a given particle. However, the deposits in each calorimeter are available separately and $\langle E/p \rangle$ can be constructed for each layer. As the layers are composed of different materials and are modeled separately in the detector geometry, confirmation that the simulation matches the data well

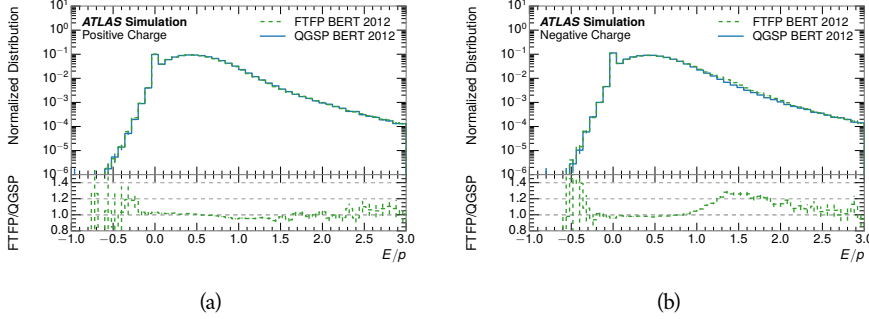


Figure 35: Comparison of the E/p distributions for (a) positive and (b) negative tracks with $0.8 < p/\text{GeV} < 1.2$ and $|\eta| < 0.6$, in simulation with the FTFP_BERT and QGSP_BERT physics lists.

in each layer adds confidence in both the description of hadronic interactions with the two different materials and also the geometric description of each.

The technique discussed in Section 8.2.3 for selecting minimally ionizing particle (MIP)s in the electromagnetic calorimeter is also useful in studying deposits in the hadronic calorimeter. Those MIPs deposit almost all of their energy exclusively in the hadronic calorimeter. Figure 36 shows $\langle E/p \rangle_{\text{RAW}}^{\text{Had}}$, where RAW indicates that no correction has been applied for neutral backgrounds and Had indicates that only clusters for the hadronic calorimeter are included. The RAW and COR versions of $\langle E/p \rangle$ in this case are the same, as the neutral background is negligible in that calorimeter layer. The distributions are shown both for the original EM scale calibration and after LCW calibration. The data and simulation agree very well in this comparison, except in the lowest momentum bin which has 5% discrepancy that has already been seen in similar measurements.

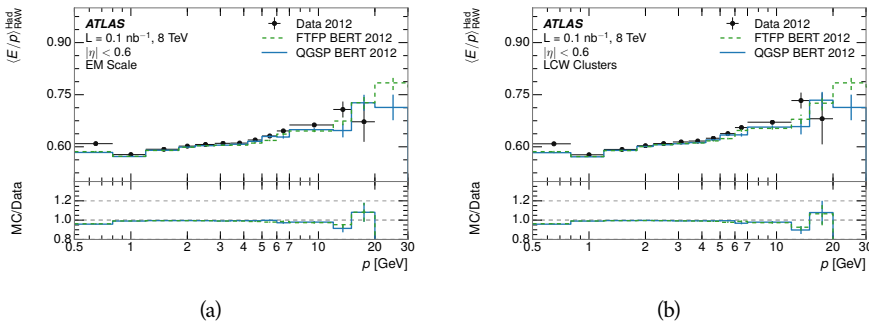


Figure 36: Comparison of the response of the hadronic calorimeter as a function of track momentum (a) at the EM-scale and (b) after the LCW calibration.

A similar comparison can be made in the electromagnetic calorimeter by selecting particles which have no associated energy in the hadronic calorimeter. These results are measured in terms of $\langle E/p \rangle_{\text{COR}}^{\text{EM}}$, where EM designates that only clusters in the electromagnetic calorimeter are included and COR designates that the neutral background is subtracted as the neutral background is present in this case. Figure 37 shows the analogous comparisons to Figure 36 in

1104 the electromagnetic calorimeter. In this case the disagreement between data and
 1105 simulation is more pronounced, with discrepancies as high as 5% over a larger
 1106 range of momenta. This level of discrepancy indicates that the description of
 1107 the electromagnetic calorimeter is actually the dominant source of discrepancy
 1108 in the combined distributions in Section 8.2.4.

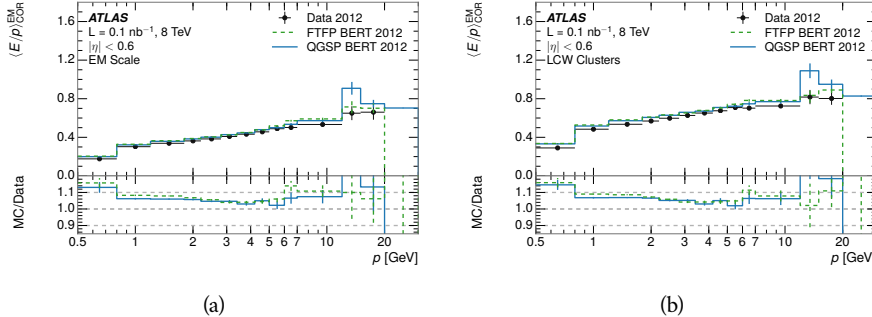


Figure 37: Comparison of the response of the EM calorimeter as a function of track momentum (a) at the EM-scale and (b) with the LCW calibration.

1109 **NOTE: There are more studies that I skipped for brevity that could be in-**
 1110 **cluded if interesting. E/p at different cluster threshold settings, E/p with**
 1111 **pileup, E/p with cells. I also left out a lot of eta bins that appear in the**
 1112 **paper so that this section didn't turn into 20 pages of plots.**

1113 8.3 IDENTIFIED PARTICLE RESPONSE

1114 The inclusive response measurement for hadrons can be augmented by measur-
 1115 ing the response for specific particle species. The simulation models each parti-
 1116 cle type separately, and understanding the properties of each is important in con-
 1117 straining the uncertainty on jets. In order to select and measure specific hadrons,
 1118 this section relies on the displaced decays of long-lived particles. Such decays
 1119 can be identified by reconstructing secondary vertices with a requirement on
 1120 mass. In particular, Λ , $\bar{\Lambda}$, and K_S^0 can be used to select a pure sample of protons,
 1121 antiprotons, and pions, respectively.

1122 8.3.1 DECAY RECONSTRUCTION

1123 The measurement of response for identified particles uses the same selection as
 1124 for inclusive particles (Section 8.1.3) with a few additions. Each event used is
 1125 required to have at least one secondary vertex, and the tracks are required to
 1126 match to that vertex rather than the primary vertex. Pions are selected from
 1127 decays of $K_S^0 \rightarrow \pi^+ \pi^-$, which is the dominant decay for K_S^0 to charged particles.
 1128 Protons are selected from decays of $\Lambda \rightarrow \pi^- p$ and antiprotons from $\bar{\Lambda} \rightarrow \pi^+ \bar{p}$,
 1129 which are similarly the dominant decays of Λ and $\bar{\Lambda}$ to charged particles. The
 1130 species of parent hadron in these decays is determined by reconstructing the
 1131 mass of the tracks associated to the secondary vertex. The sign of the higher

momentum decay particle can distinguish between Λ and $\bar{\Lambda}$, which of course have the same mass, as the proton or antiproton is kinematically favored to have higher momentum. Examples of the reconstructed masses used to select these decays are shown in Figure 38.

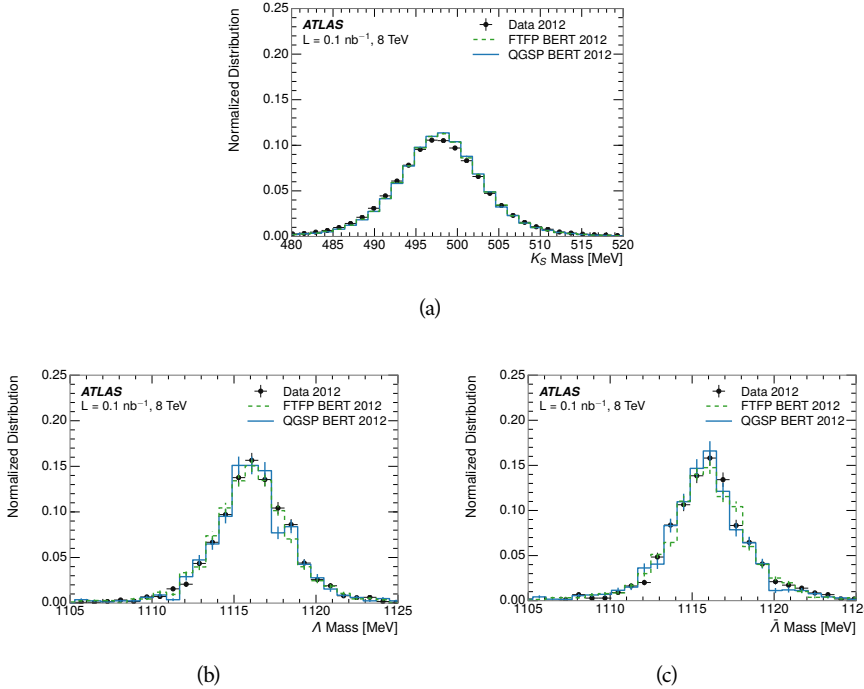


Figure 38: The reconstructed mass peaks of (a) K_S^0 , (b) Λ , and (c) $\bar{\Lambda}$ candidates.

The dominant backgrounds for the identified particle decays are nuclear interactions and combinatoric sources. These are suppressed by the kinematic requirements on the tracks as well as an additional veto which removes candidates that are consistent with both a Λ or $\bar{\Lambda}$ and a K_S^0 hypothesis, which is possible because of the different assumptions on particle mass in each case [11]. After these requirements, the backgrounds are found to be negligible compared to the statistical errors on these measurements.

8.3.2 IDENTIFIED RESPONSE

With these techniques the E/p distributions are extracted in data and simulation for each particle species and shown in Figure 39. These distributions are shown for a particular bin of E_a ($2.2 < E_a/\text{GeV} < 2.8$), rather than p . E_a is the energy available to be deposited in the calorimeter: for pions $E_a = \sqrt{p^2 + m^2}$, for protons $E_a = \sqrt{p^2 + m^2} - m$, and for antiprotons $E_a = \sqrt{p^2 + m^2} + m$. The features of the E/p distributions are similar to the inclusive case. There is a small negative tail from noise and a large fraction of tracks with zero energy from particles which do not reach the calorimeter. The long positive tail is noticeably more pronounced for antiprotons because of the additional energy generated by the annihilation in addition to the neutral background.

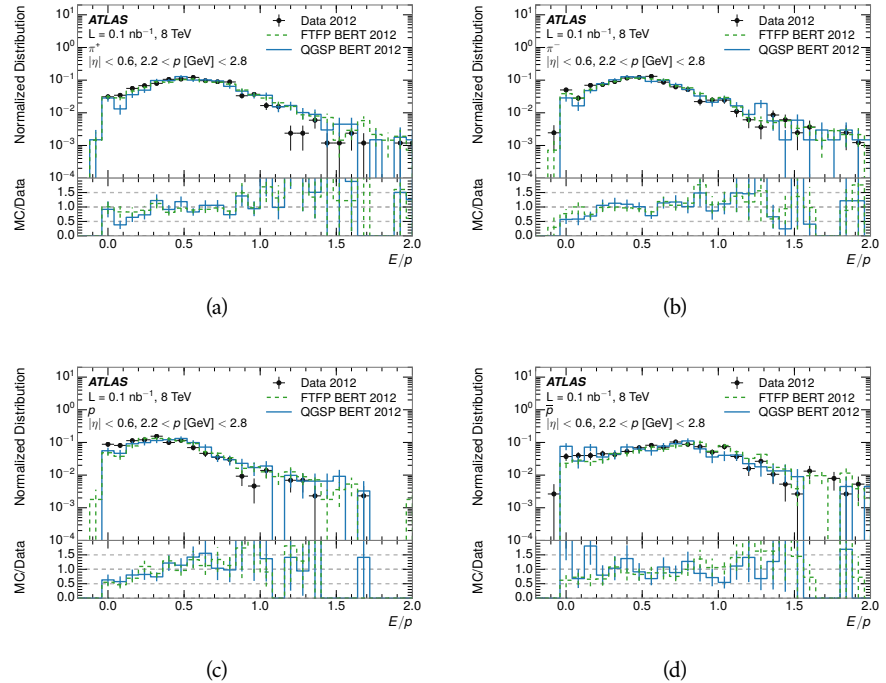


Figure 39: The E/p distribution for isolated (a) π^+ , (b) π^- , (c) proton, and (d) anti-proton tracks.

1154 The zero fraction is further explored in Figure 40 for pions and protons in data
 1155 and simulation. The simulation consistently underestimates the zero fraction
 1156 independent of particle species, which implies that this discrepancy is not caused
 1157 by the model of a particular species but rather a feature common to all.

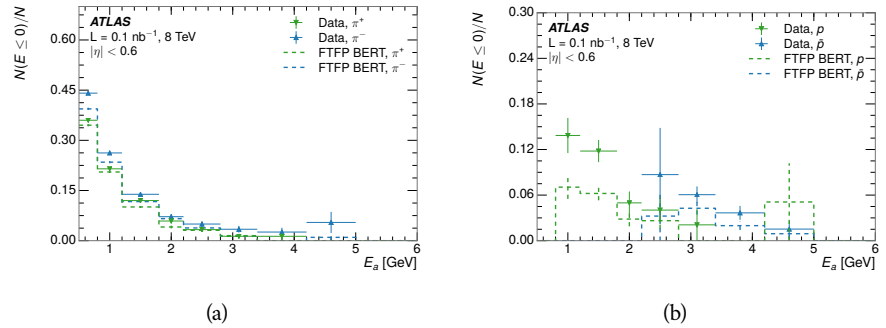


Figure 40: The fraction of tracks with $E \leq 0$ for identified (a) π^+ and π^- , and (b) proton and anti-proton tracks

1158 It is also interesting to compare the response between the different particle
 1159 species. One approach to do this is to measure the difference in $\langle E/p \rangle$ between
 1160 two types, which has the advantage of removing the neutral background. These
 1161 differences are shown in various combinations in Figure 41. The response for
 1162 π^+ is greater on average than the response to π^- because of a charge-exchange
 1163 effect which causes the production of additional neutral pions in the showers of

1164 π^+ [33]. The response for π^+ is also greater on average than the response to p ,
 1165 because a large fraction of the energy of π^+ hadrons is converted to an electro-
 1166 magnetic shower [34, 35]. However, the \bar{p} response is significantly higher than
 1167 the response to π^- because of the annihilation of the antiproton. FTFP_BERT
 1168 does a better job of modeling this effect than QGSP_BERT because of their differ-
 1169 ent descriptions of \bar{p} interactions with material.

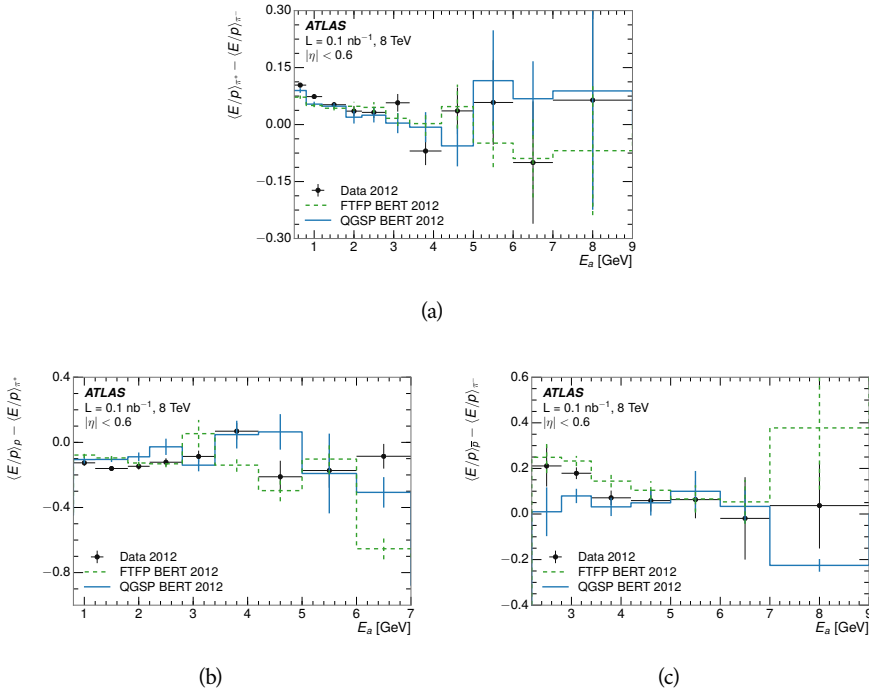


Figure 41: The difference in $\langle E/p \rangle$ between (a) π^+ and π^- (b) p and π^+ , and (c) \bar{p} and π^- .

1170 It is also possible to remove the neutral background from these response dis-
 1171 tributions using the same technique as in Section 8.2.3. The technique is largely
 1172 independent of the particle species and so can be directly applied to $\langle E/p \rangle$ for
 1173 pions. The $\langle E/p \rangle_{\text{COR}}$ distributions for pions are shown in Figure 42, which are
 1174 very similar to the inclusive results. The inclusive hadrons are comprised mostly
 1175 of pions, so this similarity is not surprising. It is also possible to see the small
 1176 differences between π^+ and π^- response here, where $\langle E/p \rangle_{\text{COR}}$ is higher on av-
 1177 erage for π^+ . The agreement between data and simulation is significantly worse
 1178 for the π^- distributions than for the π^+ , with a discrepancy greater than 10%
 1179 below 2-3 GeV.

1180 8.3.3 ADDITIONAL SPECIES IN SIMULATION

1181 The techniques above provide a method to measure the response separately for
 1182 only pions and protons. However the hadrons which forms jets include a num-
 1183 ber of additional species such as kaons and neutrons. The charged kaons are
 1184 an important component of the inclusive charged hadron distribution, which is
 1185 comprised of roughly 60-70% pions, 15-20% kaons, and 5-15% protons. These

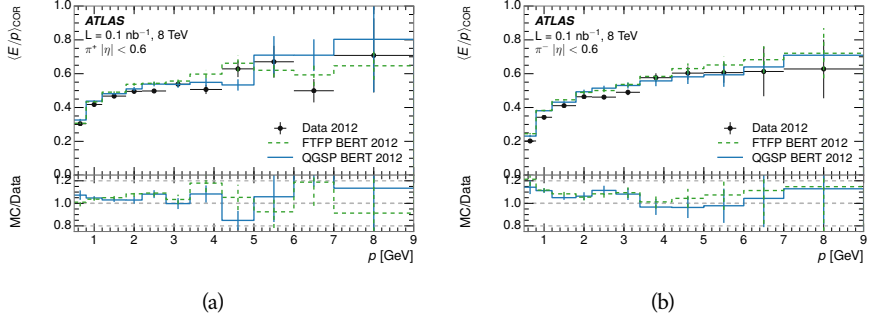


Figure 42: $\langle E/p \rangle_{\text{COR}}$ as a function of track momentum for (a) π^+ tracks and (b) π^- tracks.

are difficult to measure in data at the ATLAS detector, although a template subtraction technique has been proposed which may be effective with larger sample sizes [10]. The simulation of these particles includes noticeable differences in response at low energies, which are shown in Figure 43 for FTFP_BERT. The significant differences in response between low energy protons and antiprotons are accounted for above in the definitions of E_a .

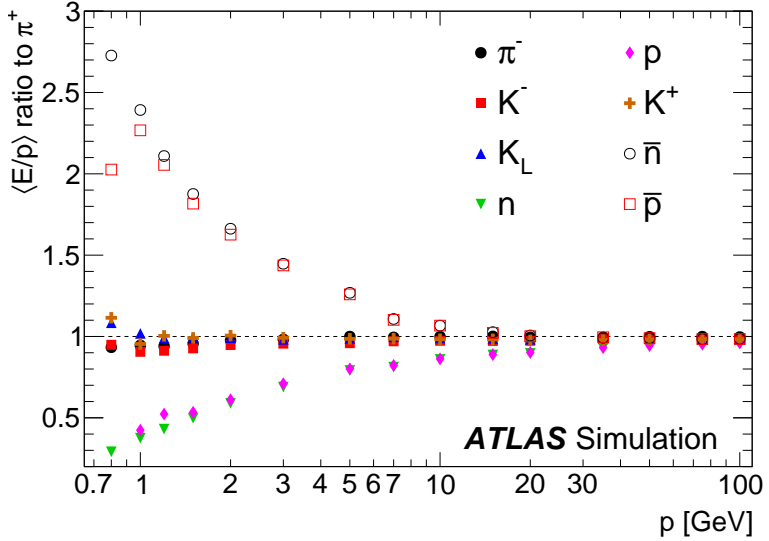


Figure 43: The ratio of the calorimeter response to single particles of various species to the calorimeter response to π^+ with the physics list FTFP_BERT.

8.4 SUMMARY

These various measurements of calorimeter response shown above for data and simulation illuminate the accuracy of the simulation of hadronic interactions at the ATLAS detector. The results were done using 2010 and 2012 data at 7 and 8 TeV, but reflect the most current understanding of the detector alignment and geometry. A number of measurements focusing on a comparison between pro-

1198 tons and antiprotons suggest that FTFP_BERT models those interaction more
1199 accurately than QGSP_BERT. These measurements, among others, were the moti-
1200 vation to switch the default Geant4 simulation from FTFP_BERT to QGSP_BERT
1201 for all ATLAS samples.

1202 Even with these updates, there are a number of small, approximately 5%, dis-
1203 crepancies in response between the data and simulation at low energies. At
1204 higher energies the simulation of hadronic interactions is very consistent with
1205 data. Chapter 9 discusses how to use these observed differences to constrain the
1206 jet energy scale and its associated uncertainties.

1207

1208 JET ENERGY RESPONSE AND UNCERTAINTY

1209 9.1 MOTIVATION

1210 As jets form a major component of many physics analyses at ATLAS, it is crucial
 1211 to carefully calibrate the measurement of jet energies and to derive an uncer-
 1212 tainty on that measurement. These uncertainties have often been the dominant
 1213 systematic uncertainty in high-energy analyses at the LHC. Dijet and multijet
 1214 balance techniques provide a method to constrain the JES and its uncertainty in
 1215 data, and provide the default values used for ATLAS jet measurements at most
 1216 energies [36]. These techniques are limited by their reliance on measuring jets
 1217 in data, so they are statistically limited in estimating the jet energy scale at the
 1218 highest jet energies. This chapter presents another method for estimating the jet
 1219 energy scale and its uncertainty which builds up a jet from its components and
 1220 thus can be naturally extended to high jet momentum. Throughout this chapter
 1221 the jets studied are simulated using Pythia8 with the CT10 parton distribution
 1222 set [37] and the AU2 tune [14], and corrections are taken from the studies includ-
 1223 ing data and simulation in Chapter 8.

1224 As described in Section 7.2, jets are formed from topological clusters of energy
 1225 in the calorimeters using the anti- k_t algorithm. These clusters originate from a
 1226 diverse spectrum of particles, in terms of both species and momentum, leading to
 1227 significantly varied jet properties and response between jets of similar produced
 1228 momentum. Figure 44 shows the simulated distribution of particles within jets
 1229 at a few examples energies. The E/p measurements provide a thorough under-
 1230 standing of the dominant particle content of jets, the charged hadrons.

1231 9.2 UNCERTAINTY ESTIMATE

1232 Simulated jets are not necessarily expected to correctly model the energy de-
 1233 posits in the calorimeters, because of the various discrepancies discussed in Chap-
 1234 ter 8. To evaluate a jet energy response, the simulated jet energies are compared
 1235 to a corrected jet built up at the particle level. Each cluster in a jet is associated
 1236 to the truth particle which deposited it, and the energy in that cluster is then
 1237 corrected for a number of effects based on measurements in data. The primary
 1238 corrections come from the single hadron response measurements in addition to
 1239 response measured using the combined test beam which covers higher momen-
 1240 tum particles [38]. These corrections include both a shift (Δ), in order to make
 1241 the simulation match the average response in data, and an uncertainty (σ) asso-
 1242 ciated with the ability to constrain the difference between data and simulation.
 1243 Some of the dominant sources of uncertainty are itemized in Table 2 with typi-
 1244 cal values, and the full list considered is described in detail in the associated pa-

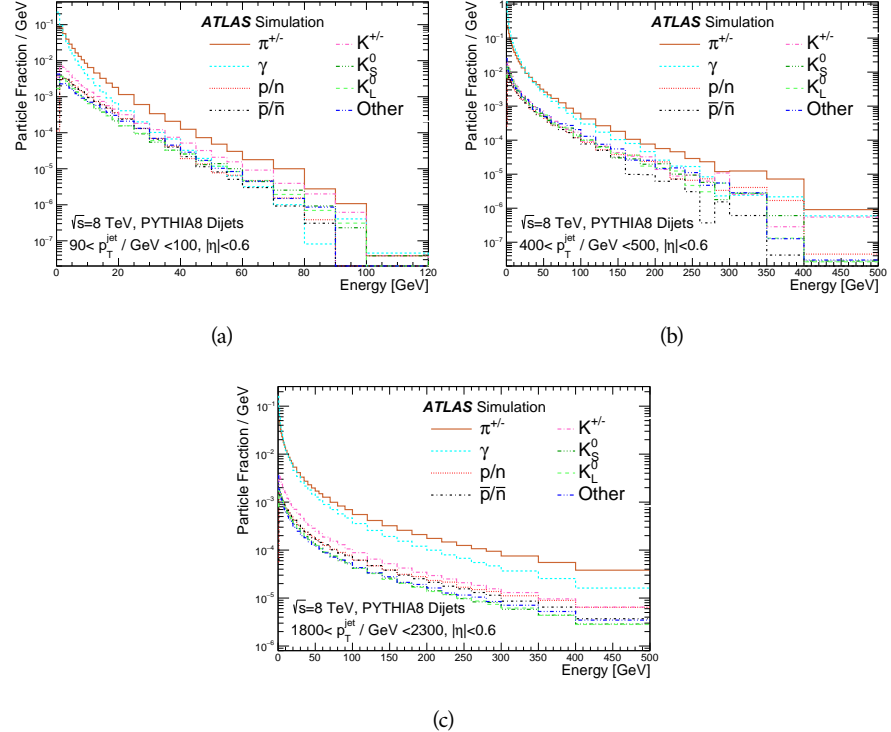


Figure 44: The spectra of true particles inside anti- k_t , $R = 0.4$ jets with (a) $90 < p_T/\text{GeV} < 100$, (b) $400 < p_T/\text{GeV} < 500$, and (c) $1800 < p_T/\text{GeV} < 2300$.

1245 per [10]. These uncertainties cover differences between the data and simulation
 1246 in the modeling of calorimeter response to a given particle. No uncertainties are
 1247 added for the difference between particle composition of jets in data and simu-
 1248 lation.

1249 From these terms, the jet energy scale and uncertainty is built up from indi-
 1250 vidual energy deposits in simulation. Each uncertainty term is treated indepen-
 1251 dently, and are taken to be gaussian distributed. The resulting scale and uncer-
 1252 tainty is shown in Figure 45, where the mean response is measured relative to
 1253 the calibrated energy reported by simulation. The dominant uncertainties come
 1254 from the statistical uncertainties on the E/p measurements at lower energies and
 1255 the additional uncertainty for out of range measurements at higher energies. The
 1256 total uncertainty from this method at intermediate jet energies is comparable to
 1257 other simulation-based methods [39] and is about twice as large as in-situ meth-
 1258 ods using data [36]. This method is the only one which provides an estimation
 1259 above 1.8 TeV, however, and so is still a crucial technique in analyses that search
 1260 for very energetic jets.

1261 These techniques can also be used to measure the correlation between bins of
 1262 average reconstructed jet momentum across a range of p_T and $|\eta|$, where cor-
 1263 relations are expected because of a similarity in particle composition at similar
 1264 energies. Figure 46 shows these correlations, where the uncertainties on jets in
 1265 neighboring bins are typically between 30% and 60% correlated. The uncertainty
 1266 on all jets becomes significantly correlated at high energies and larger pseudora-

Abbrev.	Description	Δ (%)	σ (%)
In situ E/p	The comparison of $\langle E/p \rangle_{\text{COR}}$ as described in Chapter 8 with statistical uncertainties from 500 MeV to 20 GeV.	0-3	1-5
CTB	The main $\langle E/p \rangle$ comparison uncertainties, binned in p and $ \eta $, as derived from the combined test beam results, from 20 to 350 GeV [38].	0-3	1-5
E/p Zero Fraction	The difference in the zero-fraction between data and MC simulation from 500 MeV to 20 GeV.	5-25	1-5
E/p Threshold	The uncertainty in the EM calorimeter response from the potential mismodeling of threshold effects in topological clustering.	0	0-10
Neutral	The uncertainty in the calorimeter response to neutral hadrons based on studies of physics model variations.	0	5-10
K_L	An additional uncertainty in the response to neutral K_L in the calorimeter based on studies of physics model variations.	0	20
E/p Misalignment	The uncertainty in the p measurement from misalignment of the ID.	0	1
Hadrons, $p > 350$ GeV	A flat uncertainty for all particles above the energy range or outside the longitudinal range probed with the combined test beam.	0	10

Table 2: The dominant sources of corrections and systematic uncertainties in the [JES](#) estimation technique, including typical values for the correcting shift (Δ) and the associated uncertainty (σ).

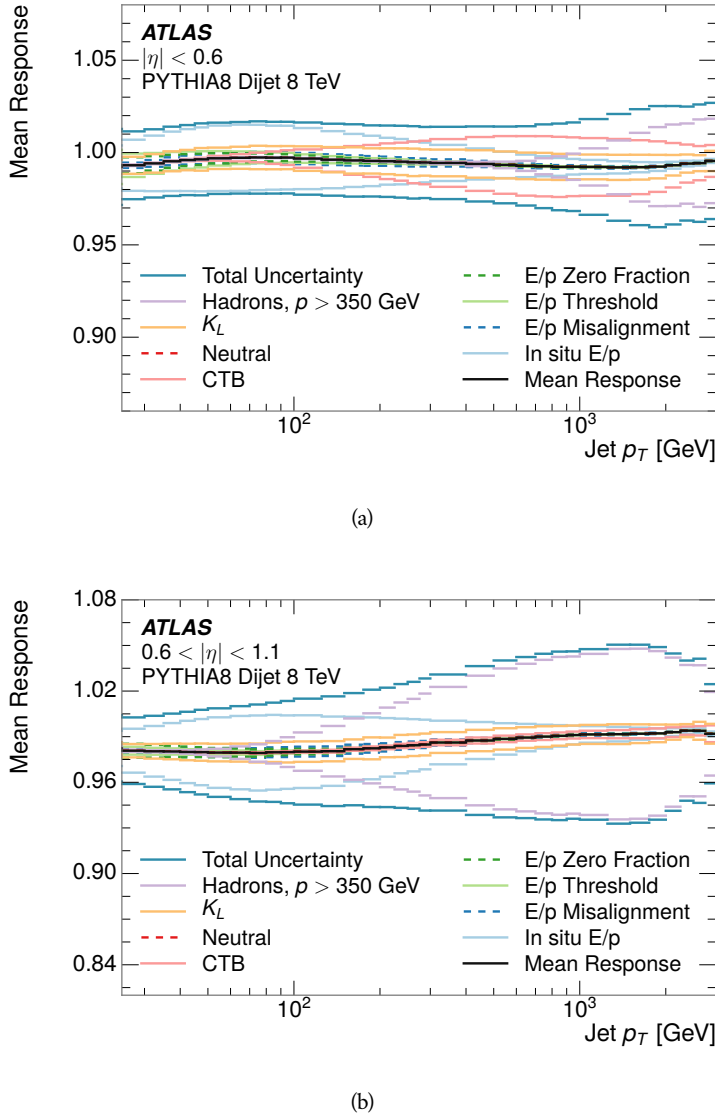


Figure 45: The [JES](#) uncertainty contributions, as well as the total [JES](#) uncertainty, as a function of jet p_T for (a) $|\eta| < 0.6$ and (b) $0.6 < |\eta| < 1.1$.

1267 pidities, when the uncertainty becomes dominated by the single term reflecting
 1268 out of range particles.

1269 9.3 SUMMARY

1270 The technique described above provides a jet energy scale and uncertainty by
 1271 building up jet corrections from the energy deposits of constituent particles. The
 1272 E/p measurements are crucial in providing corrections for the majority of parti-
 1273 cles in the jets. The uncertainty derived this way is between 2 and 5% and is about
 1274 twice as large at corresponding momentum than jet balance methods. However
 1275 this is the only uncertainty available for very energetic jets using 2012 data and
 1276 simulation, and repeating this method with Run 2 data and simulation will be

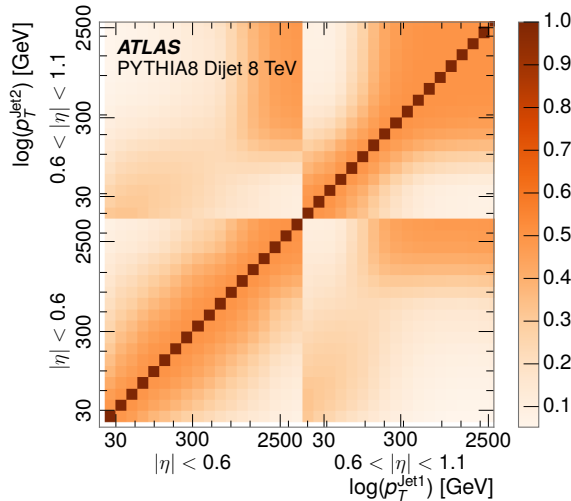


Figure 46: The JES correlations as a function of jet p_T and $|\eta|$ for jets in the central region of the detector.

¹²⁷⁷ important in providing an uncertainty for the most energetic jets in 13 TeV col-
¹²⁷⁸ lisions.

1279

PART V

1280

SEARCH FOR LONG-LIVED PARTICLES

1281

You can put some informational part preamble text here.

1282

1283 LONG-LIVED PARTICLES IN ATLAS

1284 As discussed in Section 2.3, various limitations in the SM suggest a need for new
 1285 particles at the TeV scale. A wide range of extensions to the Standard Model
 1286 predict that these new particles can have lifetimes greater than approximately
 1287 one-hundredth of a nanosecond. These include theories with universal extra-
 1288 dimensions [40, 41], with new fermions [42], and with leptoquarks [43]. Many
 1289 Supersymmetry (SUSY) theories also produce these Long-Lived Particles (LLPs),
 1290 in both R-Parity violating [44–46] and R-Parity conserving [47–50] formula-
 1291 tions. Split supersymmetry [51, 52], for example, predicts long-lived gluinos
 1292 with $O(\text{TeV})$ masses. This search focuses specifically on the SUSY case, but many
 1293 of the results are generic to any model with LLPs.

1294 Long-lived gluinos or squarks carry color-charge and will thus hadronize into
 1295 color neutral bound states called R-Hadrons. These are composit particles like
 1296 the usual hadrons but with one supersymmetric constituent, for example $\tilde{g}q\bar{q}$
 1297 and $\tilde{q}\bar{q}$. Through this hadronization process, the neutral gluino can acquire a
 1298 charge. Gluino pair production, $pp \rightarrow \tilde{g}\tilde{g}$ has the largest cross sectional increase
 1299 with the increase in energy to 13 TeV, and so this search focuses on gluino R-
 1300 Hadrons. Planned future updates will extend the case to explicitly include squark
 1301 and chargino models, but the method covers any long-lived, charged, massive
 1302 particle.

1303 10.1 EVENT TOPOLOGY

1304 The majority of SUSY models predict that gluinos will be produced in pairs at
 1305 the LHC, through processes like $pp \rightarrow q\bar{q} \rightarrow \tilde{g}\tilde{g}$ and $pp \rightarrow gg \rightarrow \tilde{g}\tilde{g}$, where the
 1306 gluon mode dominates for the collision energy and gluino masses considered
 1307 for this search. During their production, the long-lived gluinos hadronize into
 1308 color singlet bound states including $\tilde{g}q\bar{q}$, $\tilde{g}qqq$, and even $\tilde{g}g$ [53]. The probability
 1309 to form the gluon-only bound states is a free parameter usually taken to be 0.1,
 1310 while the meson states are favored among the R-Hadrons [54]. The charged and
 1311 neutral states are approximately equally likely for mesons, so the R-Hadrons will
 1312 be charged roughly 50% of the time.

1313 These channels produce R-Hadrons with large p_T , comparable to their mass,
 1314 so that they typically propagate with $0.2 < \beta < 0.9$ [54]. The fragmentation that
 1315 produces that hadrons is very hard, so the jet structure around the R-Hadron
 1316 is minimal, with less than 5 GeV of summed particle momentum expected in a
 1317 cone of $\Delta R < 0.25$ around the R-Hadron [54]. After hadronization, depending
 1318 on the gluino lifetime, the R-Hadrons then decay into hadrons and a LSP [53].

1319 In summary, the expected event for pair-produced long-lived gluinos is very
 1320 simple: two isolated, high-momentum R-Hadrons that propagate through the
 1321 detector before decaying into jets. The observable features of such events depend

1322 strongly on the interaction of the R-Hadron with the material of the detector and
 1323 also its lifetime. Section 10.1.1 describes the interactions of R-Hadrons which
 1324 reach the various detector elements in ATLAS and Section 10.1.2 provides a sum-
 1325 mary of the observable event descriptions for R-Hadrons of various lifetimes.

1326 10.11 DETECTOR INTERACTIONS

1327 After approximately 0.2 ns, the R-Hadron reaches the pixel detector. If charged,
 1328 it deposits energy into the material through repeated single collisions that result
 1329 in ionization of the silicon substrate [55]. Because of its comparatively low β ,
 1330 the ionization energy can be significantly greater than expected for SM particles
 1331 because the most-probable energy loss grows significantly as β decreases [55].
 1332 This large ionization can be measured through the time over threshold (ToT) read
 1333 out from the pixel detector as described in Section 7.1.1.2. Large ionization in
 1334 the inner detector is one of the major characteristic features of LLPs.

1335 Throughout the next few nanoseconds, the R-Hadron propagates through the
 1336 remainder of the inner detector. A charged R-Hadron will provide hits in each
 1337 of these systems as would any other charged particle, and can be reconstructed
 1338 as a track. The track reconstruction provides a measurement of its trajectory
 1339 and thus its momentum as described in Section 7.1. The large momentum is
 1340 another characteristic feature of massive particles produced at the LHC. **Note: At**
 1341 **this point I am failing to mention that the TRT provides a possible dE/dx**
 1342 **measurement, because no one uses it as far as I know.**

1343 As of roughly 20 ns, the R-Hadron enters the calorimeter where it interacts
 1344 hadronically with the material. Because of its large mass and momentum, the
 1345 R-Hadron does not typically stop in the calorimeter, but rather deposits a small
 1346 fraction of its energy through repeated interactions with nucleons. The proba-
 1347 bility of interaction between the gluino itself and a nucleon is low because the
 1348 cross section drops off with the inverse square of its mass, so the interactions are
 1349 primarily governed by the light constituents [56]. Each of these interactions can
 1350 potentially change that quark content and thus change the sign of the R-Hadron,
 1351 so that the charge at exit is typically uncorrelated with the charge at entry [54].
 1352 The total energy deposited in the calorimeters during the propagation is small
 1353 compared to the kinetic energy of the R-Hadron, around 20-40 GeV, so that
 1354 E/p is typically less than 0.1 [54].

1355 Then, 30 ns after the collision, it reaches the muon system, where it again
 1356 ionizes in the material if charged and can be reconstructed as a muon track. Be-
 1357 cause of the charge-flipping interactions in the calorimeter, this track may have
 1358 the opposite sign of the track reconstructed in the inner detector, or there may
 1359 be a track present when there was none in the inner detector and vice-versa. The
 1360 propagation time at the typically lower β results in a significant delay compared
 1361 to muons, and that delay can be assessed in terms of a time-of-flight measure-
 1362 ment. Because of the probability of charge-flip and late arrival, there is a signif-
 1363 icant chance that an R-Hadron which was produced with a charge will not be
 1364 identified as a muon. The long time-of-flight is another characteristic feature of
 1365 R-Hadrons which are reconstructed as muons.

1366 10.1.2 LIFETIME DEPENDENCE

1367 The above description assumed a lifetime long enough for the R-Hadron to exit
 1368 the detector, which through this search is referred to as “stable”, even though
 1369 the particle may decay after exiting the detector. There are several unique sig-
 1370 natures at shorter lifetimes where the R-Hadron decays in various parts of the
 1371 inner detector; these lifetimes are referred to as “metastable”.

1372 The shortest case where the R-Hadron is considered metastable is for life-
 1373 times around 0.01 ns, where the particle decays before reaching any of the de-
 1374 tector elements. Although the R-Hadrons are produced opposite each other in
 1375 the transverse plane, each R-Hadron decays to a jet and an [LSP](#). The [LSPs](#) are not
 1376 measured, so the produced jets can be significantly imbalanced in the transverse
 1377 plane which results in large missing energy. That missing energy can be used
 1378 to trigger candidate events, and provides the most efficient trigger option for
 1379 shorter lifetimes. Additionally, the precision of the tracking system allows the
 1380 displaced vertex of the R-Hadron decay to be reconstructed from the charged
 1381 particles in the jet. The distance of that vertex from the interaction point can
 1382 be used to distinguish R-Hadron decays from other processes. Figure 47 shows
 1383 a schematic diagram of an example R-Hadron event with such a lifetime. The
 1384 diagram is not to scale, but instead illustrates the detector interactions in the
 1385 pixel detector, calorimeters, and muon system. It includes a representation of
 1386 the charged R-Hadron and the neutral R-Hadron, as well as the [LSPs](#) and jets
 1387 (shown as charged hadrons) produced in the decay. Neutral hadrons may also
 1388 be produced in the decay but are not depicted. Previous searches on [ATLAS](#) have
 1389 used the displaced vertex to target [LLP](#) decays [57].

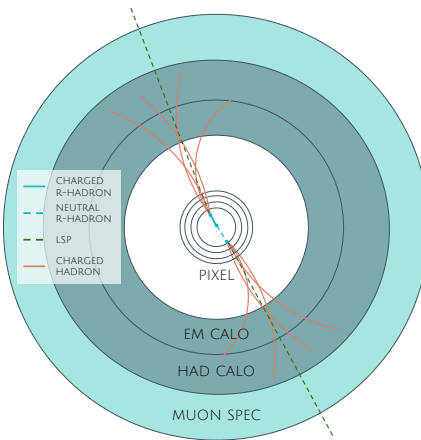


Figure 47: A schematic diagram of an R-Hadron event with a lifetime around 0.01 ns. The diagram includes one charged R-Hadron (solid blue), one neutral R-Hadron (dashed blue), [LSPs](#) (dashed green) and charged hadrons (solid orange). The pixel detector, calorimeters, and muon system are illustrated but not to scale.

1390 The next distinguishable case occurs at lifetimes greater than 0.1 ns, where
 1391 the R-Hadron forms a partial track in the inner detector. If the decay products
 1392 are sufficiently soft, they may not be reconstructed, and this forms a unique sig-

1393 nature of a disappearing track. An example of such an event is illustrated in
 1394 Figure 48, which shows the short track in the inner detector and the undetected
 1395 soft charged hadron and LSP that are produced. A dedicated search on ATLAS used
 1396 the disappearing track signature to search for LLP in Run 1 [58]. **zNote: might**
 1397 **not be worth mentioning the disappearing track here since it is actually a**
 1398 **chargino search, the soft pion is pretty unique to charginos.**

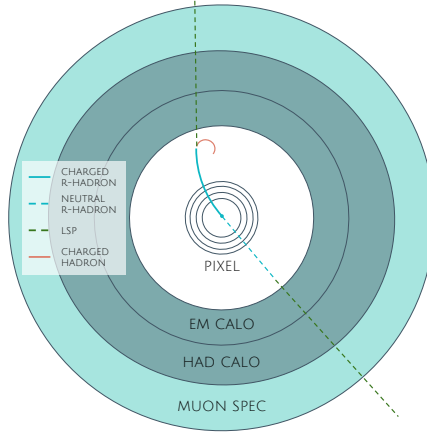


Figure 48: A schematic diagram of an R-Hadron event with a lifetime around 4 ns. The diagram includes one charged R-Hadron (solid blue), one neutral R-Hadron (dashed blue), LSPs (dashed green) and a charged hadron (solid orange). The pixel detector, calorimeters, and muon system are illustrated but not to scale.

1399 If the decay products are not soft, the R-Hadron daughters form jets, resulting
 1400 in an event-level signature of up to two high-momentum tracks, jets, and signif-
 1401 icant missing energy. The missing energy has the same origin as in the case of
 1402 0.01 ns lifetimes, from the decay to unmeasured particles, and again can be large.
 1403 The high-momentum tracks will also have the characteristically high-ionization
 1404 of massive, long-lived particles in the inner detector. Figure 49 illustrates an ex-
 1405 ample event with one charged R-Hadron which decays after approximately 10 ns,
 1406 and shows how the jets from the decay can still be reconstructed in the calorime-
 1407 ter. Several previous searches on ATLAS from Run 1 have used this signature to
 1408 search for R-Hadrons [59, 60], including a dedicated search for metastable parti-
 1409 cles [61].

1410 If the lifetime is longer than several nanoseconds, in the range of 15-30 ns,
 1411 the R-Hadron decay can occur in or after the calorimeters, but prior to reaching
 1412 the muon system. This case is similar to the above, although the jets may not be
 1413 reconstructed, and is covered by many of the same search strategies. The events
 1414 still often have large missing energy, although it is generated through different
 1415 mechanisms. The R-Hadrons do not deposit much energy in the calorimeters, so
 1416 a neutral R-Hadron will not enter into the missing energy calculation. A charged
 1417 R-Hadron opposite a neutral R-Hadron will thus generate significant missing en-
 1418 ergy, and close to 50% of pair-produced R-Hadron events fall into this category.
 1419 If both R-Hadrons are neutral then the missing energy will be low because nei-
 1420 ther is detected. Two charged R-Hadrons will also result in low missing energy
 1421 because both are reconstructed as tracks and will balance each other in the trans-

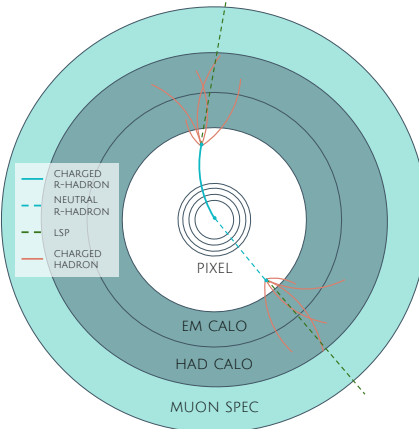


Figure 49: A schematic diagram of an R-Hadron event with a lifetime around 5 ns. The diagram includes one charged R-Hadron (solid blue), one neutral R-Hadron (dashed blue), LSPs (dashed green) and charged hadrons (solid orange). The pixel detector, calorimeters, and muon system are illustrated but not to scale.

1422 verse plane. A small fraction of the time, one of the charged R-Hadron tracks may
 1423 fail quality requirements and thus be excluded from the missing energy calcula-
 1424 tion and again result in significant missing energy. Figure 50 illustrates another
 1425 example event with one charged R-Hadron which decays after approximately 20
 1426 ns, and shows how the jets from the decay might not be reconstructed.

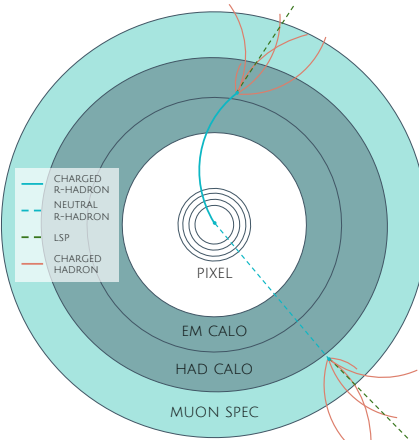


Figure 50: A schematic diagram of an R-Hadron event with a lifetime around 20 ns. The diagram includes one charged R-Hadron (solid blue), one neutral R-Hadron (dashed blue), LSPs (dashed green) and charged hadrons (solid orange). The pixel detector, calorimeters, and muon system are illustrated but not to scale.

1427 The longest lifetimes, the stable case, has all of the features of the 30-50 ns case
 1428 but with the addition of muon tracks for any R-Hadrons that exit the calorimeter
 1429 with a charge. That muon track can provide additional information from time-
 1430 of-flight measurements to help identify LSPs. An example of the event topology
 1431 for one charged and one neutral stable R-Hadron is shown in Figure 51. Some
 1432 searches on ATLAS have included this information to improve the search reach
 1433 for stable particles [60, 62].

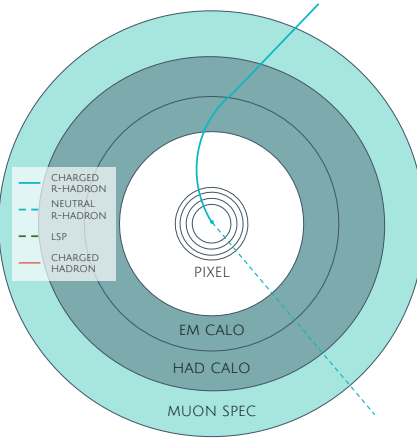


Figure 51: A schematic diagram of an R-Hadron event with a lifetime around 20 ns. The diagram includes one charged R-Hadron (solid blue) and one neutral R-Hadron (dashed blue). The pixel detector, calorimeters, and muon system are illustrated but not to scale.

1434 10.2 SIMULATION

1435 All of the event topologies discussed above are explored by simulations of R-
 1436 Hadron events in the [ATLAS](#) detector. A large number of such samples are gen-
 1437 erated to determine signal efficiencies, to measure expected yields, and to esti-
 1438 mate uncertainties. The primary interaction, pair production of gluinos with
 1439 masses between 400 and 3000 GeV, is simulated using [Pythia 6.4.27](#) [63]
 1440 with the AUET2B [64] set of tuned parameters for the underlying event and
 1441 the CTEQ6L1 [37] parton distribution function ([PDF](#)) set. The simulated inter-
 1442 actions include a modeling of pileup by adding secondary, minimum bias in-
 1443 teractions from both the same (in-time pileup) and nearby (out-of-time pileup)
 1444 bunch crossings. This event generation is then augmented with a dedicated
 1445 hadronization routine to hadronize the long-lived gluinos into final states with
 1446 R-Hadrons [65], with the probability to form a gluon-gluino bound set at 10% [66].

1447 The cross sections used for these processes are calculated at next-to-leading
 1448 order ([NLO](#)) in the strong coupling constant with a resummation of soft-gluon
 1449 emmission at next-to-leading logarithmic ([NLL](#)) [67–71]. The nominal predic-
 1450 tions and the uncertainties for each mass point are taken from an envelope of
 1451 cross-section predictions using different [PDF](#) sets and factorization and renor-
 1452 malization scales [72].

1453 The R-Hadrons then undergo a full detector simulation [], where the interac-
 1454 tions of the R-Hadrons with the material of the detector are described by dedi-
 1455 cated [Geant4](#) [7] routines. These routines model the interactions described in
 1456 Section 10.1.1, including the ionizing interactions in the silicon modules of the
 1457 inner detector and the R-Hadron-nucleon interactions in the calorimeters [73,
 1458 74]. The specific routine chosen to describe the interactions of the R-Hadrons
 1459 with nucleons, the “generic model”, uses a pragmatic approach where the scatter-
 1460 ing cross section is taken to be a constant 12 mb per light quark. In this model

1461 the gluino itself does not interact at all except through its role as a reservoir of
1462 kinetic energy.

1463 The lifetimes of these R-Hadrons are then simulated at several working points,
1464 $\tau = 0.1, 1.0, 3.0, 10, 30, 50$ and detector stable, where the particle is required to
1465 decay after propagating for a time compatible with its lifetime. Only one decay
1466 mode is simulated for these samples, $\tilde{g} \rightarrow q\bar{q}\tilde{\chi}_1^0$ with the neutralino mass set to
1467 100 GeV, which is chosen because it has the highest sensitivity among all of the
1468 modes studied in previous searches [61]. Heavier neutralinos have similar results
1469 but generate less missing energy which reduces the efficiency of triggering.

1470 All of the simulated events are then reconstructed using the same software
1471 used for collision data. The fully reconstructed events are then reweighted to
1472 match the distribution of initial state radiation in an alternative sample of events,
1473 generated with MG5_aMC@NLO [75], which has a more accurate description of ra-
1474 diate effects than Pythia6. This reweighting provides a more accurate descrip-
1475 tion of the momentum of the gluino-gluino system and is important in modeling
1476 the efficiency of triggering and offline event selection.

1477

1478 EVENT SELECTION

1479 The [LLPs](#) targeted by this search differ in their interactions with the detector from
 1480 [SM](#) particles primarily because of their large mass. When produced at the ener-
 1481 gies available at the [LHC](#), that large mass results in a low β (typically $0.2 < \beta <$
 1482 0.9). Such slow-moving particles heavily ionize in detector material. Each layer
 1483 of the pixel detector provides a measurement of that ionization, through [ToT](#), as
 1484 discussed in Section 6.3.1. The ionization in the pixel detector, quantified in
 1485 terms of dE/dx , provides the major focus for this search technique, along with
 1486 the momentum measured in the entire inner detector. It is effective both for its
 1487 discriminating power and its use in reconstructing a particle's mass, and it can
 1488 be used for a wide range of masses and lifetimes as discussed in Section 10.1.2.
 1489 However dE/dx needs to be augmented with a few additional selection require-
 1490 ments to provide a mechanism for triggering and to further reduce backgrounds.

1491 Ionization itself is not currently accessible for triggering, so this search in-
 1492 stead relies on E_T^{miss} to trigger signal events. Although triggering on E_T^{miss} can
 1493 be inefficient, E_T^{miss} is often large for many production mechanisms of [LLPs](#), as
 1494 discussed in Section 10.1.

1495 The use of ionization to reject [SM](#) backgrounds relies on well-measured, high-
 1496 momentum tracks, so some basic requirements on quality and kinematics are
 1497 placed on the tracks considered in this search. These quality requirements have
 1498 been significantly enhanced in Run 2 by a newly introduced tracking variable
 1499 that is very effective in removing highly-ionizing backgrounds caused by over-
 1500 lapping tracks. A few additional requirements are placed on the tracks consid-
 1501 ered for [LLP](#) candidates that increase background rejection by targeting specific
 1502 types of [SM](#) particles. These techniques provide a significant analysis improve-
 1503 ment over previous iterations of ionization-based searches on ATLAS by provid-
 1504 ing additional background rejection with minimal loss in signal efficiency.

1505 The ionization measurement with the Pixel detector can be calibrated to pro-
 1506 vide an estimator of $\beta\gamma$. That estimate, together with the momentum measure-
 1507 ment provided by tracking, can be used to reconstruct a mass for each track
 1508 which traverses the pixel detector. That mass variable will be peaked at the [LLP](#)
 1509 mass for any signal, and provides an additional tool to search for an excess. In
 1510 addition to an explicit requirement on ionization, this search constructs a mass-
 1511 window for each targeted signal mass in order to evaluate any excess of events
 1512 and to set limits.

1513 The strategy discussed here is optimized for lifetimes of $O(1) - O(10)$ ns.
 1514 Pixel ionization is especially useful in this regime as particles only need to prop-
 1515 agate through the first seven layers of the inner detector, about 37 cm from the
 1516 beam axis. The search is still competitive with other searches for [LLPs](#) at longer
 1517 lifetimes, because the primary discriminating variables are still applicable even
 1518 for particles that do not decay within the detector [62]. Although the majority of

1519 the requirements will be the same for all lifetimes, two signal regions are defined
 1520 to optimize separately for intermediate and long lifetime particles.

1521 11.1 TRIGGER

1522 Triggering remains a significant difficulty in defining an event selection with
 1523 high signal efficiency in a search for LLPs. There are no triggers available in
 1524 the current ATLAS system that can fire directly from a high momentum track
 1525 with large ionization (Section 6.6). Although in some configurations a charged
 1526 LLP can fire muon triggers, this requirement introduces significant model depen-
 1527 dence on both the allowed lifetimes and the interactions in the calorimeter [54],
 1528 as discussed in Section 10.1.1.

1529 For a search targeting particles which may decay prior to reaching the muon
 1530 system, the most efficient available trigger is based on missing energy [54]. As
 1531 discussed in Section 10.1, signal events can produce significant E_T^{miss} by a few
 1532 mechanisms. At the trigger level however, the missing energy is only calculated
 1533 using the calorimeters (Section 6.6) where the R-Hadrons deposit little energy.
 1534 So, at short lifetimes, E_T^{miss} measured in the calorimeter is generated by an im-
 1535 balance between the jets and undetected LSPs produced in R-Hadron decays. At
 1536 longer lifetimes, without the decay products, missing energy is only produced in
 1537 the calorimeters when the R-Hadrons recoil against an initial state radiation (ISR)
 1538 jet.

1539 These features are highlighted in Figure 52, which shows the E_T^{miss} distribu-
 1540 tions for simulated short lifetime (3 ns) and stable R-Hadron events. The figure
 1541 includes both the offline E_T^{miss} , the missing energy calculated with all available
 1542 information, and Calorimeter E_T^{miss} , the missing energy calculated using only
 1543 information available at the calorimeter which approximates the missing energy
 1544 available at the trigger. The short lifetime sample has significantly greater E_T^{miss}
 1545 and Calorimeter E_T^{miss} than the stable sample as expected. For the stable sam-
 1546 ple, a small fraction of events with very large E_T^{miss} (about 5%) migrate into the
 1547 bin with very small Calorimeter E_T^{miss} because the E_T^{miss} produced by a charged
 1548 R-Hadron track opposite a neutral R-Hadron track does not contribute any miss-
 1549 ing energy in the calorimeters.

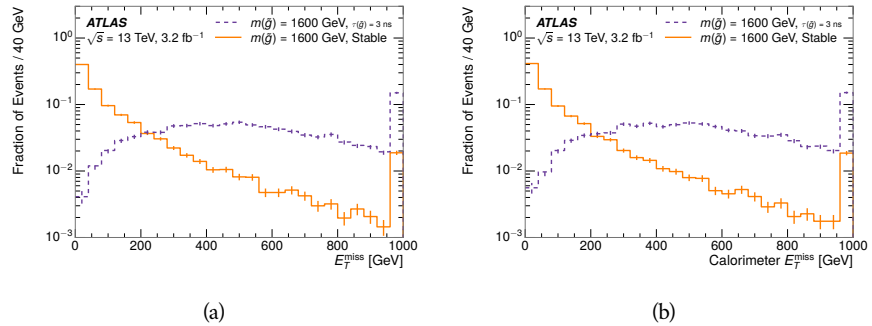


Figure 52: The distribution of (a) E_T^{miss} and (b) Calorimeter E_T^{miss} for simulated signal events before the trigger requirement.

1550 So, either case to some extent relies on kinematic degrees of freedom to pro-
 1551 duce missing energy, as the pair-produced LLPs tend to balance each other in
 1552 the transverse plain. That balance results in a relatively low efficiency for long-
 1553 lifetime particles, roughly 40%, and efficiencies between 65% and 95% for shorter
 1554 lifetimes depending on both the mass and the lifetime. For long lifetimes in par-
 1555 ticular, the presence of ISR is important in providing an imbalance in the trans-
 1556 verse plane, and is an important aspect of modeling the selection efficiency for
 1557 R-Hadron events.

1558 The missing energy trigger with the lowest threshold available is chosen for
 1559 this selection in order to maximize the trigger efficiency. During 2015 data col-
 1560 lection this was the HLT_xe70 trigger, which used a 50 GeV threshold on miss-
 1561 ing energy at LVL1 and a 70 GeV threshold on missing energy at the HLT. These
 1562 formation of the trigger decision for missing energy was discussed in more detail
 1563 in Section 6.6.

1564 11.2 KINEMATICS AND ISOLATION

1565 After the trigger requirement, each event is required to have a primary vertex
 1566 reconstructed from at least two well-measured tracks in the inner detector, each
 1567 with $p_T > 400$ MeV. If more than one such vertex exists, the primary vertex
 1568 is taken to be the one with the largest summed track momentum for all tracks
 1569 associated to that vertex. The offline reconstructed E_T^{miss} is required to be above
 1570 130 GeV to additionally reject SM backgrounds. The transverse missing energy
 1571 is calculated using fully reconstructed and calibrated offline objects, as described
 1572 in Section 7.5. In particular the E_T^{miss} definition in this selection uses jets recon-
 1573 structed with the anti- k_t algorithm with radius $R = 0.4$ from clusters of energy
 1574 in the calorimeter (Section 7.2) and with $p_T > 20$ GeV, as well as reconstructed
 1575 muons, electrons, and tracks not identified as another object type.

1576 The E_T^{miss} distributions are shown for data and a few simulated signals in Fig-
 1577 ure 53, after the trigger requirement. The cut placed at 130 GeV is 95% effi-
 1578 cient for metastable and 90% efficient for stable particles, after the trigger re-
 1579 quirement, because of the missing energy generating mechanisms discussed pre-
 1580 viously. The distribution of data in this figure and subsequent figures in this sec-
 1581 tion can be interpreted as the distribution of backgrounds, as any signal contam-
 1582 ination would be negligible if present at these early stages of the selection (prior
 1583 to the final requirement on ionization). The background falls rapidly with miss-
 1584 ing energy, motivating the direct requirement on E_T^{miss} for the signal region. Al-
 1585 though a tighter requirement than the specified value of 130 GeV would seem to
 1586 increase the search potential from these early distributions, other requirements
 1587 are more optimal when taken as a whole. The specific values for each require-
 1588 ment in signal region were optimized considering the increase in discovery reach
 1589 for tightening the requirement on each discriminating variable. **NOTE: If space**
 1590 **and time permit, I will add a whole section about signal region optimiza-**
 1591 **tion..**

1592 It is typically the practice for searches for new physics on ATLAS to place an
 1593 offline requirement on the triggering variable that is sufficiently tight to guar-

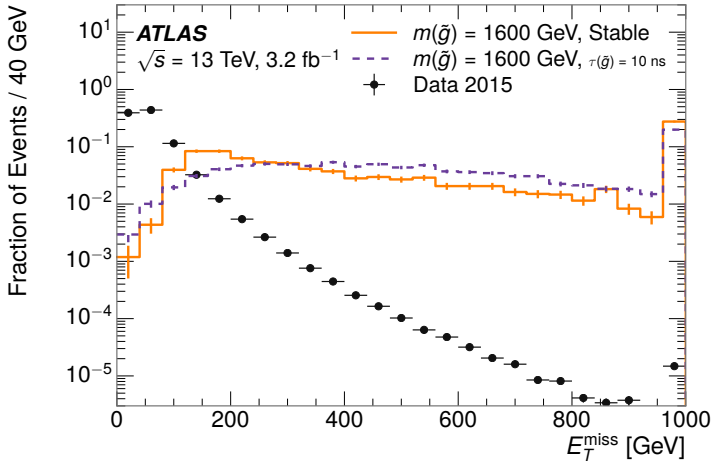


Figure 53: The distribution of E_T^{miss} for data and simulated signal events, after the trigger requirement.

1594 antee that the event would pass the trigger. Such a tight requirement makes the
 1595 uncertainty on the trigger efficiency of the simulation negligible, as modeling the
 1596 regime where the trigger is only partially efficient can be difficult. In this analy-
 1597 sis, however, because of the atypical interactions of R-Hadrons with the tracker
 1598 and the calorimeter, the offline requirement on E_T^{miss} is not sufficient to guar-
 1599 antee a 100% trigger efficiency even at large values, as can be seen in Figure 54.
 1600 This figure shows the efficiency for passing the HLT_xe70 trigger as a function
 1601 of the requirement on E_T^{miss} , which plateaus to roughly 85% even at large values.
 1602 This plateau does not reach 100% because events which have large offline miss-
 1603 ing energy from a neutral R-Hadron produced opposite of a charged R-Hadron
 1604 can have low missing energy in the calorimeters. The Calorimeter E_T^{miss} , on the
 1605 other hand, does not have this effect and reaches 100% efficiency at large values
 1606 because it is the quantity that directly corresponds to the trigger threshold. In
 1607 both cases the efficiency of triggering is greater for the short lifetime sample be-
 1608 cause the late decays to hadrons and LSPs produce an imbalance in the calorime-
 1609 ters even though they may not be reconstructed offline as tracks or jets. For this
 1610 reason, the requirement on E_T^{miss} is determined by optimizing the background
 1611 rejection even though it corresponds to a value of trigger efficiency significantly
 1612 below 1.0.

1613 Potential signal events are then required to have at least one candidate LLP
 1614 track. Although the LLPs are produced in pairs, many models do not consistently
 1615 yield two charged particles. For example, in the R-Hadron model highlighted
 1616 here, only 20% of events have two charged R-Hadrons while 47% of events have
 1617 just one. A signal region requiring two charged candidates could be a powerful
 1618 improvement in background rejection for a larger dataset, but it is not consid-
 1619 ered in this version of the analysis as it was found to be unnecessary to reject the
 1620 majority of backgrounds.

1621 For a track to be selected as a candidate, it must have $p_T > 50 \text{ GeV}$ and pass
 1622 basic quality requirements. The track must be associated to the primary vertex.

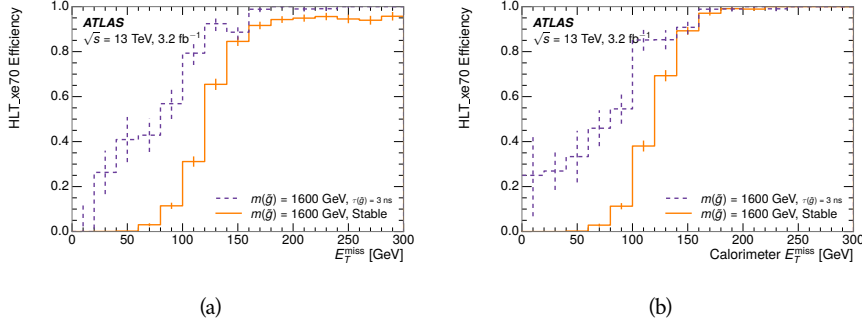


Figure 54: The trigger efficiency for the HLT_xe70 trigger requirement as a function of (a) E_T^{miss} and (b) Calorimeter E_T^{miss} for simulated signal events.

It must also have at least seven clusters in the silicon layers in the inner detector to ensure an accurate measurement of momentum. Those clusters must include one in the innermost layer if the extrapolated track is expected to pass through that layer. And to ensure a reliable measurement of ionization, the track is required to have at least two clusters in the pixel detector that provide a measurement of dE/dx .

At this point in the selection, there is a significant high-ionization background from multiple tracks that significantly overlap in the inner detector. Previous version of this analysis have rejected these overlaps by an explicit overlap rejection between pairs of fully reconstructed tracks, typically by requiring no additional tracks within a cone around the candidate. This technique, however, fails to remove the background from tracks that overlap so precisely that the tracks cannot be separately resolved, which can be produced in very collimated photon conversions or decays of pions.

A new method, added in Run 2, identifies cluster shapes that are likely formed by multiple particles based on a neural network classification algorithm. The number of clusters that are classified this way in the pixel detector for a given track is called N_{split} . As the shape of clusters requires significantly less spatial separation to identify overlaps than it does to reconstruct two fully resolved tracks, this variable is more effective at rejecting backgrounds from overlaps. Figure 55 shows the dependence of ionization on N_{split} ; as N_{split} increases the most probable value of dE/dx grows significantly up to twice the expected value when $N_{\text{split}} = 4$.

This requirement is very successful in reducing the long positive tail of the dE/dx distributions, as can be seen in Figure 56. Comparing the distribution for “baseline tracks”, tracks with only the above requirements on clusters applied and before the requirement on N_{split} , to the distribution with $N_{\text{split}} = 0$, it is clear that the fraction of tracks with large dE/dx is reduced by several orders of magnitude. The tracks without split hits are very close to the dE/dx distribution of identified muons, which are extremely well isolated on average. Figure 56 also includes the distribution of dE/dx in an example signal simulation to demonstrate how effective dE/dx is as a discriminating variable with this isolation applied. The background falls rapidly for $dE/dx > 1.8 \text{ MeVg}^{-1}\text{cm}^2$

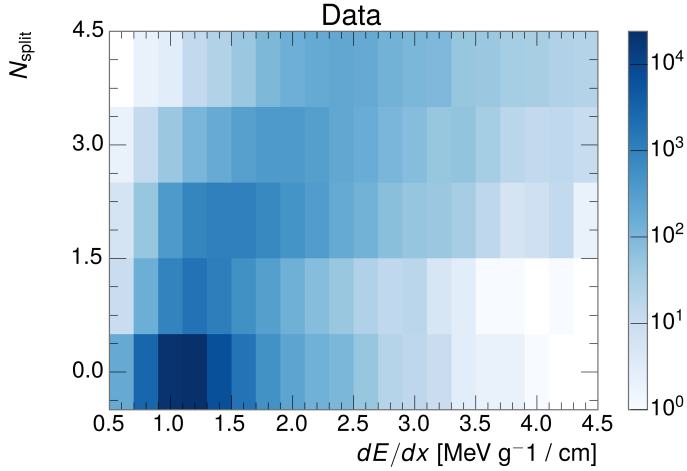


Figure 55: The dependence of dE/dx on N_{split} in data after basic track hit requirements have been applied.

1656 while the majority of the signal, approximately 90% depending on the mass, falls
 1657 above that threshold. Over 90% of LLP tracks in simulated signal events pass the
 1658 N_{split} -based isolation requirement.

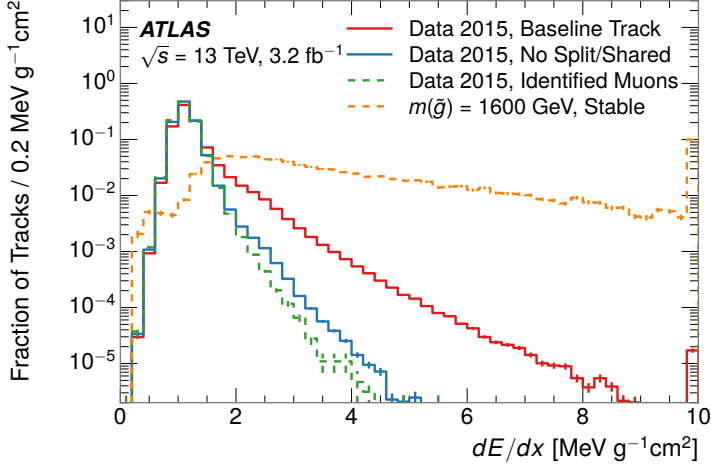


Figure 56: The distribution of dE/dx with various selections applied in data and simulated signal events.

1659 A few additional kinematic requirements are imposed to help reduce SM back-
 1660 grounds. The momentum of the candidate track must be at least 150 GeV, and
 1661 the uncertainty on that measurement must be less than 50%. The distribution of
 1662 momentum is shown in Figure 57 for tracks in data and simulated signal events
 1663 after the previously discussed requirements on clusters, transverse momentum,
 1664 and isolation have been imposed. The signal particles are much harder on aver-

age than their backgrounds because of the high energy interactions required to produce them. The transverse mass, M_T , defined as

$$M_T = \sqrt{2p_T E_T^{\text{miss}}(1 - \cos(\Delta\phi(E_T^{\text{miss}}, \text{track})))} \quad (3)$$

estimates the mass of a decay of to a single charged particle and an undetected particle and is required to be greater than 130 GeV to reject contributions from the decay of W bosons. Figure 58 shows the distribution of M_T for data and simulated signal events. The signal is distributed over a wide range of M_T , with about 90% above the threshold value of 130 GeV. The data shows a dual-peaked structure, where the first peak comes from W boson decays and the second peak is a kinematic shaping from the requirements on E_T^{miss} and the track p_T in dijet events.

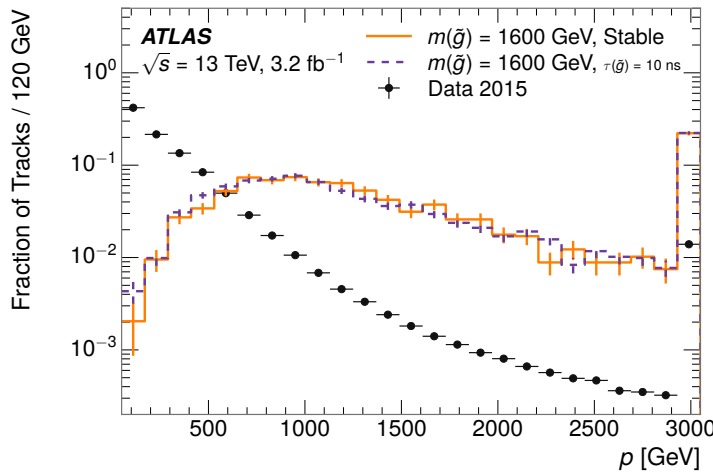


Figure 57: The distribution of track momentum for data and simulated signal events, after previous selection requirements have been applied.

11.3 PARTICLE SPECIES REJECTION

The amount of ionization deposited by particles with low mass and high momentum has a large positive tail [55], so backgrounds can be formed by a wide variety of SM processes when various charged particles have a few randomly large deposits of energy in the pixel detector. Those backgrounds can be additionally reduced by targeting other interactions with the detector where they are expected to have different behavior than R-Hadrons. The interactions with the detector depend on the types of particles produced rather than the processes which produce them, so this search forms a series of rejections to remove backgrounds from individual particle species. These rejections focus on using additional features of the event, other than the kinematics of the candidate track, as they can provide a powerful source of background rejection with very high signal efficiency. However, the lifetime of an R-Hadron can significantly change its

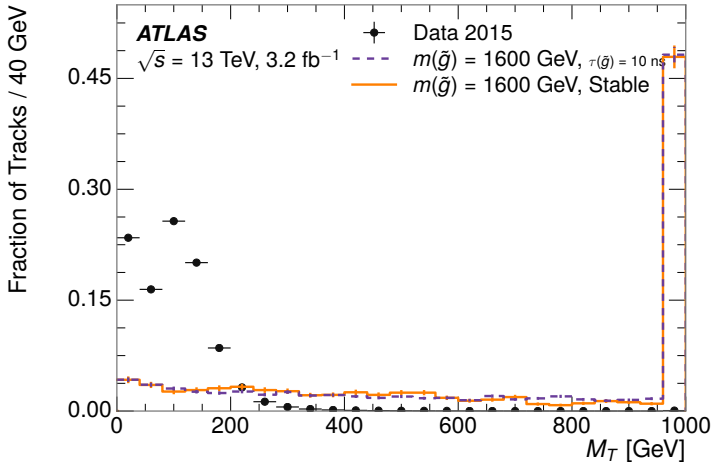


Figure 58: The distribution of M_T for data and simulated signal events, after previous selection requirements have been applied.

1688 detector characteristics, as discussed in Section 10.1.2. To accommodate these
 1689 differences, the SM rejections defined in this section are split to form two signal
 1690 regions, one for long-lifetimes particles, the stable region ($50 \leq \tau[\text{ns}] < \infty \text{ ns}$),
 1691 and one for intermediate lifetime particles, the metastable region ($0.4 < \tau[\text{ns}] <$
 1692 50).

1693 Jets can be very effectively rejected by considering the larger-scale isolation of
 1694 the candidate track. In this case the isolation focuses on the production of nearby
 1695 particles as a jet-veto, rather than the isolation from overlapping tracks based on
 1696 N_{split} that was used to reduce high-ionization backgrounds. As explained in Sec-
 1697 tion 10.1, the fragmentation process which produces an R-Hadron is very hard
 1698 and thus is not expected to produce additional particles with a summed momen-
 1699 tum of more than 5 GeV. The jet-veto uses the summed momentum of tracks
 1700 with a cone of $\Delta R < 0.25$, referred to as p_T^{Cone} , which is shown in Figure 59 for
 1701 data and simulated signal events. In the data this value has a peak at zero from
 1702 isolated tracks such as leptons, and a long tail from jets which contains as much
 1703 as 80% of the background above 20 GeV at this stage of the selection. In signal
 1704 events p_T^{Cone} is strongly peaked at zero and significantly less than 1% of signal
 1705 events have p_T^{Cone} above 20 GeV. This makes a requirement of $p_T^{\text{Cone}} < 20 \text{ GeV}$
 1706 a very effective method to reject background without losing signal efficiency.
 1707 For the stable signal region, this cut is further tightened to $p_T^{\text{Cone}} < 5 \text{ GeV}$ as
 1708 it is the most effective variable remaining to extend the search reach for long
 1709 lifetimes.

1710 Even for fully isolated particles, there are additional methods to reject each
 1711 type of particle using information in the muon system and calorimeters. Muons
 1712 can be identified very reliably using the tracks in the muon system, as described
 1713 in Section 7.4. For intermediate lifetimes the LLPs do not survive long enough
 1714 to reach the muon system, and so muons are vetoed by rejecting tracks that as-
 1715 sociate to a muon with medium muon identification requirements (Section 7.4).
 1716 For longer lifetimes, this rejection is not applied because LLPs which reach the

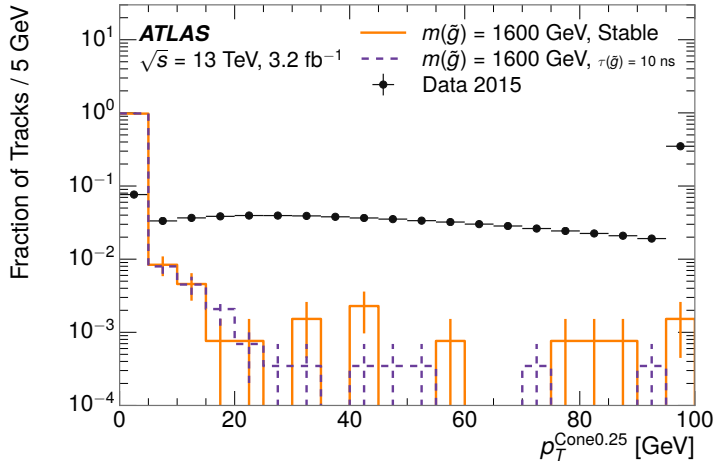


Figure 59: The distribution of summed tracked momentum within a cone of $\Delta R < 0.25$ around the candidate track for data and simulated signal events, after previous selection requirements have been applied.

1717 muon system can be identified as muons as often as 30% of the time in simulated
 1718 samples.

1719 Calorimeter-based particle rejection relies on the expected small deposits of
 1720 energy from LLPs. When the lifetime is long enough to reach the calorimeter, a
 1721 LLP deposits little of its energy as it traverses the material, as discussed in Sec-
 1722 tion 10.1. Even when the particle does decay before the calorimeter, the major-
 1723 ity of its energy is carried away by the LSP and not deposited in the calorimeter.
 1724 In both cases the energy is expected to be distributed across the layers of the
 1725 calorimeters and not peaked in just one layer. This can be quantified in terms
 1726 of E/p , the ratio of calorimeter energy of a nearby jet to the track momentum,
 1727 and f_{EM} , the fraction of energy in that jet within the electromagnetic calorime-
 1728 ter. When no jets fall within a cone of 0.05 of the particle, E/p and f_{EM} are both
 1729 defined as zero. E/p is expected to be above 1.0 for typical SM particles because
 1730 of calibration and the contributions from other nearby particles, as discussed in
 1731 Chapter ???. At these momenta there is no significant zero fraction due to inter-
 1732 actions with the detector or insufficient energy deposits (see Section 8.2.2). f_{EM}
 1733 is peaked close to 1.0 for electrons, and distributed between 10% and 90% for
 1734 hadrons.

1735 These trends can be seen in the two dimensional distribution for signal in
 1736 Figure 60 for stable and metastable (10 ns) events. The majority of R-Hadrons
 1737 in both samples fall into the bin for $E/p = 0$ and $f_{\text{EM}} = 0$ because the majority
 1738 of the time there is no associated jet. In the stable sample, when there often is
 1739 an associated jet, E/p is typically still below 0.1, and the f_{EM} is predominantly
 1740 under 0.8. In the metastable sample, on the other hand, E/p is larger but still
 1741 typically below 0.1 because of actual jets produced during the decay. The f_{EM} is
 1742 much lower on average in this case, below 0.1, because the 10 ns lifetime particles
 1743 rarely decay before passing through the electromagnetic calorimeter. Figure 60
 1744 also includes simulated Z decays to electrons or tau leptons. From the decays

1745 to electrons it is clear that the majority of electrons have f_{EM} above 0.9. The
 1746 tau decays include a variety of products. Muons can be seen in the bin where
 1747 $E/p = 0$ and $f_{\text{EM}} = 0$ because they do not have an associated jet. Electrons fall
 1748 into the range where $E/p > 1$ and $f_{\text{EM}} > 0.9$. Hadronic tau decays are the most
 1749 common, and fall in the range of $0.1 < f_{\text{EM}} < 0.9$ and $E/p > 1.0$.

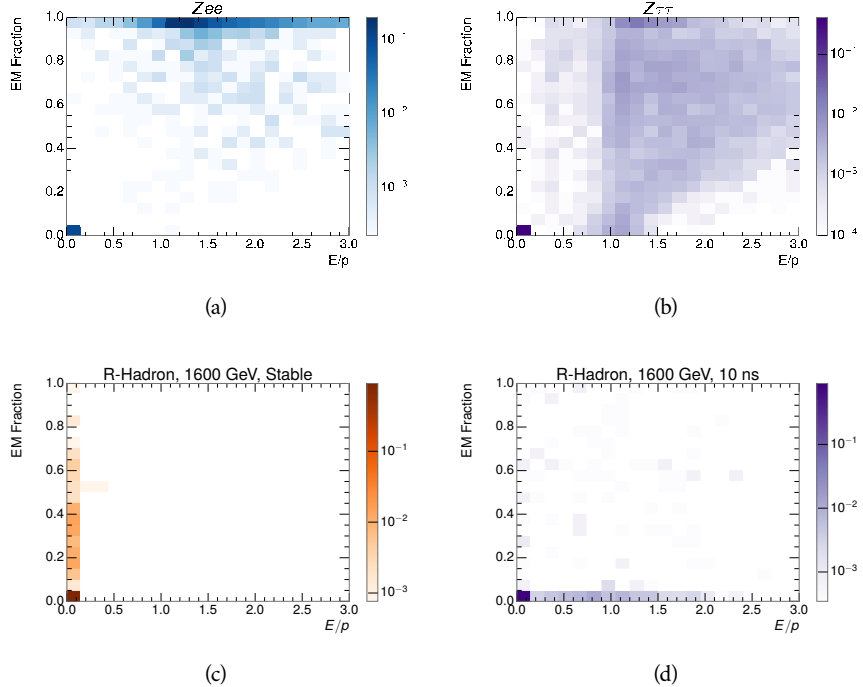


Figure 60: The normalized, two-dimensional distribution of E/p and f_{EM} for simulated
 (a) $Z \rightarrow ee$, (b) $Z \rightarrow \tau\tau$, (c) 1200 GeV Stable R-Hadron events, and (d) 1200
 GeV, 10 ns R-Hadron events.

1750 These differences motivate an electron rejection by requiring an f_{EM} below
 1751 0.9. Similarly, isolated hadrons are rejected by requiring $E/p < 1.0$. These re-
 1752 quirements combine to remove the majority of isolated electrons and hadrons
 1753 but retain over 95% of the simulated signal across a range of masses and lifetimes.

1754 11.4 IONIZATION

1755 The final requirement on the candidate track is the primary discriminating vari-
 1756 able, the ionization in the pixel detector. That ionization is measured in terms
 1757 of dE/dx , which was shown for data and simulated signal events in Figure 56.
 1758 dE/dx is dramatically greater for the high mass signal particles than the back-
 1759 grounds, which start to fall immediately after the minimally ionizing peak at 1.1
 1760 $\text{MeV g}^{-1} \text{cm}^2$. The dE/dx for candidate tracks must be greater than a pseudorapidity-
 1761 dependent threshold, specifically $1.80 - 0.11|\eta| + 0.17\eta^2 - 0.05\eta^3 \text{ MeV g}^{-1} \text{ cm}^{-2}$,
 1762 in order to correct for an approximately 5% dependence of the MIP peak on η .
 1763 The requirement was chosen as part of the signal region optimization, and man-

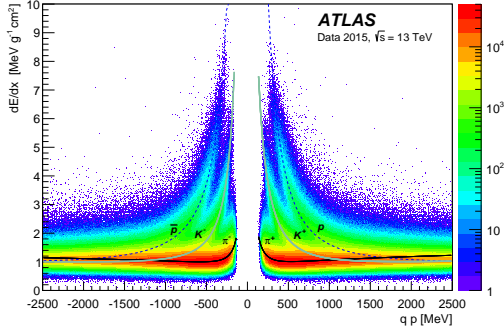


Figure 61: Two-dimensional distribution of dE/dx versus charge signed momentum (qp) for minimum-bias tracks. The fitted distributions of the most probable values for pions, kaons and protons are superimposed.

ages to reduce the backgrounds by a factor of 100 while remaining 70-90% efficient for simulated signal events depending on the mass.

11.4.1 MASS ESTIMATION

The mean value of ionization in silicon is governed by the Bethe equation and the most probable value follows a Landau-Vavilov distribution [55]. Those forms inspire a parametric description of dE/dx in terms of $\beta\gamma$,

$$(dE/dx)_{MPV}(\beta\gamma) = \frac{p_1}{\beta^{p_3}} \ln(1 + [p_2 \beta\gamma]^{p_5}) - p_4 \quad (4)$$

which performs well in the range $0.3 < \beta\gamma < 1.5$. This range includes the expected range of $\beta\gamma$ for the particles targeted for this search, with $\beta\gamma \approx 2.0$ for lower mass particles ($O(100 \text{ GeV})$) and up to $\beta\gamma \approx 0.5$ for higher mass particles ($O(1000 \text{ GeV})$). The parameters, p_i , are fit using a 2015 data sample of low-momentum pions, kaons, and protons as described in Ref. [76]. Figure 61 shows the two-dimensional distribution of dE/dx and momentum along with the above fitted values for $(dE/dx)_{MPV}$.

The above equation (4) is then numerically inverted to estimate $\beta\gamma$ and the mass for each candidate track. In simulated signal events, the mean of this mass value reproduces the generated mass up to around 1800 GeV to within 3%, and a 3% shift is applied to correct for this difference. The mass distributions prior to this correction are shown for a few stable mass points in Figure 62. The large widths of these distributions come from the high variability in energy deposits in the pixel detector as well as the uncertainty on momentum measurements at high momentum, but the means converge to the expected values.

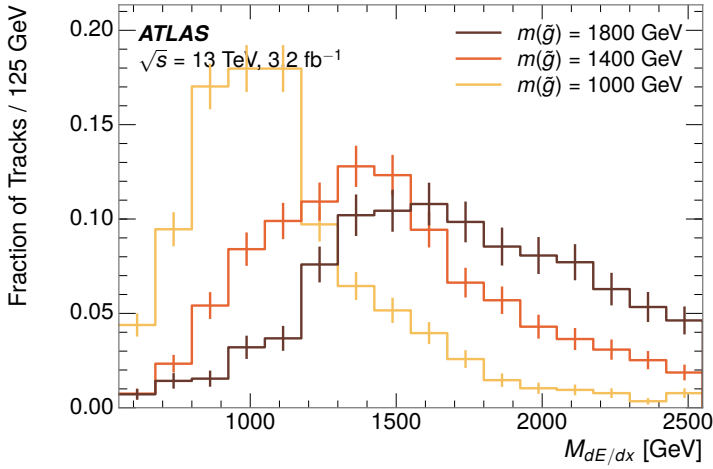


Figure 62: The distribution of mass estimated using dE/dx for simulated stable R-Hadrons with masses between 1000 and 1600 GeV.

This analysis evaluates expected yields and the resulting cross sectional limits using windows in this mass variable. The windows are formed by fitting mass distributions in simulated signal events like those in Figure 62 to Gaussian distributions and taking all events that fall within $\pm 1.4\sigma$ of the mean. As can be seen in Figure 62, typical values for this width are $\sigma \approx 300 - 500$ GeV depending on the generated mass.

11.5 EFFICIENCY

The numbers of events passing each requirement through ionization are shown in Table 3 for the full 2015 dataset and a simulated 1600 GeV, 10 ns lifetime R-Hadron sample. The table highlights the overall acceptance \times efficiency for signal events, which for this example is 19%. Between SM rejection and ionization, this signal region reduces the background of tracks which pass the kinematic requirements down by an additional factor of almost 2000.

There is a strong dependence of this efficiency on lifetime and mass, with efficiencies dropping to under 1% at low lifetimes. Figure 63 shows the dependence on both mass and lifetime for all signal samples considered in this search. The dependence on mass is relatively slight and comes predominantly from the increasing fraction of R-Hadrons which pass the ionization cut with increasing mass. The trigger and E_T^{miss} requirements are most efficient for particles that decay before reaching the calorimeters. However, the chance of a particle to be reconstructed as a high-quality track decreases significantly at low lifetimes as the particle does not propagate sufficiently through the inner detector. These effects lead to a maximum in the selection efficiency for lifetimes around 10-30 ns.

The inefficiency of this signal region at short lifetimes comes almost exclusively from an acceptance effect, in that the particles do not reach the necessary

Selection	Exp. Signal Events	Observed Events in 3.2 fb^{-1}
Generated	26.0 ± 0.3	
E_T^{miss} Trigger	24.8 ± 0.3 (95%)	
$E_T^{\text{miss}} > 130 \text{ GeV}$	23.9 ± 0.3 (92%)	
Track Quality and $p_T > 50$	10.7 ± 0.2 (41%)	368324
Isolation Requirement	9.0 ± 0.2 (35%)	108079
Track $p > 150 \text{ GeV}$	6.6 ± 0.2 (25%)	47463
$M_T > 130 \text{ GeV}$	5.8 ± 0.2 (22%)	18746
Electron and Hadron Veto	5.5 ± 0.2 (21%)	3612
Muon Veto	5.5 ± 0.2 (21%)	1668
Ionization Requirement	5.0 ± 0.1 (19%)	11

Table 3: The expected number of events at each level of the selection for metastable $1600 \text{ GeV}, 10 \text{ ns}$ R-Hadrons, along with the number of events observed in data, for 3.2 fb^{-1} . The simulated yields are shown with statistical uncertainties only. The total efficiency \times acceptance is also shown for the signal.

1811 layers of the SCT. This can be seen more clearly by defining a fiducial region
 1812 which includes events with at least one R-Hadron that is produced with non-
 1813 zero charge, $p_T > 50 \text{ GeV}$, $p > 150 \text{ GeV}$, $|\eta| < 2.5$, and a decay distance greater
 1814 than 37 cm in the transverse plane. At short (1 ns) lifetimes, the acceptance into
 1815 this region is as low as 4%. Once this acceptance is accounted for, the selection
 1816 efficiency ranges from 25% at lifetimes of 1 ns up to 45% at lifetimes of 10 ns.

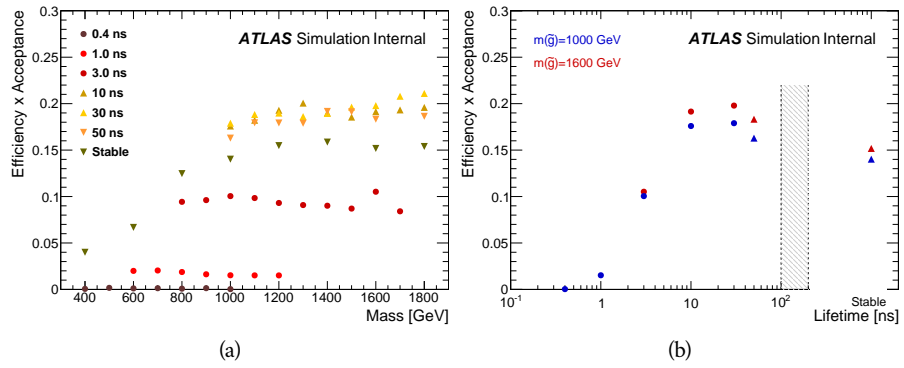


Figure 63: The acceptance \times efficiency as a function of R-Hadron (a) mass and (b) lifetime. (a) shows all of the combinations of mass and lifetime considered in this search, and (b) highlights the lifetime dependence for 1000 GeV and 1600 GeV R-Hadrons.

1817

1818 BACKGROUND ESTIMATION

1819 The event selection discussed in the previous section focuses on detector signa-
 1820 tures, emphasizing a single high-momentum, highly-ionizing track. That track
 1821 is then required to be in some way inconsistent with the expected properties
 1822 of SM particles, with various requirements designed to reject jets, hadrons,
 1823 electrons, and muons (Section 11.3). Therefore the background for this search comes
 1824 entirely from reducible backgrounds that are outliers of various distributions in-
 1825 cluding dE/dx , f_{EM} , and p_T^{Cone} . The simulation can be tuned in various ways to
 1826 do an excellent job of modeling the average properties of each particle type [77],
 1827 but it is not necessarily expected to accurately reproduce outliers. For this rea-
 1828 sons, the background estimation used for this search is estimated entirely using
 1829 data.

1830 12.1 BACKGROUND SOURCES

1831 SM charged particles with lifetimes long enough to form tracks in the inner de-
 1832 tector can be grouped into three major categories based on their detector inter-
 1833 actions: hadrons, electrons, and muons. Every particle that enters into the back-
 1834 ground for this search belongs to one of these types. Relatively pure samples of
 1835 tracks from each of these types can be formed in data by inverting the various
 1836 rejection techniques in Section 11.3. Specifically, muons are selected requiring
 1837 medium muon identification, electrons requiring $E/p > 1.0$ and $f_{\text{EM}} > 0.95$,
 1838 and hadrons requiring $E/p > 1.0$ and $f_{\text{EM}} < 0.95$.

1839 Figure 64 shows the distributions of momentum and dE/dx for these cate-
 1840 gories in data, after requiring the event level selection as well as the track re-
 1841 quirements on p_T , hits, and N_{split} , as discussed in Section 11.2. Simulated signal
 1842 events are included for reference. These distribution are only illustrative of the
 1843 differences between types, as the rejection requirements could alter their shape.
 1844 This is especially significant for momentum which enters directly into E/p and
 1845 can indirectly affect muon identification. However the various types show clear
 1846 differences in both distributions. The distributions of momentum are not nec-
 1847 essarily expected to match between the various types because the production
 1848 mechanisms for each type result in different kinematic distributions. dE/dx is
 1849 also different between types because of incomplete isolation; although the re-
 1850 quirement on N_{split} helps to reduce the contribution of nearby particles it does
 1851 not completely remove the effect of overlaps. Muons are better isolated because
 1852 they do not have the additional particle from hadronization present for hadrons
 1853 and they are significantly less likely do interact with the detector and produce
 1854 secondary particles compared to hadrons and electrons. Thus muons have the
 1855 smallest fraction of dE/dx above the threshold of $1.8 \text{ MeVg}^{-1}\text{cm}^2$; hadrons and
 1856 electrons have a larger fraction above this threshold.

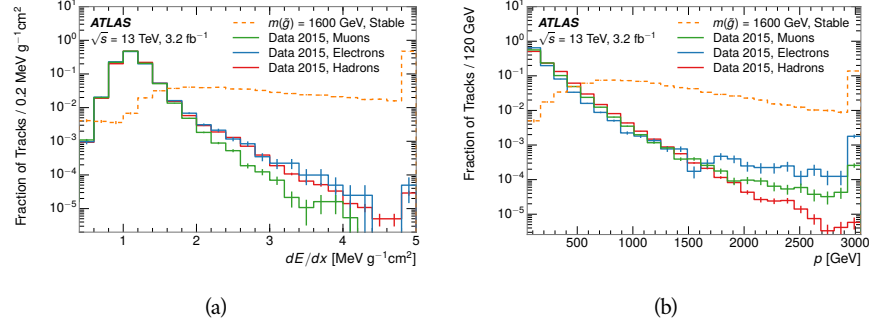


Figure 64: The distribution of (a) dE/dx and (b) momentum for tracks in data and simulated signal after requiring the event level selection and the track selection on p_T , hits, and N_{split} . Each sub-figure shows the normalized distributions for tracks classified as hadrons, electrons, and muons in data and R-Hadrons in the simulated signal.

1857 It is difficult to determine what fraction of each particle type enters into the fi-
 1858 nal signal region. The background method will not have significant dependence
 1859 on the relative contributions of each species, but it is useful to understand the
 1860 differences between each when considering the various tests of the method.

1861 12.2 PREDICTION METHOD

1862 The data-driven background estimation relies on the independence between ion-
 1863 ization and other kinematic variables in the event. For standard model particles
 1864 with momenta above 50 GeV, dE/dx is not correlated with momentum; though
 1865 there is a slight relativistic rise as momentum increases, the effect is small com-
 1866 pared to the width of the distribution of ionization energy deposits.. So, the
 1867 proposed method to estimate the mass distribution of the signal region is to use
 1868 momentum from a track with low dE/dx (below the threshold value) and to com-
 1869 bine it with a random dE/dx value from a dE/dx template. The resulting track is
 1870 just as likely as the original, so a number of such random generations provide the
 1871 expected distributions of momentum and ionization. These are then combined
 1872 using the parametrization described in Section 11.4.1 to form a distribution of
 1873 mass for the signal region.

1874 Algorithmically this method is implemented by forming two distinct Control
 1875 Regions (**CR**s). The first **CR**, CR1, is formed by applying the entire event selec-
 1876 tion from Chapter 11 up to the dE/dx and mass requirements. The dE/dx re-
 1877 quirement is instead inverted for this region. Because of the independence of
 1878 dE/dx , the tracks in this control region have the same kinematic distribution
 1879 as the tracks in the signal region, and are used to measure a two-dimensional
 1880 template of p and η . The second **CR**, CR2, is formed from the event selection
 1881 through the dE/dx requirement, but with an inverted E_T^{miss} requirement. The
 1882 tracks in this control region are expected to have similar dE/dx distributions to
 1883 the signal region before the ionization requirement, and so this region is used to
 1884 measure a two-dimensional template of dE/dx and η .

1885 The contribution of any signal to the control regions is minimized by the in-
 1886 verted selection requirements. Only less than 10% of simulated signal events
 1887 have either dE/dx or E_T^{miss} below the threshold values in the original signal re-
 1888 gion, while the backgrounds are significantly enhanced by inverting those re-
 1889 quirements. The signal contamination is less than 1% in both control regions
 1890 for all of the simulated masses and lifetimes considered in this analysis.

1891 With those measured templates, the shape of the mass estimation is generated
 1892 by first selecting a random (p , η) combination from CR1. This momentum
 1893 value is combined with a dE/dx value taken from the appropriate distribution
 1894 of dE/dx for the selected η from CR2. The use of η in both random samplings
 1895 controls for any correlation between p , dE/dx , and η . Those values are then
 1896 used to calculate a mass in the same way that is done for regular tracks in data,
 1897 see Section 11.4.1. As this procedure includes all dE/dx values, the cut at 1.8
 1898 MeVg $^{-1}$ cm 2 is then enforced to fully model the signal region. The generated
 1899 mass distribution is then normalized by scaling the background estimate to the
 1900 data in the region $M < 160$ GeV, where signals of this type have already been
 1901 excluded [61]. This normalization uses the distributions of mass generated with-
 1902 out the ionization requirement.

1903 The statistical uncertainties on these background distributions are calculated
 1904 by independently fluctuating each bin of the input templates according to their
 1905 Poisson uncertainties. These fluctuations are repeated a large number of times,
 1906 and the uncertainty on the resulting distribution is taken as the root mean square
 1907 (RMS) deviation of the fluctuations from the average. As the procedure uses one
 1908 million random combinations to generate the distributions, The statistical un-
 1909 certainty from the actual random generations is negligible compared to the un-
 1910 certainty from measuring the templates.

1911 12.3 VALIDATION

1912 The validity of the background estimation technique can be evaluated in both
 1913 data and simulation. The underlying assumption that random combinations of
 1914 dE/dx and momentum can predict a mass distribution in an orthogonal region
 1915 can be tested using simulated samples where concerns like multiple particle types
 1916 can be controlled. Using the same technique in another set of signal-depleted
 1917 regions in data then extends this confidence to the more complicated case where
 1918 several particle species are inherently included.

1919 12.3.1 CLOSURE IN SIMULATION

1920 The first test of the procedure is done using a simulated sample of $W \rightarrow \mu\nu$
 1921 decays. These types of events provide the ingredients required to test the back-
 1922 ground estimate, E_T^{miss} and isolated tracks, with high statistics. In this example
 1923 there is no signal, so simulated events in the orthogonal CRs are used to estimate
 1924 the shape of the mass distribution of the simulated events in the signal region. To
 1925 reflect the different topology for W boson decays, the CRs use slightly modified
 1926 definitions. In all CRs, the requirement of $p > 150$ GeV and the SM rejection

1927 requirements are removed. Additionally, for the signal region the requirement
 1928 on E_T^{miss} is relaxed to 30 GeV and the corresponding inverted requirement on
 1929 CR2 is also set at 30 GeV.

1930 With these modified selections, the simulated and randomly generated distri-
 1931 butions of $M_{dE/dx}$ are shown in Figure 65. This figure includes the mass distri-
 1932 butions before and after the requirement on dE/dx , which significantly shapes
 1933 the distributions. In both cases the background estimation technique repro-
 1934 duces the shape of $M_{dE/dx}$ in the signal region. There is a small difference in the pos-
 1935 itive tail of the mass distribution prior to the ionization cut, where the random
 1936 events underestimate the fraction of tracks with mass above 150 GeV by about
 1937 20%. After the ionization requirement, however, this discrepancy is not present
 1938 and the two distributions agree to within statistical uncertainties.

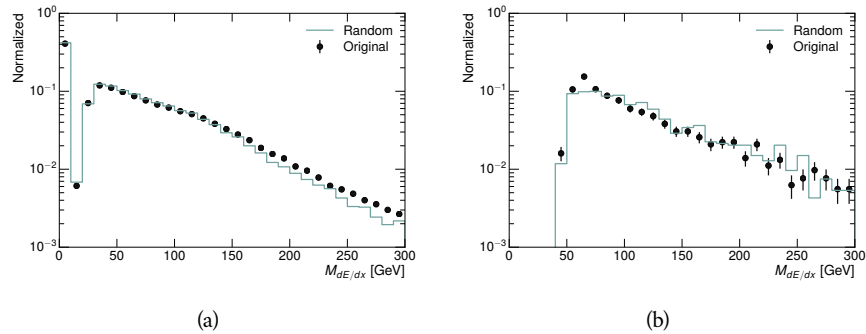


Figure 65: The distribution of $M_{dE/dx}$ (a) before and (b) after the ionization requirement for tracks in simulated W boson decays and for the randomly generated background estimate.

1939 This ability to reproduce the shape of the mass distribution in simulated events
 1940 shows that the technique works as expected. No significant biases are acquired
 1941 in using low dE/dx events to select kinematic templates or in using low E_T^{miss}
 1942 events to select ionization templates, as either would result in a mismodeling of
 1943 the shape of the mass distribution. The simulated events contain only one par-
 1944 ticle type, however, so this test only establishes that the technique works well
 1945 when the the CRs are populated by exactly the same species.

1946 12.3.2 VALIDATION REGION IN DATA

1947 The second test of the background estimate is performed using data in an or-
 1948 thogonal validation region. The validation region, and the corresponding CRs,
 1949 are formed using the same selection requirements as in the nominal method but
 1950 with a modified requirement on momentum, $50 < p[\text{GeV}] < 150$. This allows
 1951 the technique to be checked in a region with very similar properties but where
 1952 the signal is depleted, as the majority of the signal has momentum above 150
 1953 GeV while the backgrounds are enhanced below that threshold. Any biases on
 1954 the particle composition of the CRs for the signal region will be reflected in the
 1955 CRs used to estimate the mass distribution in the validation region.

1956 Figure 66 shows the measured and randomly generated mass distributions for
 1957 data before and after the ionization requirement. The background estimate does
 1958 an excellent job of modeling the actual background before the ionization require-
 1959 ment, with good agreement to within the statistical uncertainties out to the limit
 1960 of the mass distribution. There are very few events in the validation region after
 1961 the ionization requirement, but the few observed events are consistent with the
 1962 background prediction. The good agreement in this validation region provides
 1963 a confirmation that the technique works even in the full-complexity case with
 1964 multiple particle types entering the distributions. Any bias from changes in par-
 1965 ticle composition between regions is small compared to statistical uncertainties.

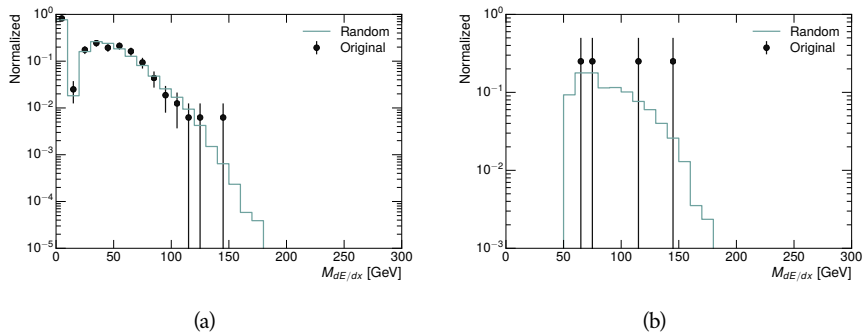


Figure 66: The distribution of $M_{dE/dx}$ (a) before and (b) after the ionization require-
 ment for tracks in the validation region and for the randomly generated back-
 ground estimate.

1966

1967 SYSTEMATIC UNCERTAINTIES AND RESULTS

1968 13.1 SYSTEMATIC UNCERTAINTIES

1969 A number of systematic uncertainties affect the interpretation of the results of
 1970 the search. These uncertainties can broken down into two major categories,
 1971 those which affect the estimate of the background using data and those which
 1972 affect the measurement of the signal yield estimated with simulated events. The
 1973 total measured systematic uncertainties are 7% for the background estimation
 1974 and approximately 32% for the signal yield depending on lifetime. These system-
 1975atic uncertainties are expected to be small compared to the statistical fluctuations
 1976 of the measured yields so that measured cross-sectional limits will be dominated
 1977 by statistical uncertainties. The following sections describe each source of sys-
 1978 tematic uncertainty for each of the two types.

1979 13.1.1 BACKGROUND ESTIMATE

1980 The systematic uncertainties on the background estimate come primarily from
 1981 considering alternative methods for generating the background distributions.
 1982 These uncertainties are small compared to the statistical uncertainties on the
 1983 background estimate which come from the limited statistics in measuring the
 1984 template distributions, as described in Section 12.2. They are summarized in
 1985 Table 4.

Source of Uncertainty:	Value [%]
Analytic Description of dE/dx	4.0
Muon Fraction (Stable Region only)	3.0
IBL Ionization Correction	3.8
Normalization	3.0
Total (Metastable Region):	6.3
Total (Stable Region):	7.0

Table 4: A summary of the sources of systematic uncertainty for the data-driven background in the signal region. If the uncertainty depends on the mass, the maximum values are reported.

1986 13.1.1.1 ANALYTIC DESCRIPTION OF DE/DX

1987 The background estimate uses a binned template distribution to estimate the
 1988 dE/dx of tracks in the signal region, as described in Section 12.2. It is also possi-

ble to fit that measured distribution to a functional form to help smooth the distribution in the tails of dE/dx where the template is driven by a small number of tracks. Both Landau convolved with a Gaussian and Crystal Ball functions are considered as the functional form and used to re-estimate the background distribution. The deviations compared to the nominal method are found to be 4%, and this is taken as a systematic uncertainty to cover the inability carefully predict the contribution from the long tail of dE/dx where there are few measurements available in data.

13.1.1.2 MUON FRACTION

The stable region of the analysis explicitly includes tracks identified as muons, which have a known difference in their dE/dx distributions compared to non-muon tracks (Section 12.1). To account for a difference in muon fraction between the background region and the signal region for this selection, the dE/dx templates for muons and non-muons are measured separately and then the relative fraction of each is varied in the random generation. The muon fraction is varied by its statistical uncertainty and the resulting difference of 3% in background yield is taken as the systematic uncertainty.

13.1.1.3 IBL CORRECTIONS

The Insertible B-Layer (IBL), described in Section 6.3.1, received a significant dose of radiation during the data collection in 2015. The irradiation can cause a drift in the frontend electronics and thus alter the dE/dx measurement which includes the ToT output by the IBL. These effects are corrected for in the nominal analysis by scaling the dE/dx measurements by a constant factor derived for each run to match the average dE/dx value to a reference run where the IBL was known to be stable to this effect. However, this corrective factor does not account for inter-run variations. To account for this potential drift of dE/dx , the correction procedure is repeated by varying the corrections up and down by the maximal run-to-run variation from the full data-taking period, which results in an uncertainty of 3.8%.

13.1.1.4 NORMALIZATION

As described in Section 12.2, the generated distribution of masses is normalized in a shoulder region ($M < 160$ GeV) where signals have been excluded by previous analyses. That normalization factor is varied by its statistical uncertainty and the resulting fluctuation in the mass distribution of 3% is taken as a systematic uncertainty on the background estimate.

13.1.2 SIGNAL YIELD

The systematic uncertainties on the signal yield can be divided into three categories; those on the simulation process, those on the modeling of the detector efficiency or calibration, and those affecting the overall signal yield. They are summarized in Table 4. The largest uncertainty comes from the uncertainty on

2029 the production cross section for gluinos, which is the dominant systematic un-
 2030 certainty in this analysis.

Source of Uncertainty	-[%]	+[%]
ISR Modeling (Metastable Region)	1.5	1.5
ISR Modeling (Stable Region)	14	14
Pile-up Reweighting	1.1	1.1
Trigger Efficiency Reweighting	0.9	0.9
E_T^{miss} Scale	1.1	2.2
Ionization Parametrization	7.1	0
Momentum Parametrization	0.3	0.0
Electron Rejection	0.0	0.0
Hadron Rejection	0.0	0.0
μ Identification	4.3	4.3
Luminosity	5	5
Signal size uncertainty	28	28
Total (Metastable Region)	30	29
Total (Stable Region)	33	32

Table 5: A summary of the sources of systematic uncertainty for the simulated signal yield. The uncertainty depends on the mass and lifetime, and the maximum negative and positive values are reported in the table.

2031 13.1.2.1 ISR MODELING

2032 As discussed in Section 10.2, MadGraph is expected to reproduce the distribution
 2033 of ISR in signal events more accurately than the nominal Pythia samples. The
 2034 analysis reweights the distribution of ISR in the simulated signal events to match
 2035 the distribution found in generated MadGraph samples. This has an effect on the
 2036 selection efficiency in the signal samples, where ISR contributes to the generation
 2037 of E_T^{miss} . To account for the potential inaccuracy on the simulation of ISR at high
 2038 energies, half of the difference between the signal efficiency with the reweighted
 2039 distribution and the original distribution is taken as a systematic uncertainty.

2040 13.1.2.2 PILEUP REWEIGHTING

2041 The simulated events were generated prior to data collection with an estimate of
 2042 the average number of interactions per bunch crossing. This estimate does not
 2043 match the value of pileup during actual data collection, but a large fraction of the
 2044 simulated events would be discarded in order to match the distribution in data.
 2045 Therefore the simulated signal events are not reweighted for pileup by default
 2046 in the analysis. The effect of the pileup on signal efficiency is not expected to
 2047 depend on the mass or lifetime of the generated signal events, which allows all

2048 of the generated signal events to be used together to assess the pileup dependence.
 2049 To account for the potential effect of the difference in the number of interactions
 2050 per bunch crossing between data and simulation, the difference in yield between
 2051 the nominal signal events and the reweighted events averaged over all masses
 2052 and lifetimes is taken as a systematic uncertainty on the yield for each mass and
 2053 lifetime (1.1%).

2054 13.1.2.3 TRIGGER EFFICIENCY REWEIGHTING

2055 As described in Section 11.2, the selection for this analysis does not require a suf-
 2056 ficiently large value of E_T^{miss} to be above the plateau of trigger efficiency. There-
 2057 fore, some signal events which would otherwise pass the event selection can be
 2058 excluded because of the trigger requirement. These effects can be difficult to es-
 2059 timate in simulation, and thus are constrained by comparing data and simulated
 2060 events in an alternative W boson region which uses decays to muons to find a rel-
 2061 atively pure sample of events with missing energy. The trigger efficiency for data
 2062 and simulated W events are shown in Figure 67. The comparison between data
 2063 and MC in this region constrains the simulation of the trigger efficiency. The
 2064 simulated signal events are reweighted by the ratio of data to simulation in the
 2065 W boson decays, while the difference between the data and simulation in those
 2066 decays is taken as a systematic uncertainty. This results in an uncertainty of only
 2067 0.9% as the majority of events are well above the plateau and the disagreement
 2068 between data and simulation is small even below that plateau.

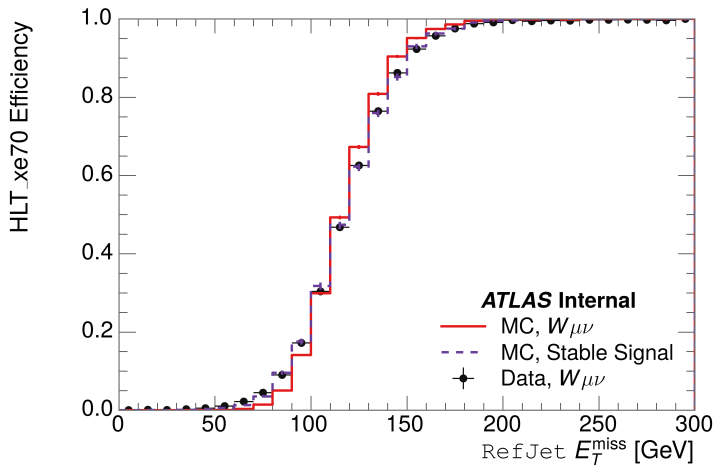


Figure 67: The trigger efficiency for the HLT_xe70 trigger requirement as a function of Calorimeter E_T^{miss} for simulated data events with a W boson selection. Simulated signal events and simulated W boson events are also included.

2069 13.1.2.4 MISSING TRANSVERSE MOMENTUM SCALE

2070 The ATLAS Combined Performance (CP) group provides a default recommenda-
 2071 tion for systematic variations of jets and missing energy (**note: I'm not quite**
 2072 **sure what to cite for this - I don't see any papers from the jet/met group**

Systematic Variation	-[%]	+[%]
JET_GroupedNP_1	-0.7	1.3
JET_GroupedNP_2	-0.7	1.2
JET_GroupedNP_3	-0.5	1.3

Table 6: Example of the contributing systematic variations to the total systematic for the E_T^{miss} Scale, as measured in a 1200 GeV, Stable R-Hadron signal sample.

2073 **after this was implemented).** These variations enter into this analysis only in
 2074 the requirement on E_T^{miss} . The effect of the measured scale of E_T^{miss} is evaluated
 2075 by varying the E_T^{miss} scale according to the one sigma variations provided by all
 2076 **CP** recommendations on objects affecting event kinematics in simulated signal
 2077 events. Missing energy is reconstructed from fully reconstructed objects so any
 2078 systematic uncertainties affecting jets, muons, electrons, or the E_T^{miss} soft terms
 2079 are included. The only non-negligible contributions found using this method are
 2080 itemized in Table 6 for an example signal sample (1200 GeV, Stable R-Hadron),
 2081 where the systematic is measured as the relative difference in the final signal ef-
 2082 ficiency after applying the associated variation through the CP tools. The only
 2083 variations that are significant are the grouped jet systematic variations, which
 2084 combine recommended jet systematic uncertainties into linearly independent
 2085 variations.

2086 As the peak of the reconstructed E_T^{miss} distribution in the signal is significantly
 2087 above the current threshold for events which pass the trigger requirement, the
 2088 effect of scale variation is expected to be small, which is consistent with the mea-
 2089 sured systematic of approximately 2%. Events which do not pass the trigger re-
 2090 quirement usually fail because there are no ISR jets in the event to balance the
 2091 R -hadrons' transverse momentum, so the reconstructed E_T^{miss} is low and there-
 2092 fore also expected to be not very sensitive to scale changes.

2093 13.1.2.5 MOMENTUM PARAMETRIZATION

2094 The uncertainty on the signal efficiency from track momentum is calculated us-
 2095 ing the **CP** group recommendations for tracks. In particular, only one recom-
 2096 mended systematic variation affects track momentum, the sagitta bias for q/P .
 2097 This uncertainty is propagated to the final selection efficiency by varying the
 2098 track momentum by the recommended one sigma variation, and the associated
 2099 uncertainty is found to be negligible (0.3%).

2100 13.1.2.6 IONIZATION REQUIREMENT

2101 The dE/dx distributions in data and simulated events have different most prob-
 2102 able values, which is due in part to radiation effects in the detector that are not
 2103 fully accounted for in the simulation. The difference does not affect the mass
 2104 measurement used in this analysis, as independent calibrations are done in sim-
 2105 ulation and in data. However, it does affect the efficiency of the high dE/dx
 2106 selection requirement. To calculate the size of the effect on the signal efficiency,

2107 the dE/dx distribution in signal simulation is scaled by a scale factor obtained
 2108 from comparing the dE/dx distribution of inclusive tracks in data and in sim-
 2109 ulation. The difference in efficiency for this sample with a scaled dE/dx dis-
 2110 tribution, relative to the nominal case, is taken as a systematic uncertainty on
 2111 signal efficiency. The uncertainty is as large as 7% for low masses and falls to a
 2112 negligible effect for large masses.

2113 13.1.2.7 ELECTRON AND JET REJECTION

2114 The systematic uncertainty on the electron rejection is measured by varying the
 2115 EM fraction requirement significantly, from 0.95 to 0.9. This is found to have
 2116 a less than 0.04% effect on signal acceptance, on average, and so is completely
 2117 negligible. Similarly, the uncertainty on jet rejection is measured by tightening
 2118 the E/p requirement from 0.5 to 0.4. This is found to have no effect on signal
 2119 acceptance, so again the systematic is again negligible.

2120 13.1.2.8 MUON VETO

2121 The metastable signal region requires that the candidate tracks are not identi-
 2122 fied as medium muons because the majority of R-Hadrons in the lifetime range
 2123 included in that region do not reach the muon spectrometers before they de-
 2124 cay. However, the exponential tail of the R-Hadron lifetime distribution results
 2125 in some R-Hadrons traversing the muon spectrometer. These can still fail the
 2126 muon medium identification because they can fail on the requirement on the
 2127 number of precision hits required to pass the loose selection because they ar-
 2128 rive late to the muon spectrometer. This can be seen in Figure 68, which shows
 2129 the efficiency of the muon veto as a function of $1/\beta$, for two simulated stable
 2130 R-Hadron samples.

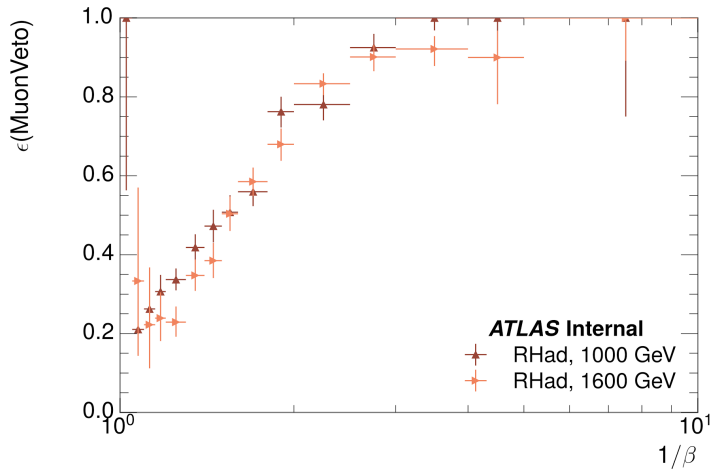


Figure 68: The efficiency of the muon veto for R -hadrons of two different masses, as a function of $\frac{1}{\beta}$ for simulated R-Hadron tracks.

2131 Thus, the efficiency of the muon veto depends on the timing resolution of the
 2132 spectrometer, so an uncertainty is applied to the signal efficiency to cover dif-

2133 differences in timing resolution between data and simulation. First, a sample of
 2134 $Z \rightarrow \mu\mu$ events is selected in data in which one of the muons has a late arrival
 2135 time measured in the Monitored Drift Tube ([MDT](#)). Then the reconstructed β
 2136 distribution is compared to the distribution in simulated $Z \rightarrow \mu\mu$ events; the
 2137 difference between these two distributions reflects the difference in timing res-
 2138 olution between data and simulation. To emulate this difference in simulated
 2139 signal events, the magnitude of the difference is used to scale and shift the true
 2140 β distribution of R-Hadrons in simulation. Signal events are then reweighted
 2141 based on this varied β distribution, and the difference in the efficiency of the
 2142 muon veto selection is compared with the nominal and reweighted true β distri-
 2143 butions. The difference in muon veto efficiency is taken as a systematic uncer-
 2144 tainty of the muon veto.

2145 The comparison of reconstructed β between data and simulation is performed
 2146 separately in the barrel, transition, and endcap regions of the spectrometer, and
 2147 the reweighting of the true β distribution in signal is done per region. The com-
 2148 parison of average reconstructed [MDT](#) β between data and simulation for the
 2149 barrel region is shown in Figure 69 for $Z \rightarrow \mu\mu$ events. As expected, The uncer-
 2150 tainty is found to be negligible for R-hadrons with short lifetimes, and is only
 2151 significant for lifetimes above 30 ns.

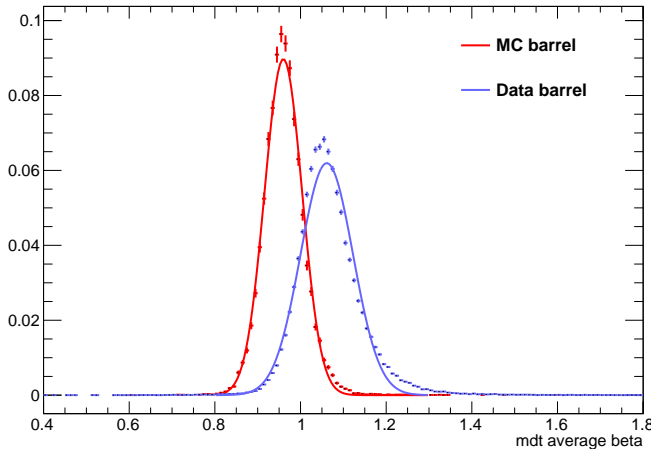


Figure 69: The average reconstructed MDT β distribution for $Z \rightarrow \mu\mu$ events in which
 one of the muons is reconstructed as a slow muon, for both data and simula-
 tion. A gaussian fit is superimposed.

2152 13.1.2.9 LUMINOSITY

2153 The luminosity uncertainty is provided by a luminosity measurement on [ATLAS](#)
 2154 and was measured to be 5% at the time of the publication of this analysis.

2155 13.1.2.10 SIGNAL SIZE

2156 As discussed in Section 10.2, the signal cross sections are calculated at [NLO](#) in the
 2157 strong coupling constant with a resummation of soft-gluon emission at [NLL](#). The

Selection Region	Expected Background	Data
Stable	$17.2 \pm 2.6 \pm 1.2$	16
Metastable	$11.1 \pm 1.7 \pm 0.7$	11

Table 7: The estimated number of background events and the number of observed events in data for the specified selection regions prior to the requirement on mass. The background estimates show statistical and systematic uncertainties.

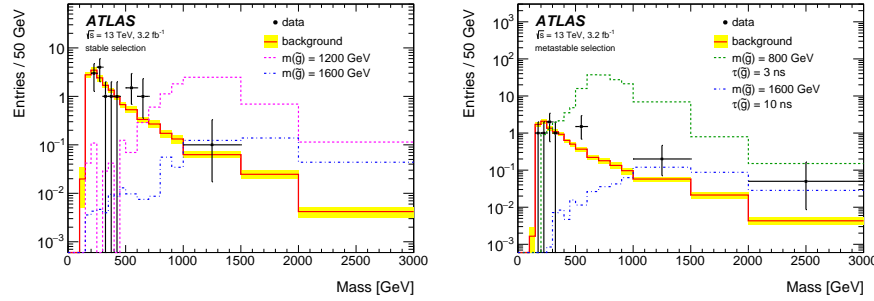


Figure 70: The observed mass distribution of events in data and the generated background distribution in (a) the stable and (b) the metastable signal region. A few example simulated signal distributions are superimposed.

uncertainties on those cross sections are between 14% to 28% for the R-Hadrons in the range of 400 to 1800 GeV [73, 74], where the uncertainty increases with the mass.

13.2 FINAL YIELDS

This full analysis was performed using the 3.2 fb^{-1} from the 2015 data-taking. Using the selections discussed in Chapter 11, sixteen events were observed in the stable signal region and eleven events were observed in the metastable signal region, prior to requirements on the candidate track mass. The background estimate discussed in Chapter 12 predicts $17 \pm 2.6(\text{stat}) \pm 1.2(\text{syst})$ events for the stable region and $11.1 \pm 1.7(\text{stat}) \pm 0.7(\text{syst})$ events for the metastable region. These counts are summarized in Table 7.

The mass estimated using dE/dx (Section 11.4.1) provides the final discriminating variable, where the signal would be expected as an excess in the falling exponential tail of the expected background. The observed distribution of masses is shown in Figure 70, along with the predicted distribution from the background estimate for each signal region. Both include a few example simulated signal distributions, which show the scale of an excess were the R-Hadron signals present. There is no statistically significant evidence of an excess in the data over the background estimation. From this distribution it is clearly possible to rule out signals with lower masses, around 1200 GeV, which have larger cross sections.

2178 13.3 CROSS SECTIONAL LIMITS

2179 Because there is no observed significant excess of events in the signal region, this
 2180 analysis sets upper limits on the allowed cross section for R-Hadron production.
 2181 These limits are set for each mass point by counting the observed events in data,
 2182 along with the expected background and simulated signal events, in windows of
 2183 mass. The mass windows are formed by fitting the distribution of signal events to
 2184 a Gaussian distribution, and the window is then $\pm 1.4\sigma$ around the center of that
 2185 Gaussian. Two examples of the windows formed by this procedure are shown in
 2186 Tables 8-9, for the stable and 10 ns working points. The corresponding counts of
 2187 observed data, expected background, and simulated signal for those same work-
 2188 ing points are shown in Tables 10-11. Appendix B includes the mass windows
 2189 and counts for all of the considered signal points.

$m(\tilde{g})$ [GeV]	Left Extremum [GeV]	Right Extremum [GeV]
1000	655	1349
1100	734	1455
1200	712	1631
1300	792	1737
1400	717	1926
1500	815	2117
1600	824	2122
1700	900	2274
1800	919	2344

Table 8: The left and right extremum of the mass window for each generated mass point with a 10 ns lifetime.

$m(\tilde{g})$ [GeV]	Left Extremum [GeV]	Right Extremum [GeV]
800	627	1053
1000	726	1277
1200	857	1584
1400	924	1937
1600	993	2308
1800	1004	2554

Table 9: The left and right extremum of the mass window used for each generated stable mass point.

2190 The 95% confidence level upper limits on the cross sections for a large grid of
 2191 masses (between 800 and 1800 GeV) and lifetimes (between 0.4 and stable) are
 2192 extracted from these counts with the CL_S method using the profile likelihood

$m(\tilde{g})$ [GeV]	Expected Signal	Expected Background	Observed Data
800	462.83 ± 14.86	1.764 ± 0.080	2.0
1000	108.73 ± 3.38	1.458 ± 0.070	1.0
1200	31.74 ± 0.95	1.137 ± 0.060	1.0
1400	10.22 ± 0.29	1.058 ± 0.058	1.0
1600	3.07 ± 0.09	0.947 ± 0.054	1.0
1800	1.08 ± 0.05	0.940 ± 0.054	1.0

Table 10: The expected number of signal events, the expected number of background events, and the observed number of events in data with their respective statistical errors within the respective mass window for each generated stable mass point

$m(\tilde{g})$ [GeV]	Expected Signal	Expected Background	Observed Data
1000	144.48 ± 5.14	1.499 ± 0.069	2.0
1100	73.19 ± 2.61	1.260 ± 0.060	2.0
1200	41.54 ± 1.41	1.456 ± 0.067	2.0
1300	22.58 ± 0.77	1.201 ± 0.058	2.0
1400	12.70 ± 0.42	1.558 ± 0.071	2.0
1500	6.73 ± 0.24	1.237 ± 0.060	2.0
1600	3.90 ± 0.13	1.201 ± 0.058	2.0
1700	2.27 ± 0.07	1.027 ± 0.052	2.0
1800	1.34 ± 0.04	1.019 ± 0.052	2.0

Table 11: The expected number of signal events, the expected number of background events, and the observed number of events in data with their respective statistical errors within the respective mass window for each generated mass point with a lifetime of 10 ns.

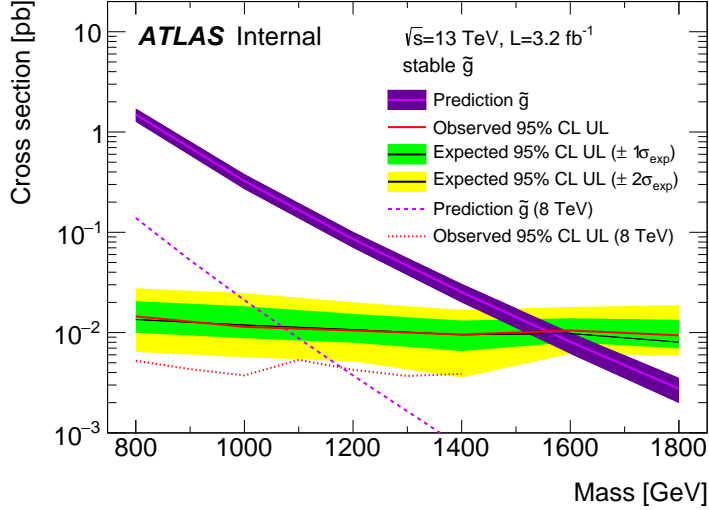


Figure 71: The observed and expected cross section limits as a function of mass for the stable simulated signal. The predicted cross section values for the corresponding signals are included.

ratio as a test statistic [78]. For this procedure, the systematic uncertainties estimated for the signal and background yields are treated as Gaussian-distributed nuisance parameters. The uncertainty on the normalization of the expected background distribution is included in the expected background events. At this point the expected cross section limit is calculated for both the metastable and stable signal region for each lifetime point, and the region with the best expected limit is selected for each lifetime. Using that procedure, the metastable region is used for lifetimes up to and including 30 ns, and the stable region for lifetimes above it.

The resulting cross-sectional upper limits are shown as a function of mass in Figure 71 and Figure 72 for each lifetime considered. The limits are interpolated linearly between each mass point, and the dependence of the limit on the mass is small as the efficiency is relatively constant for large R-Hadron masses. There is however a strong dependence on lifetime, as discussed in Section 11.5, where the probability to form a fully reconstructed track and the kinematic freedom to produce E_T^{miss} result in a local maximum in the limit at 10–30 ns. The figures also include the expected cross section for pair-produced gluino R-Hadrons for reference. For the 10 ns and stable cross section limits, both the observed limit and expected cross section for the Run 1, 8 TeV version of this analysis are included. There the cross sectional limits are lower because of the increased available luminosity, while the signal cross sections were also much lower because of the lower collision energy.

13.4 MASS LIMITS

The cross-sectional limits can then be used to derive a lower mass limit for gluino R-Hadrons by comparing them to the theoretically predicted production cross

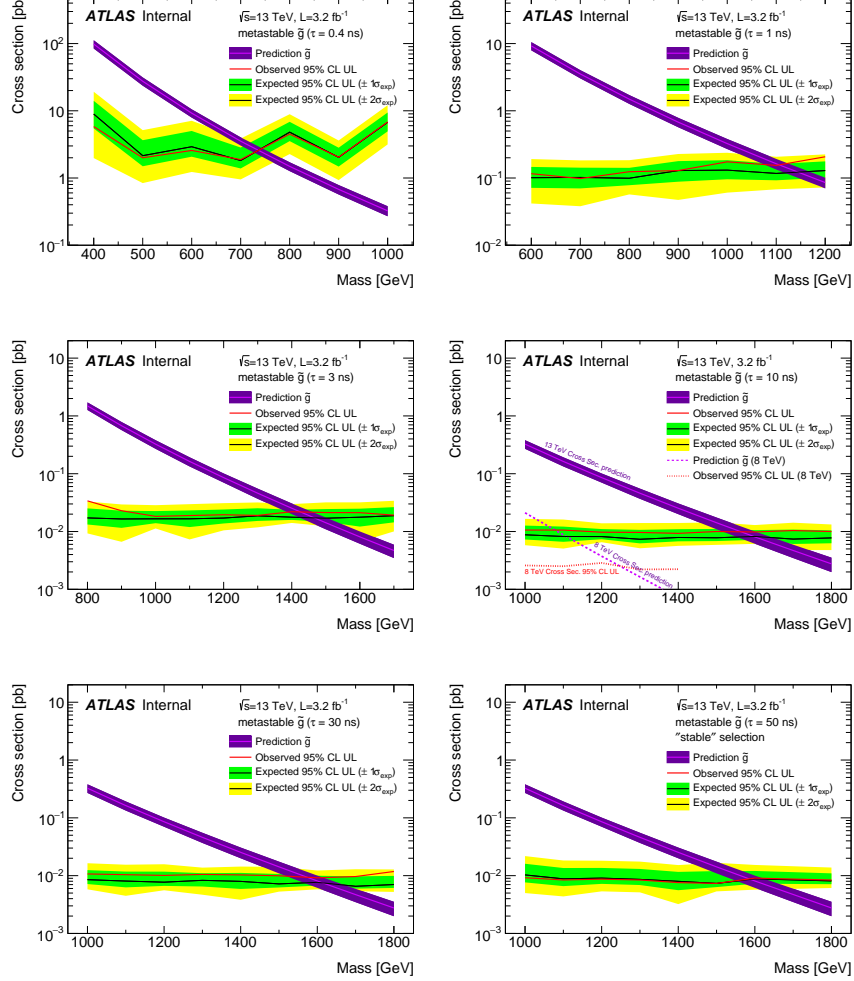


Figure 72: The observed and expected cross section limits as a function of mass for each generated lifetime. The predicted cross section values for the corresponding signals are included.

sections. These mass limits range from only 740 GeV at the lowest lifetimes considered, where the selection efficiency is very low, to up to 1580 GeV at 30 ns where the selection efficiency is maximized. The observed and expected mass limits for each lifetime point are detailed in Table 12, which also lists which selection region was used for each lifetime. These excluded range of masses as a function of lifetime is also shown in Figure 73. The Run 1 limits are included for comparison; the limits have increased by about 200 GeV on average. The search has also improved since the previous incarnation from Run 1 in optimizing the region between 30 GeV and detector-stable lifetimes by introducing the second signal region. The definition of the stable region prevents the significant drop in mass limit that occurred above 30 GeV in the Run 1 analysis.

Selection	τ [ns]	$M_{\text{obs}} > [\text{GeV}]$	$M_{\text{exp}} > [\text{GeV}]$
Metastable	0.4	740	730
"	1.0	1110	1150
"	3.0	1430	1470
"	10	1570	1600
"	30	1580	1620
Stable	50	1590	1590
"	stable	1570	1580

Table 12: The observed and expected 95% CL lower limit on mass for gluino R-Hadrons for each considered lifetime.

13.5 CONTEXT FOR LONG-LIVED SEARCHES

This search plays an important role in the current, combined [ATLAS](#) search for long lived particles. The mass limits provided by various [ATLAS](#) searches for long-lived gluino R-Hadrons can be seen in Figure 74. This search provides the most competitive limit for lifetimes between 3 ns up through very long lifetimes, where it is still competitive with dedicated searches for stable particles. The limits placed on gluino production are very similar to the limits on promptly decaying models.

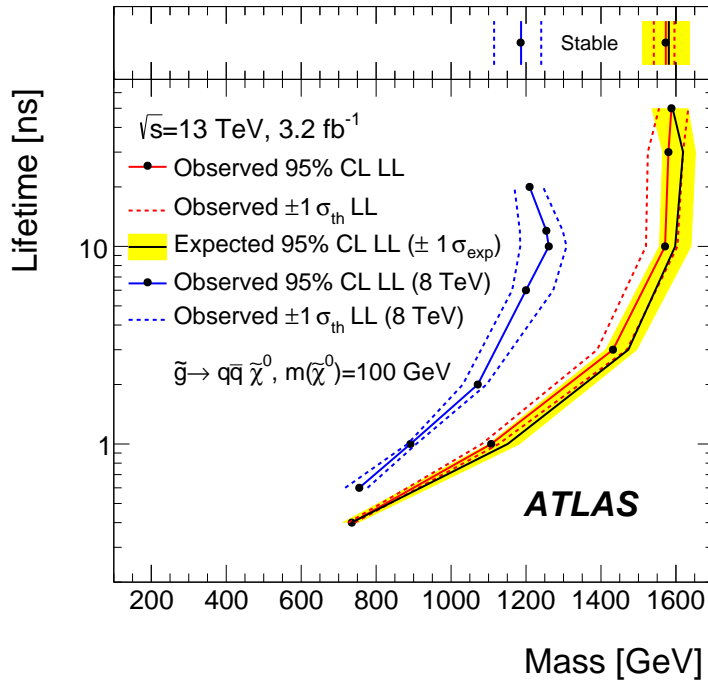


Figure 73: The excluded range of masses as a function of gluino lifetime. The expected lower limit (LL), with its experimental $\pm 1\sigma$ band, is given with respect to the nominal theoretical cross-section. The observed 95% LL obtained at $\sqrt{s} = 8 \text{ TeV}$ [61] is also shown for comparison.

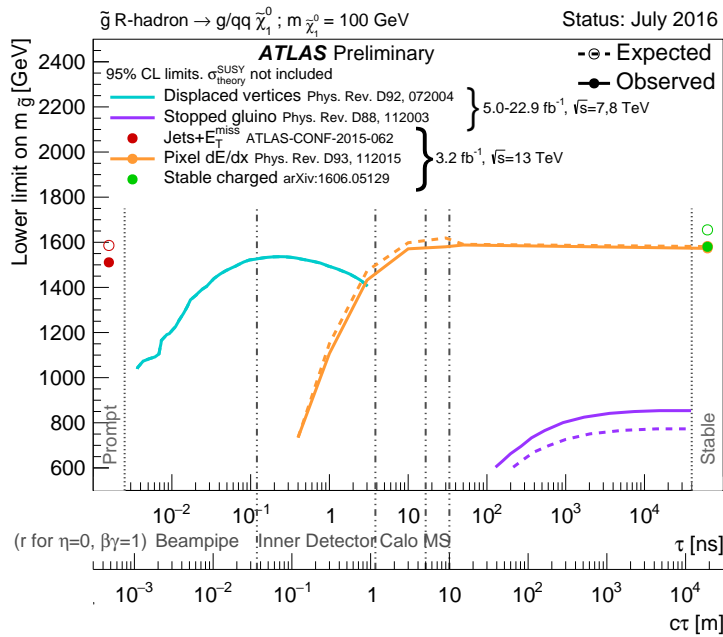


Figure 74: The constraints on the gluino mass as a function of lifetime for a split-supersymmetry model with the gluino R-Hadrons decaying into a gluon or light quarks and a neutralino with mass of 100 GeV. The solid lines indicate the observed limits, while the dashed lines indicate the expected limits. The area below the curves is excluded. The dots represent results for which the particle is assumed to be prompt or stable.

2237

PART VI

2238

CONCLUSIONS

2239

You can put some informational part preamble text here.

14

2240

2241 SUMMARY AND OUTLOOK

2242 14.1 SUMMARY

2243 14.2 OUTLOOK

2244

PART VII

2245

APPENDIX

2246

A

2247

2248 INELASTIC CROSS SECTION

B

2249

2250 EXPANDED R-HADRON YIELDS AND LIMITS

$m(\tilde{g})$ [GeV]	Left Extremum [GeV]	Right Extremum [GeV]
1000	682	1387
1100	763	1478
1200	801	1606
1300	809	1841
1400	861	2011
1500	920	2032
1600	952	2173
1800	1017	2422

Table 13: The left and right extremum of the mass window for each generated mass point with a 50 ns lifetime.

$m(\tilde{g})$ [GeV]	Left Extremum [GeV]	Right Extremum [GeV]
1000	689	1321
1100	746	1513
1200	788	1670
1300	860	1734
1400	833	1925
1500	852	2048
1600	833	2283
1700	946	2379
1800	869	2505

Table 14: The left and right extremum of the mass window for each generated mass point with a 30 ns lifetime.

$m(\tilde{g})$ [GeV]	Left Extremum [GeV]	Right Extremum [GeV]
1000	655	1349
1100	734	1455
1200	712	1631
1300	792	1737
1400	717	1926
1500	815	2117
1600	824	2122
1700	900	2274
1800	919	2344

Table 15: The left and right extremum of the mass window for each generated mass point with a 10 ns lifetime.

$m(\tilde{g})$ [GeV]	Left Extremum [GeV]	Right Extremum [GeV]
800	531	1065
900	576	1165
1000	610	1345
1100	635	1432
1200	663	1563
1300	620	1667
1400	742	1727
1500	761	1937
1600	573	2000
1700	621	2182

Table 16: The left and right extremum of the mass window used for each generated mass point with a lifetime of 3 ns.

$m(\tilde{g})$ [GeV]	Left Extremum [GeV]	Right Extremum [GeV]
600	411	758
700	385	876
800	486	970
900	406	987
1000	408	1136
1100	555	1196
1200	516	1378

Table 17: The left and right extremum of the mass window used for each mass point with a lifetime of 1 ns.

$m(\tilde{g})$ [GeV]	Left Extremum [GeV]	Right Extremum [GeV]
400	204	510
500	295	639
600	288	702
700	323	701
800	190	771
900	277	677
1000	249	688

Table 18: The left and right extremum of the mass window for each generated mass point with a lifetime of 0.4 ns.

$m(\tilde{g})$ [GeV]	Left Extremum [GeV]	Right Extremum [GeV]
800	627	1053
1000	726	1277
1200	857	1584
1400	924	1937
1600	993	2308
1800	1004	2554

Table 19: The left and right extremum of the mass window used for each generated stable mass point.

$m(\tilde{g})$ [GeV]	Expected Signal	Expected Background	Observed Data
1000	131.18 ± 6.35	1.803 ± 0.081	1.0 ± 1.0
1100	71.11 ± 3.35	1.409 ± 0.069	1.0 ± 1.0
1200	37.18 ± 1.75	1.310 ± 0.066	1.0 ± 1.0
1300	20.76 ± 0.95	1.431 ± 0.069	1.0 ± 1.0
1400	12.63 ± 0.57	1.273 ± 0.065	1.0 ± 1.0
1500	6.57 ± 0.29	1.115 ± 0.059	1.0 ± 1.0
1600	3.56 ± 0.16	1.041 ± 0.057	1.0 ± 1.0
1800	1.27 ± 0.05	0.918 ± 0.053	1.0 ± 1.0

Table 20: The expected number of signal events, the expected number of background events, and the observed number of events in data with their respective statistical errors within the respective mass window for each generated mass point with a lifetime of 50 ns.

$m(\tilde{g})$ [GeV]	Expected Signal	Expected Background	Observed Data
1000	144.65 ± 6.34	1.328 ± 0.063	2.0 ± 1.4
1100	75.28 ± 3.27	1.255 ± 0.060	2.0 ± 1.4
1200	40.51 ± 1.75	1.193 ± 0.058	2.0 ± 1.4
1300	20.91 ± 0.93	0.997 ± 0.051	2.0 ± 1.4
1400	11.97 ± 0.51	1.131 ± 0.056	2.0 ± 1.4
1500	6.81 ± 0.28	1.111 ± 0.055	2.0 ± 1.4
1600	4.19 ± 0.16	1.193 ± 0.058	2.0 ± 1.4
1700	2.42 ± 0.09	0.963 ± 0.050	2.0 ± 1.4
1800	1.46 ± 0.05	1.138 ± 0.056	3.0 ± 1.7

Table 21: The expected number of signal events, the expected number of background events, and the observed number of events in data with their respective statistical errors within the respective mass window for each generated mass point with a lifetime of 30 ns.

$m(\tilde{g})$ [GeV]	Expected Signal	Expected Background	Observed Data
1000	144.48 ± 5.14	1.499 ± 0.069	2.0 ± 1.4
1100	73.19 ± 2.61	1.260 ± 0.060	2.0 ± 1.4
1200	41.54 ± 1.41	1.456 ± 0.067	2.0 ± 1.4
1300	22.58 ± 0.77	1.201 ± 0.058	2.0 ± 1.4
1400	12.70 ± 0.42	1.558 ± 0.071	2.0 ± 1.4
1500	6.73 ± 0.24	1.237 ± 0.060	2.0 ± 1.4
1600	3.90 ± 0.13	1.201 ± 0.058	2.0 ± 1.4
1700	2.27 ± 0.07	1.027 ± 0.052	2.0 ± 1.4
1800	1.34 ± 0.04	1.019 ± 0.052	2.0 ± 1.4

Table 22: The expected number of signal events, the expected number of background events, and the observed number of events in data with their respective statistical errors within the respective mass window for each generated mass point with a lifetime of 10 ns.

$m(\tilde{g})$ [GeV]	Expected Signal	Expected Background	Observed Data
800	362.97 ± 14.68	1.841 ± 0.080	5.0 ± 2.2
900	169.20 ± 6.69	1.710 ± 0.076	3.0 ± 1.7
1000	84.78 ± 3.23	1.727 ± 0.076	2.0 ± 1.4
1100	40.06 ± 1.60	1.679 ± 0.075	2.0 ± 1.4
1200	20.06 ± 0.81	1.598 ± 0.072	2.0 ± 1.4
1300	10.76 ± 0.43	1.851 ± 0.080	2.0 ± 1.4
1400	5.52 ± 0.22	1.374 ± 0.064	2.0 ± 1.4
1500	3.16 ± 0.13	1.355 ± 0.064	2.0 ± 1.4
1600	2.13 ± 0.11	2.235 ± 0.093	3.0 ± 1.7
1700	1.10 ± 0.06	1.995 ± 0.085	2.0 ± 1.4

Table 23: The expected number of signal events, the expected number of background events, and the observed number of events in data with their respective statistical errors within the respective mass window for each generated mass point with a lifetime of 3 ns.

$m(\tilde{g})$ [GeV]	Expected Signal	Expected Background	Observed Data
600	431.80 ± 36.60	2.418 ± 0.099	3.0 ± 1.7
700	192.77 ± 15.28	3.267 ± 0.126	3.0 ± 1.7
800	69.63 ± 5.90	2.125 ± 0.089	3.0 ± 1.7
900	28.91 ± 2.59	3.114 ± 0.121	3.0 ± 1.7
1000	13.64 ± 1.22	3.359 ± 0.129	5.0 ± 2.2
1100	6.13 ± 0.57	1.879 ± 0.081	3.0 ± 1.7
1200	3.24 ± 0.30	2.387 ± 0.098	5.0 ± 2.2

Table 24: The expected number of signal events, the expected number of background events, and the observed number of events in data with their respective statistical errors within the respective mass window for each generated mass point with a lifetime of 1 ns.

$m(\tilde{g})$ [GeV]	Expected Signal	Expected Background	Observed Data
400	181.71 ± 75.59	6.780 ± 0.238	4.0 ± 2.0
500	103.88 ± 30.05	4.310 ± 0.160	4.0 ± 2.0
600	28.34 ± 9.34	4.868 ± 0.177	4.0 ± 2.0
700	13.62 ± 4.00	3.908 ± 0.147	4.0 ± 2.0
800	2.75 ± 1.15	9.001 ± 0.308	8.0 ± 2.8
900	2.25 ± 0.71	5.045 ± 0.183	5.0 ± 2.2
1000	0.34 ± 0.19	6.026 ± 0.214	6.0 ± 2.4

Table 25: The expected number of signal events, the expected number of background events, and the observed number of events in data with their respective statistical errors within the respective mass window for each generated mass point with a lifetime of p4 ns.

$m(\tilde{g})$ [GeV]	Expected Signal	Expected Background	Observed Data
800	462.83 ± 14.86	1.764 ± 0.080	2.0 ± 1.4
1000	108.73 ± 3.38	1.458 ± 0.070	1.0 ± 1.0
1200	31.74 ± 0.95	1.137 ± 0.060	1.0 ± 1.0
1400	10.22 ± 0.29	1.058 ± 0.058	1.0 ± 1.0
1600	3.07 ± 0.09	0.947 ± 0.054	1.0 ± 1.0
1800	1.08 ± 0.05	0.940 ± 0.054	1.0 ± 1.0

Table 26: The expected number of signal events, the expected number of background events, and the observed number of events in data with their respective statistical errors within the respective mass window for each generated stable mass point

2251 BIBLIOGRAPHY

- 2252 [1] Lyndon Evans and Philip Bryant. "LHC Machine". In: *JINST* 3 (2008), S08001.
2253 doi: [10.1088/1748-0221/3/08/S08001](https://doi.org/10.1088/1748-0221/3/08/S08001).
- 2254 [2] C Lefevre. "LHC: the guide (English version). Guide du LHC (version anglaise)".
2255 2009. URL: <https://cds.cern.ch/record/1165534>.
- 2256 [3] ATLAS Collaboration. "The ATLAS Experiment at the CERN Large Hadron
2257 Collider". In: *JINST* 3 (2008), S08003. doi: [10.1088/1748-0221/3/08/S08003](https://doi.org/10.1088/1748-0221/3/08/S08003).
- 2259 [4] S. Chatrchyan et al. "The CMS experiment at the CERN LHC". In: *JINST*
2260 3 (2008), S08004. doi: [10.1088/1748-0221/3/08/S08004](https://doi.org/10.1088/1748-0221/3/08/S08004).
- 2261 [5] A. Augusto Alves Jr. et al. "The LHCb Detector at the LHC". In: *JINST* 3
2262 (2008), S08005. doi: [10.1088/1748-0221/3/08/S08005](https://doi.org/10.1088/1748-0221/3/08/S08005).
- 2263 [6] K. Aamodt et al. "The ALICE experiment at the CERN LHC". In: *JINST* 3
2264 (2008), S08002. doi: [10.1088/1748-0221/3/08/S08002](https://doi.org/10.1088/1748-0221/3/08/S08002).
- 2265 [7] S. Agostinelli et al. "GEANT4: A simulation toolkit". In: *Nucl. Instrum. Meth.*
2266 A 506 (2003), pp. 250–303. doi: [10.1016/S0168-9002\(03\)01368-8](https://doi.org/10.1016/S0168-9002(03)01368-8).
- 2267 [8] ATLAS Collaboration. "A study of the material in the ATLAS inner de-
2268 tector using secondary hadronic interactions". In: *JINST* 7 (2012), P01013.
2269 doi: [10.1088/1748-0221/7/01/P01013](https://doi.org/10.1088/1748-0221/7/01/P01013). arXiv: [1110.6191 \[hep-ex\]](https://arxiv.org/abs/1110.6191).
2270 PERF-2011-08.
- 2271 [9] ATLAS Collaboration. "Electron and photon energy calibration with the
2272 ATLAS detector using LHC Run 1 data". In: *Eur. Phys. J. C* 74 (2014), p. 3071.
2273 doi: [10.1140/epjc/s10052-014-3071-4](https://doi.org/10.1140/epjc/s10052-014-3071-4). arXiv: [1407.5063](https://arxiv.org/abs/1407.5063)
2274 [hep-ex]. PERF-2013-05.
- 2275 [10] ATLAS Collaboration. "A measurement of the calorimeter response to sin-
2276 ggle hadrons and determination of the jet energy scale uncertainty using
2277 LHC Run-1 pp -collision data with the ATLAS detector". In: (2016). arXiv:
2278 [1607.08842 \[hep-ex\]](https://arxiv.org/abs/1607.08842). PERF-2015-05.
- 2279 [11] ATLAS Collaboration. "Single hadron response measurement and calorime-
2280 ter jet energy scale uncertainty with the ATLAS detector at the LHC". In:
2281 *Eur. Phys. J. C* 73 (2013), p. 2305. doi: [10.1140/epjc/s10052-013-2305-1](https://doi.org/10.1140/epjc/s10052-013-2305-1). arXiv: [1203.1302 \[hep-ex\]](https://arxiv.org/abs/1203.1302). PERF-2011-05.
- 2283 [12] ATLAS Collaboration. "The ATLAS Simulation Infrastructure". In: *Eur.*
2284 *Phys. J. C* 70 (2010), p. 823. doi: [10.1140/epjc/s10052-010-1429-9](https://doi.org/10.1140/epjc/s10052-010-1429-9).
2285 arXiv: [1005.4568 \[hep-ex\]](https://arxiv.org/abs/1005.4568). SOFT-2010-01.
- 2286 [13] T. Sjöstrand, S. Mrenna, and P. Skands. "A Brief Introduction to PYTHIA
2287 8.1". In: *Comput. Phys. Commun.* 178 (2008), pp. 852–867. doi: [10.1016/j.cpc.2008.01.036](https://doi.org/10.1016/j.cpc.2008.01.036). arXiv: [0710.3820](https://arxiv.org/abs/0710.3820).

- 2289 [14] ATLAS Collaboration. *Summary of ATLAS Pythia 8 tunes*. ATL-PHYS-PUB-
 2290 2012-003. 2012. URL: <http://cds.cern.ch/record/1474107>.
- 2291 [15] A.D. Martin, W.J. Stirling, R.S. Thorne, and G. Watt. “Parton distributions
 2292 for the LHC”. In: *Eur. Phys. J. C* 63 (2009). Figures from the MSTW Website,
 2293 pp. 189–285. doi: [10.1140/epjc/s10052-009-1072-5](https://doi.org/10.1140/epjc/s10052-009-1072-5). arXiv: [0901.0002](https://arxiv.org/abs/0901.0002).
- 2294 [16] A. Sherstnev and R.S. Thorne. “Parton Distributions for LO Generators”.
 2295 In: *Eur. Phys. J. C* 55 (2008), pp. 553–575. doi: [10.1140/epjc/s10052-008-0610-x](https://doi.org/10.1140/epjc/s10052-008-0610-x). arXiv: [0711.2473](https://arxiv.org/abs/0711.2473).
- 2296 [17] A. Ribon et al. *Status of Geant4 hadronic physics for the simulation of LHC*
 2297 *experiments at the start of LHC physics program*. CERN-LCGAPP-2010-02.
 2300 2010. URL: <http://lcgapp.cern.ch/project/docs/noteStatusHadronic2010.pdf>.
- 2301 [18] M. P. Guthrie, R. G. Alsmiller, and H. W. Bertini. “Calculation of the cap-
 2302 ture of negative pions in light elements and comparison with experiments
 2303 pertaining to cancer radiotherapy”. In: *Nucl. Instrum. Meth.* 66 (1968), pp. 29–
 2304 36. doi: [10.1016/0029-554X\(68\)90054-2](https://doi.org/10.1016/0029-554X(68)90054-2).
- 2305 [19] H. W. Bertini and P. Guthrie. “News item results from medium-energy
 2306 intranuclear-cascade calculation”. In: *Nucl. Instr. and Meth. A* 169 (1971),
 2307 p. 670. doi: [10.1016/0375-9474\(71\)90710-X](https://doi.org/10.1016/0375-9474(71)90710-X).
- 2308 [20] V.A. Karmanov. “Light Front Wave Function of Relativistic Composite
 2309 System in Explicitly Solvable Model”. In: *Nucl. Phys. B* 166 (1980), p. 378.
 2310 doi: [10.1016/0550-3213\(80\)90204-7](https://doi.org/10.1016/0550-3213(80)90204-7).
- 2311 [21] H. S. Fesefeldt. *GHEISHA program*. Pitha-85-02, Aachen. 1985.
- 2312 [22] G. Folger and J.P. Wellisch. “String parton models in Geant4”. In: (2003).
 2313 arXiv: [nucl-th/0306007](https://arxiv.org/abs/nucl-th/0306007).
- 2314 [23] N. S. Amelin et al. “Transverse flow and collectivity in ultrarelativistic
 2315 heavy-ion collisions”. In: *Phys. Rev. Lett.* 67 (1991), p. 1523. doi: [10.1103/PhysRevLett.67.1523](https://doi.org/10.1103/PhysRevLett.67.1523).
- 2316 [24] N. S. Amelin et al. “Collectivity in ultrarelativistic heavy ion collisions”. In:
 2317 *Nucl. Phys. A* 544 (1992), p. 463. doi: [10.1016/0375-9474\(92\)90598-E](https://doi.org/10.1016/0375-9474(92)90598-E).
- 2318 [25] L. V. Bravina et al. “Fluid dynamics and Quark Gluon string model - What
 2319 we can expect for Au+Au collisions at 11.6 AGeV/c”. In: *Nucl. Phys. A* 566
 2320 (1994), p. 461. doi: [10.1016/0375-9474\(94\)90669-6](https://doi.org/10.1016/0375-9474(94)90669-6).
- 2321 [26] L. V. Bravin et al. “Scaling violation of transverse flow in heavy ion colli-
 2322 sions at AGS energies”. In: *Phys. Lett. B* 344 (1995), p. 49. doi: [10.1016/0370-2693\(94\)01560-Y](https://doi.org/10.1016/0370-2693(94)01560-Y).
- 2323 [27] B. Andersson et al. “A model for low-pT hadronic reactions with general-
 2324 izations to hadron-nucleus and nucleus-nucleus collisions”. In: *Nucl. Phys.*
 2325 *B* 281 (1987), p. 289. doi: [10.1016/0550-3213\(87\)90257-4](https://doi.org/10.1016/0550-3213(87)90257-4).

- [28] B. Andersson, A. Tai, and B.-H. Sa. “Final state interactions in the (nuclear) FRITIOF string interaction scenario”. In: *Z. Phys. C* 70 (1996), pp. 499–506. doi: [10.1007/s002880050127](https://doi.org/10.1007/s002880050127).
- [29] B. Nilsson-Almqvist and E. Stenlund. “Interactions Between Hadrons and Nuclei: The Lund Monte Carlo, Fritiof Version 1.6”. In: *Comput. Phys. Commun.* 43 (1987), p. 387. doi: [10.1016/0010-4655\(87\)90056-7](https://doi.org/10.1016/0010-4655(87)90056-7).
- [30] B. Ganhuyag and V. Uzhinsky. “Modified FRITIOF code: Negative charged particle production in high energy nucleus nucleus interactions”. In: *Czech. J. Phys.* 47 (1997), pp. 913–918. doi: [10.1023/A:1021296114786](https://doi.org/10.1023/A:1021296114786).
- [31] ATLAS Collaboration. “Topological cell clustering in the ATLAS calorimeters and its performance in LHC Run 1”. In: (2016). arXiv: [1603.02934 \[hep-ex\]](https://arxiv.org/abs/1603.02934).
- [32] Peter Speckmayer. “Energy Measurement of Hadrons with the CERN ATLAS Calorimeter”. Presented on 18 Jun 2008. PhD thesis. Vienna: Vienna, Tech. U., 2008. url: <http://cds.cern.ch/record/1112036>.
- [33] CMS Collaboration. “The CMS barrel calorimeter response to particle beams from 2 to 350 GeV/c”. In: *Eur. Phys. J. C* 60.3 (2009). doi: [10.1140/epjc/s10052-009-0959-5](https://doi.org/10.1140/epjc/s10052-009-0959-5).
- [34] J. Beringer et al. (Particle Data Group). “Review of Particle Physics”. In: *Chin. Phys. C* 38 (2014), p. 090001. url: <http://pdg.lbl.gov>.
- [35] P. Adragna et al. “Measurement of Pion and Proton Response and Longitudinal Shower Profiles up to 20 Nuclear Interaction Lengths with the ATLAS Tile Calorimeter”. In: *Nucl. Instrum. Meth. A* 615 (2010), pp. 158–181. doi: [10.1016/j.nima.2010.01.037](https://doi.org/10.1016/j.nima.2010.01.037).
- [36] ATLAS Collaboration. “Jet energy measurement and its systematic uncertainty in proton–proton collisions at $\sqrt{s} = 7$ TeV with the ATLAS detector”. In: *Eur. Phys. J. C* 75 (2015), p. 17. doi: [10.1140/epjc/s10052-014-3190-y](https://doi.org/10.1140/epjc/s10052-014-3190-y). arXiv: [1406.0076 \[hep-ex\]](https://arxiv.org/abs/1406.0076). PERF-2012-01.
- [37] Hung-Liang Lai, Marco Guzzi, Joey Huston, Zhao Li, Pavel M. Nadolsky, et al. “New parton distributions for collider physics”. In: *Phys. Rev. D* 82 (2010), p. 074024. doi: [10.1103/PhysRevD.82.074024](https://doi.org/10.1103/PhysRevD.82.074024). arXiv: [1007.2241 \[hep-ph\]](https://arxiv.org/abs/1007.2241).
- [38] E. Abat et al. “Study of energy response and resolution of the ATLAS barrel calorimeter to hadrons of energies from 20 to 350 GeV”. In: *Nucl. Instrum. Meth. A* 621.1-3 (2010), pp. 134 –150. doi: <http://dx.doi.org/10.1016/j.nima.2010.04.054>.
- [39] ATLAS Collaboration. “Jet energy measurement with the ATLAS detector in proton–proton collisions at $\sqrt{s} = 7$ TeV”. In: *Eur. Phys. J. C* 73 (2013), p. 2304. doi: [10.1140/epjc/s10052-013-2304-2](https://doi.org/10.1140/epjc/s10052-013-2304-2). arXiv: [1112.6426 \[hep-ex\]](https://arxiv.org/abs/1112.6426). PERF-2011-03.
- [40] Nausheen R. Shah and Carlos E. M. Wagner. “Gravitons and dark matter in universal extra dimensions”. In: *Phys. Rev. D* 74 (2006), p. 104008. doi: [10.1103/PhysRevD.74.104008](https://doi.org/10.1103/PhysRevD.74.104008). arXiv: [hep-ph/0608140 \[hep-ph\]](https://arxiv.org/abs/hep-ph/0608140).

- [41] Jonathan L. Feng, Arvind Rajaraman, and Fumihiro Takayama. “Graviton cosmology in universal extra dimensions”. In: *Phys. Rev.* D68 (2003), p. 085018. doi: [10.1103/PhysRevD.68.085018](https://doi.org/10.1103/PhysRevD.68.085018). arXiv: [hep-ph/0307375](https://arxiv.org/abs/hep-ph/0307375) [hep-ph].
- [42] Paul H. Frampton and Pham Quang Hung. “Long-lived quarks?” In: *Phys. Rev. D* 58 (5 1998), p. 057704. doi: [10.1103/PhysRevD.58.057704](https://doi.org/10.1103/PhysRevD.58.057704). URL: <http://link.aps.org/doi/10.1103/PhysRevD.58.057704>.
- [43] C. Friberg, E. Norrbin, and T. Sjostrand. “QCD aspects of leptoquark production at HERA”. In: *Phys. Lett.* B403 (1997), pp. 329–334. doi: [10.1016/S0370-2693\(97\)00543-1](https://doi.org/10.1016/S0370-2693(97)00543-1). arXiv: [hep-ph/9704214](https://arxiv.org/abs/hep-ph/9704214) [hep-ph].
- [44] Herbert K. Dreiner. “An introduction to explicit R-parity violation”. In: (1997). arXiv: [hep-ph/9707435](https://arxiv.org/abs/hep-ph/9707435).
- [45] Edmond L. Berger and Zack Sullivan. “Lower limits on R-parity-violating couplings in supersymmetry”. In: *Phys. Rev. Lett.* 92 (2004), p. 201801. doi: [10.1103/PhysRevLett.92.201801](https://doi.org/10.1103/PhysRevLett.92.201801). arXiv: [hep-ph/0310001](https://arxiv.org/abs/hep-ph/0310001).
- [46] R. Barbieri, C. Berat, M. Besancon, M. Chemtob, A. Deandrea, et al. “R-parity violating supersymmetry”. In: *Phys. Rept.* 420 (2005), p. 1. doi: [10.1016/j.physrep.2005.08.006](https://doi.org/10.1016/j.physrep.2005.08.006). arXiv: [hep-ph/0406039](https://arxiv.org/abs/hep-ph/0406039).
- [47] M. Fairbairn et al. “Stable massive particles at colliders”. In: *Phys. Rept.* 438 (2007), p. 1. doi: [10.1016/j.physrep.2006.10.002](https://doi.org/10.1016/j.physrep.2006.10.002). arXiv: [hep-ph/0611040](https://arxiv.org/abs/hep-ph/0611040).
- [48] Christopher F. Kolda. “Gauge-mediated supersymmetry breaking: Introduction, review and update”. In: *Nucl. Phys. Proc. Suppl.* 62 (1998), p. 266. doi: [10.1016/S0920-5632\(97\)00667-1](https://doi.org/10.1016/S0920-5632(97)00667-1). arXiv: [hep-ph/9707450](https://arxiv.org/abs/hep-ph/9707450).
- [49] Howard Baer, Kingman Cheung, and John F. Gunion. “A Heavy gluino as the lightest supersymmetric particle”. In: *Phys. Rev. D* 59 (1999), p. 075002. doi: [10.1103/PhysRevD.59.075002](https://doi.org/10.1103/PhysRevD.59.075002). arXiv: [hep-ph/9806361](https://arxiv.org/abs/hep-ph/9806361).
- [50] S. James Gates Jr. and Oleg Lebedev. “Searching for supersymmetry in hadrons”. In: *Phys. Lett. B* 477 (2000), p. 216. doi: [10.1016/S0370-2693\(00\)00172-6](https://doi.org/10.1016/S0370-2693(00)00172-6). arXiv: [hep-ph/9912362](https://arxiv.org/abs/hep-ph/9912362).
- [51] G. F. Giudice and A. Romanino. “Split supersymmetry”. In: *Nucl. Phys. B* 699 (2004), p. 65. doi: [10.1016/j.nuclphysb.2004.11.048](https://doi.org/10.1016/j.nuclphysb.2004.11.048). arXiv: [hep-ph/0406088](https://arxiv.org/abs/hep-ph/0406088).
- [52] N. Arkani-Hamed, S. Dimopoulos, G. F. Giudice, and A. Romanino. “Aspects of split supersymmetry”. In: *Nucl. Phys. B* 709 (2005), p. 3. doi: [10.1016/j.nuclphysb.2004.12.026](https://doi.org/10.1016/j.nuclphysb.2004.12.026). arXiv: [hep-ph/0409232](https://arxiv.org/abs/hep-ph/0409232).
- [53] Glennys R. Farrar and Pierre Fayet. “Phenomenology of the Production, Decay, and Detection of New Hadronic States Associated with Supersymmetry”. In: *Phys. Lett.* B76 (1978), pp. 575–579. doi: [10.1016/0370-2693\(78\)90858-4](https://doi.org/10.1016/0370-2693(78)90858-4).

- 2414 [54] A. C. Kraan, J. B. Hansen, and P. Nevski. “Discovery potential of R-hadrons
 2415 with the ATLAS detector”. In: *Eur. Phys. J.* C49 (2007), pp. 623–640. doi:
 2416 [10.1140/epjc/s10052-006-0162-x](https://doi.org/10.1140/epjc/s10052-006-0162-x). arXiv: [hep-ex/0511014](https://arxiv.org/abs/hep-ex/0511014)
 2417 [[hep-ex](#)].
- 2418 [55] K. A. Olive et al. “Review of Particle Physics”. In: *Chin. Phys.* C38 (2014),
 2419 p. 090001. doi: [10.1088/1674-1137/38/9/090001](https://doi.org/10.1088/1674-1137/38/9/090001).
- 2420 [56] Rasmus Mackeprang and David Milstead. “An Updated Description of
 2421 Heavy-Hadron Interactions in GEANT-4”. In: *Eur. Phys. J.* C66 (2010), pp. 493–
 2422 501. doi: [10.1140/epjc/s10052-010-1262-1](https://doi.org/10.1140/epjc/s10052-010-1262-1). arXiv: [0908.1868](https://arxiv.org/abs/0908.1868)
 2423 [[hep-ph](#)].
- 2424 [57] ATLAS Collaboration. “Search for massive, long-lived particles using mul-
 2425 titrack displaced vertices or displaced lepton pairs in pp collisions at $\sqrt{s} =$
 2426 8 TeV with the ATLAS detector”. In: *Phys. Rev. D* 92 (2015), p. 072004.
 2427 doi: [10.1103/PhysRevD.92.072004](https://doi.org/10.1103/PhysRevD.92.072004). arXiv: [1504.05162](https://arxiv.org/abs/1504.05162) [[hep-ex](#)].
 2428 SUSY-2014-02.
- 2429 [58] ATLAS Collaboration. “Search for charginos nearly mass degenerate with
 2430 the lightest neutralino based on a disappearing-track signature in pp col-
 2431 lisions at $\sqrt{s} = 8$ TeV with the ATLAS detector”. In: *Phys. Rev. D* 88 (2013),
 2432 p. 112006. doi: [10.1103/PhysRevD.88.112006](https://doi.org/10.1103/PhysRevD.88.112006). arXiv: [1310.3675](https://arxiv.org/abs/1310.3675)
 2433 [[hep-ex](#)]. SUSY-2013-01.
- 2434 [59] ATLAS Collaboration. “Searches for heavy long-lived sleptons and R-Hadrons
 2435 with the ATLAS detector in pp collisions at $\sqrt{s} = 7$ TeV”. In: *Phys. Lett. B*
 2436 720 (2013), p. 277. doi: [10.1016/j.physletb.2013.02.015](https://doi.org/10.1016/j.physletb.2013.02.015). arXiv:
 2437 [1211.1597](https://arxiv.org/abs/1211.1597) [[hep-ex](#)]. SUSY-2012-01.
- 2438 [60] ATLAS Collaboration. “Searches for heavy long-lived charged particles
 2439 with the ATLAS detector in proton–proton collisions at $\sqrt{s} = 8$ TeV”. In:
 2440 *JHEP* 01 (2015), p. 068. doi: [10.1007/JHEP01\(2015\)068](https://doi.org/10.1007/JHEP01(2015)068). arXiv:
 2441 [1411.6795](https://arxiv.org/abs/1411.6795) [[hep-ex](#)]. SUSY-2013-22.
- 2442 [61] ATLAS Collaboration. “Search for metastable heavy charged particles with
 2443 large ionisation energy loss in pp collisions at $\sqrt{s} = 8$ TeV using the AT-
 2444 LAS experiment”. In: *Eur. Phys. J.* C 75 (2015), p. 407. doi: [10.1140/epjc/s10052-015-3609-0](https://doi.org/10.1140/epjc/s10052-015-3609-0). arXiv: [1506.05332](https://arxiv.org/abs/1506.05332) [[hep-ex](#)]. SUSY-
 2445 2014-09.
- 2447 [62] ATLAS Collaboration. “Search for heavy long-lived charged R -hadrons
 2448 with the ATLAS detector in 3.2 fb^{-1} of proton–proton collision data at
 2449 $\sqrt{s} = 13$ TeV”. In: *Phys. Lett.* B760 (2016), pp. 647–665. doi: [10.1016/j.physletb.2016.07.042](https://doi.org/10.1016/j.physletb.2016.07.042). arXiv: [1606.05129](https://arxiv.org/abs/1606.05129) [[hep-ex](#)].
 2450
- 2451 [63] Torbjorn Sjöstrand, Stephen Mrenna, and Peter Skands. “PYTHIA 6.4 Physics
 2452 and Manual”. In: *JHEP* 0605 (2006), p. 026. doi: [10.1088/1126-6708/2006/05/026](https://doi.org/10.1088/1126-6708/2006/05/026). arXiv: [hep-ph/0603175](https://arxiv.org/abs/hep-ph/0603175).
- 2454 [64] *Further ATLAS tunes of PYTHIA6 and Pythia 8*. Tech. rep. ATL-PHYS-PUB-
 2455 2011-014. Geneva: CERN, 2011. URL: <https://cds.cern.ch/record/1400677>.

- [65] Aafke Christine Kraan. “Interactions of heavy stable hadronizing particles”. In: *Eur. Phys. J.* C37 (2004), pp. 91–104. doi: [10.1140/epjc/s2004-01946-6](https://doi.org/10.1140/epjc/s2004-01946-6). arXiv: [hep-ex/0404001](https://arxiv.org/abs/hep-ex/0404001) [hep-ex].
- [66] M. Fairbairn et al. “Stable massive particles at colliders”. In: *Phys. Rept.* 438 (2007), p. 1. doi: [10.1016/j.physrep.2006.10.002](https://doi.org/10.1016/j.physrep.2006.10.002). arXiv: [hep-ph/0611040](https://arxiv.org/abs/hep-ph/0611040).
- [67] W. Beenakker, R. Hopker, M. Spira, and P. M. Zerwas. “Squark and gluino production at hadron colliders”. In: *Nucl. Phys. B* 492 (1997), p. 51. doi: [10.1016/S0550-3213\(97\)00084-9](https://doi.org/10.1016/S0550-3213(97)00084-9). arXiv: [hep-ph/9610490](https://arxiv.org/abs/hep-ph/9610490).
- [68] A. Kulesza and L. Motyka. “Threshold resummation for squark-antisquark and gluino-pair production at the LHC”. In: *Phys. Rev. Lett.* 102 (2009), p. 111802. doi: [10.1103/PhysRevLett.102.111802](https://doi.org/10.1103/PhysRevLett.102.111802). arXiv: [0807.2405](https://arxiv.org/abs/0807.2405) [hep-ph].
- [69] A. Kulesza and L. Motyka. “Soft gluon resummation for the production of gluino-gluino and squark-antisquark pairs at the LHC”. In: *Phys. Rev. D* 80 (2009), p. 095004. doi: [10.1103/PhysRevD.80.095004](https://doi.org/10.1103/PhysRevD.80.095004). arXiv: [0905.4749](https://arxiv.org/abs/0905.4749) [hep-ph].
- [70] Wim Beenakker, Silja Brensing, Michael Kramer, Anna Kulesza, Eric Laenen, et al. “Soft-gluon resummation for squark and gluino hadroproduction”. In: *JHEP* 0912 (2009), p. 041. doi: [10.1088/1126-6708/2009/12/041](https://doi.org/10.1088/1126-6708/2009/12/041). arXiv: [0909.4418](https://arxiv.org/abs/0909.4418) [hep-ph].
- [71] W. Beenakker, S. Brensing, M.n Kramer, A. Kulesza, E. Laenen, et al. “Squark and Gluino Hadroproduction”. In: *Int. J. Mod. Phys. A* 26 (2011), p. 2637. doi: [10.1142/S0217751X11053560](https://doi.org/10.1142/S0217751X11053560). arXiv: [1105.1110](https://arxiv.org/abs/1105.1110) [hep-ph].
- [72] Michael Krämer et al. *Supersymmetry production cross sections in pp collisions at $\sqrt{s} = 7 \text{ TeV}$* . 2012. arXiv: [1206.2892](https://arxiv.org/abs/1206.2892) [hep-ph].
- [73] Rasmus Mackeprang and Andrea Rizzi. “Interactions of Coloured Heavy Stable Particles in Matter”. In: *Eur. Phys. J.* C50 (2007), pp. 353–362. doi: [10.1140/epjc/s10052-007-0252-4](https://doi.org/10.1140/epjc/s10052-007-0252-4). arXiv: [hep-ph/0612161](https://arxiv.org/abs/hep-ph/0612161) [hep-ph].
- [74] Rasmus Mackeprang and David Milstead. “An Updated Description of Heavy-Hadron Interactions in GEANT-4”. In: *Eur. Phys. J.* C66 (2010), pp. 493–501. doi: [10.1140/epjc/s10052-010-1262-1](https://doi.org/10.1140/epjc/s10052-010-1262-1). arXiv: [0908.1868](https://arxiv.org/abs/0908.1868) [hep-ph].
- [75] J. Alwall, R. Frederix, S. Frixione, V. Hirschi, F. Maltoni, O. Mattelaer, H. S. Shao, T. Stelzer, P. Torrielli, and M. Zaro. “The automated computation of tree-level and next-to-leading order differential cross sections, and their matching to parton shower simulations”. In: *JHEP* 07 (2014), p. 079. doi: [10.1007/JHEP07\(2014\)079](https://doi.org/10.1007/JHEP07(2014)079). arXiv: [1405.0301](https://arxiv.org/abs/1405.0301) [hep-ph].
- [76] “dE/dx measurement in the ATLAS Pixel Detector and its use for particle identification”. In: (2011).

- 2498 [77] ATLAS Collaboration. “The ATLAS Simulation Infrastructure”. In: *Eur.*
2499 *Phys. J.* C70 (2010), pp. 823–874. doi: [10.1140/epjc/s10052-010-1429-9](https://doi.org/10.1140/epjc/s10052-010-1429-9). arXiv: [1005.4568 \[physics.ins-det\]](https://arxiv.org/abs/1005.4568).
- 2500
2501 [78] Alexander L. Read. “Presentation of search results: The CL(s) technique”.
2502 In: *J. Phys.* G28 (2002). [,11(2002)], pp. 2693–2704. doi: [10.1088/0954-3899/28/10/313](https://doi.org/10.1088/0954-3899/28/10/313).
2503

2504 DECLARATION

2505 Put your declaration here.

2506 *Berkeley, CA, September 2016*

2507

Bradley Axen

2508

2509 COLOPHON

2510

Not sure that this is necessary.